Optimising Green Ammonia Production via SOEC Heat Integration to Support Decarbonisation of The Maritime Sector

A Techno-Economic Study

Rie Emilie Hansen

Thermal Energy & Process Engineering, 2025-08

Master's Thesis

This report is composed in the program LaTeX. The AspenTech® software Aspen Plus was used for process modelling, while MATLAB® was used for modelling and plotting, and Microsoft® Excel for simple calculations and data processing. All illustrations in the report are made in Adobe® Illustrator.

Energy Technology
Aalborg Universitet
http://www.aau.dk

AALBORG UNIVERSITY
STUDENT REPORT

Title:
Optimising Green Ammonia Production via SOEC Heat Integration to Support Decarbonisation of The Maritime Sector

Theme:
Master's Thesis

Project Period:
Spring Semester 2025

Participant:
Rie Emilie Hansen

Supervisors:
Mads Pagh Nielsen
Vincenzo Liso
Hossein Asgharian

Copies: 1

Page Numbers: 75

Date of Completion:
August 29th 2025

Abstract:

Decarbonising the maritime sector is a pressing challenge in achieving global climate goals, as shipping faces significant complications to direct electrification. In response to this, the production of green ammonia, integrated with high-temperature (HT) solid oxide electrolysis cells (SOECs) and low-temperature (LT) proton-conducting SOECs (P-SOECs), is investigated to optimise large-scale green ammonia production for maritime applications. The objective is to evaluate the technical and economic feasibility of a 500 MW electrolysis-based ammonia plant with and without heat integration between the Haber-Bosch reactor (HBR) and steam electrolysis. The plant is modelled as three subsystems: hydrogen production via steam electrolysis, nitrogen production via cryogenic air separation, and ammonia synthesis through the HB process. Process simulations in Aspen Plus are coupled with electrochemical modelling in MATLAB to assess four case configurations: SOEC and P-SOEC systems, with and without heat integration. Results show that heat integration significantly improves plant performance, with the heat-integrated HT SOEC case achieving the highest electrical efficiency of 82.3% and lowest levelised cost of ammonia (LCOA) of 310 - 535 USD/ton$_{NH_3}$, making it competitive with other green ammonia pathways. While the P-SOEC configuration benefits most from waste-heat integration, it remains constrained by lower Faradaic efficiency and higher capital costs. These findings highlight the potential of heat-integrated steam electrolysis systems as a cost-effective pathway to supply green ammonia for the maritime industrys transition to carbon neutrality.

Summary

This thesis investigates the techno-economic feasibility of optimising green ammonia production by integrating high-temperature (HT) solid oxide electrolysis cells (SOECs) and low-temperature (LT) proton-conducting SOECs (P-SOECs) with the Haber-Bosch (HB) process. The work is motivated by the pressing need to decarbonise the maritime sector, a hard-to-abate industry that accounts for approximately 2.3% of global CO_2 emissions. Using ammonia as an e-fuel presents advantages in terms of a high volumetric energy density, an existing global infrastructure, and potential for fully renewable production without any CO_2 emissions. To accommodate the e-fuel production capacity required for the transition of the maritime industry, a large-scale green ammonia plant using a 500 MW electrolysis system is considered.

The large-scale green ammonia plant is modelled as three main subsystems: (1) hydrogen production via steam electrolysis, (2) nitrogen production via a cryogenic air separation unit (CASU), and (3) ammonia synthesis through the HB process. Emphasis is placed on the integration of waste heat from the HB reactor (HBR), enabled by the exothermic ammonia synthesis reaction, to improve overall plant efficiency and reduce production costs. When considering heat integration between ammonia synthesis and steam electrolysis, an optimisation problem arises, since ammonia synthesis favours lower operating temperatures (400-500 °C) to increase the equilibrium conversion and thereby ammonia yield. In comparison, steam electrolysis favours higher operating temperatures (800-1000 °C) for increased Faradaic efficiency (FE) and thereby hydrogen production. If a steam electrolyser is operated at a lower temperature, it increases the percentage of the required heat duty for steam generation that the HBR can cover, thereby reducing energy consumption. However, this also reduces hydrogen generation from the electrolyser, creating the optimisation problem. Therefore, four plant configurations are evaluated to analyse the effect of steam electrolysis operating temperature:

1. HT SOEC without heat integration (SOEC-B)
2. HT SOEC with heat integration (SOEC-INT)
3. LT P-SOEC without heat integration (P-SOEC-B)
4. LT P-SOEC with heat integration (P-SOEC-INT)

Process models of the three subsystems are developed in Aspen Plus, including specified ammonia synthesis reaction kinetics and coupling with electrochemical models in MATLAB. The results show significant benefits of heat integration. The SOEC-INT case achieves the highest plant energy efficiency by significantly reducing the external heating requirement, resulting in lower operational costs compared to the non-integrated cases. While the P-SOEC offers potential improvements in durability due to lower operating temperatures, its lower FE leads to higher electricity and water consumption, and elevated stack prices lead to higher capital costs and therefore levelised cost of ammonia (LCOA). The techno-economic analysis indicates that the SOEC-INT configuration is the most cost-effective, enabling ammonia pro-

duction at a competitive price compared to other green ammonia pathways. The resulting plant energy efficiency and LCOA across the four cases are seen in Figure 1.

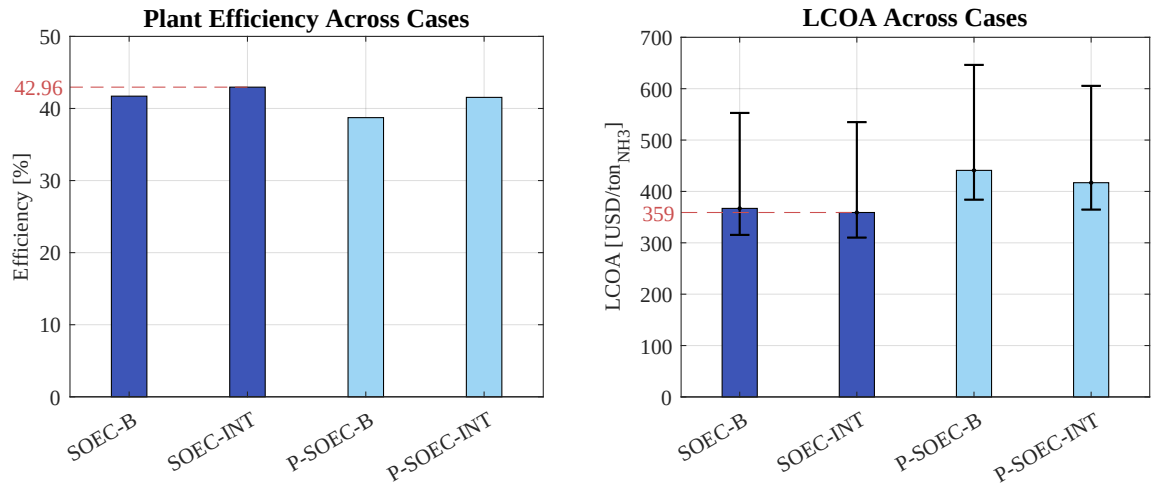

(a) Plant energy efficiency.

(b) LCOA after 20 years.

Figure 1: Comparison of the four cases in terms of overall plant energy efficiency and LCOA. An upper and lower margin for the LCOA is included to illustrate the sensitivity of electricity costs.

Besides the performance presented in Figure 1, the main conclusions can be summarised as follows:

- Heat integration between the HBR and SOEC significantly improves the technical performance of the ammonia plants by covering 55.2% and 69.7% of the heat required for steam generation in the SOEC and P-SOEC systems, respectively.
- The HT SOEC cases offer the best balance of efficiency and LCOA for large-scale e-ammonia production, although durability challenges remain. SOEC-INT is the most cost-effective configuration with an electrolysis electrical efficiency of 82.3%.
- The LT P-SOEC cases exhibit the highest relative efficiency gain from adding heat integration, increasing the electrolysis electrical efficiency from 67.7% to 75.5%. However, challenges in stack efficiency, prices and scalability must be addressed.
- Green ammonia can play an important role in the transition of the maritime sector to carbon neutrality, with integrated systems enabling competitive production costs.

Preface

This master's thesis is written on the 4th semester of the master's program in *Energy Engineering* with specialisation in *Thermal Energy and Process Engineering* at the Faculty of Engineering and Science at Aalborg University.

Reading Guide

The references to literature in the report are done using the Vancouver method. The references are shown as [number], representing the order in which they appear in the project. A reference may appear in a sentence if it refers to something specific, or after a paragraph if it is used for the entire content of that paragraph. A bibliography is included at the end of the report, where the references and the source information appear.

The main part of the project is divided into chapters and sections with assigned numbering, as seen in the table of contents. Appendices are labelled with a letter. Figures, tables, and equations are assigned numbers according to the order in which they appear in the given chapter.
The report includes a nomenclature containing an overview of the symbols and abbreviations used alphabetically. Numbers are divided in thousands by a comma and separate decimals by a period.

Acknowledgements

I want to express my gratitude to my supervisors, Professor *Mads Pagh Nielsen*, Associate Professor *Vincenzo Liso*, and Postdoctoral Researcher *Hossein Asgharian*, for their guidance, constructive feedback and continuous support throughout the course of this thesis. Their expertise has been fundamental to the completion of this work.

Rie Emilie Hansen
<reha19@student.aau.dk>

Nomenclature

Symbol	Description	SI Unit
a	Activity	[atm]
d	Discount rate	[%]
f°	Pure component fugacity	[atm]
k_r	Kinetic constant of reverse reaction	$[\mathrm{mol}/(\mathrm{m}^3 \cdot \mathrm{atm} \cdot \mathrm{s})]$
$\dot{m}$	Mass flow rate	[kg/s]
m	Mass	[kg]
$\dot{n}$	Molar flow rate	[mol/s]
p	Partial pressure	[bar]
r	Reaction rate	$[\mathrm{mol}/\mathrm{m}^3 - \mathrm{s}]$
x	Mole fraction	[-]
y	Year	[-]
A	Area	$[\mathrm{m}^2]$
C	Costs	[USD]
D	Diameter	[m]
E	Voltage	[V]
E^0	Open-cell potential	[V]
F	Faraday constant	[C/mol]
$GHSV$	Has-hourly space velocity	[1/h]
HHV	Higher heating value	[MJ/kg]
H_{rxn}	Heat of reaction	[kJ/mol]
I	Current density	$[\mathrm{A}/\mathrm{m}^2]$
I_0	Exchange current density	$[\mathrm{A}/\mathrm{m}^2]$
K_a	Equilibrium constant	[-]
L	Length	[m]
$LCOA$	Levelised cost of ammonia	[USD/ton]
LHV	Lower heating value	[MJ/kg]
N	Number of	[-]
P	Pressure	[bar]
$\dot{Q}$	Heat transfer rate	[W]
R_u	Universal gas constant	$[\mathrm{J}/(\mathrm{mol} \cdot \mathrm{K})]$
T	Temperature	[°C] / [K]
$\dot{V}$	Volume flow rate	$[\mathrm{m}^3/\mathrm{s}]$
V	Volume	$[\mathrm{m}^3]$
$\dot{W}$	Power	[W]
α	Charge transfer coefficient	[-]
γ	Pre-exponential factor	$[\mathrm{A}/\mathrm{m}^2]$
δ	Layer thickness	[m]
η	Efficiency	[-]
ρ	Density	$[\mathrm{kg}/\mathrm{m}^3]$
σ	Activation energy	[kJ/mol]
ϕ	Porosity	[-]
χ	Production capacity	[kg/h]
ψ	Fugacity coefficient	[atm]
Δ	Change	[-]
Φ	Electrical resistivity	[Ωm]

Sub-/superscript	Description
x_A	Anode
x_{act}	Activation (overpotential)
x_{bed}	Catalyst bed
x_{bp}	Bulk phase
x_C	Cathode
x_{cat}	Catalyst
x_{cell}	Electrolysis cell
x_{conc}	Concentration (overpotential)
x_E	Electrolyte
x_{gen}	Generated
x_{ohm}	Ohmic (overpotential)
x_i	Species
x_{in}	Input
x_{req}	Required
x_{stack}	Electrolysis stack
x_{tn}	Thermoneutral
x_{tot}	Total
x_{tpd}	Triple phase boundary
x°	Standard state at 25°C and 1 atm
x^{op}	Operational
x^{cap}	Capital

Chemical Species	Description
Ar	Argon
BZY	Yttrium-doped Barium Zirconate
CO_2	Carbon Dioxide
e^-	Electron
H^+	Hydrogen ion
H_2	Hydrogen
H_2O	Water
KOH	Potassium Hydroxide
N_2	Nitrogen
NH_3	Ammonia
Ni	Nickel
O^{2-}	Oxygen ion
O_2	Oxygen
OH^-	Hydroxide ion
YSZ	Yttrium Stabilised Zirconia

Abbreviations

Abbreviation	Description
AEA	Aspen Energy Analyser
AEC	Alkaline Electrolysis Cell
APEA	Aspen Process Economic Analyser
ASU	Air Separation Unit
BAU	Business As Usual
CAPEX	Capital Expenditures
CASU	Cryogenic Air Separation Unit
CCS	Carbon Capture and Storage
CCUS	Carbon Capture, Utilisation and Storage
EU	European Union
FE	Faradaic Efficiency
GHG	Greenhouse Gas
GHSV	Gas-Hourly Space Velocity
HB	Haber-Bosch
HBR	Haber-Bosch Reactor
HER	Hydrogen Evolution Reaction
HEX	Heat Exchanger
HHV	Higher Heating Value
HP	High-Pressure
HPC	High-Pressure Column
HT	High-Temperature
IPCC	Intergovernmental Panel on Climate Change
IRENA	International Renewable Energy Agency
LCOA	Levelised Cost Of Ammonia
LHV	Lower Heating Value
LPC	Low-Pressure Column
LT	Low-Temperature
MAT	Minimum Approach Temperature
MER	Minimum Energy Requirement
MILP	Mixed-Integer Linear Programming
MSHX	Multi-Stream Heat Exchanger
OER	Oxygen Evolution Reaction
OPEX	Operational Expenditures
PBR	Packed-Bed Reactor
PCFC	Proton-Conducting Fuel Cell
PEMEC	Proton Exchange Membrane Electrolysis Cell
PFD	Process Flow Diagram
P-SOEC	Proton-Conducting Solid-Oxide Electrolysis Cell
PtX	Power-to-X
RES	Renewable Energy Source
SMR	Steam-Methane Reforming
SOEC	Solid-Oxide Electrolysis Cell
SOFC	Solid-Oxide Fuel Cell
TRL	Technology Readiness Level
WGS	Water-Gas Shift

Contents

1 | Introduction

In light of the accelerating consequences of climate change caused primarily by anthropogenic greenhouse gas (GHG) emissions, there is an urgent need for ambitious strategies to support the green transition. To avoid the most severe effects of global warming, the Paris Agreement aims to keep the global average temperature increase below 2 °C, preferably 1.5 °C, compared to pre-industrial levels [1]. However, projections from the Intergovernmental Panel on Climate Change (IPCC) [1] indicate a sharp rise in global temperatures, increasing the need for bold climate action to accommodate the Paris Agreement and reach targets like net-zero carbon emissions in 2050 set by the European Union (EU) [2]. This requires a transformation across all sectors. Certain industrial and transport sectors face significant technological and economic barriers to direct electrification, making decarbonisation more challenging. According to the International Renewable Energy Agency (IRENA) [3], these hard-to-abate sectors include road freight transport, shipping, aviation, iron and steel, and chemicals and petrochemicals. Together, these five sectors account for approximately 24% of global energy consumption and 20% of the total CO_2 emissions, distributed as seen in Figure 1.1.

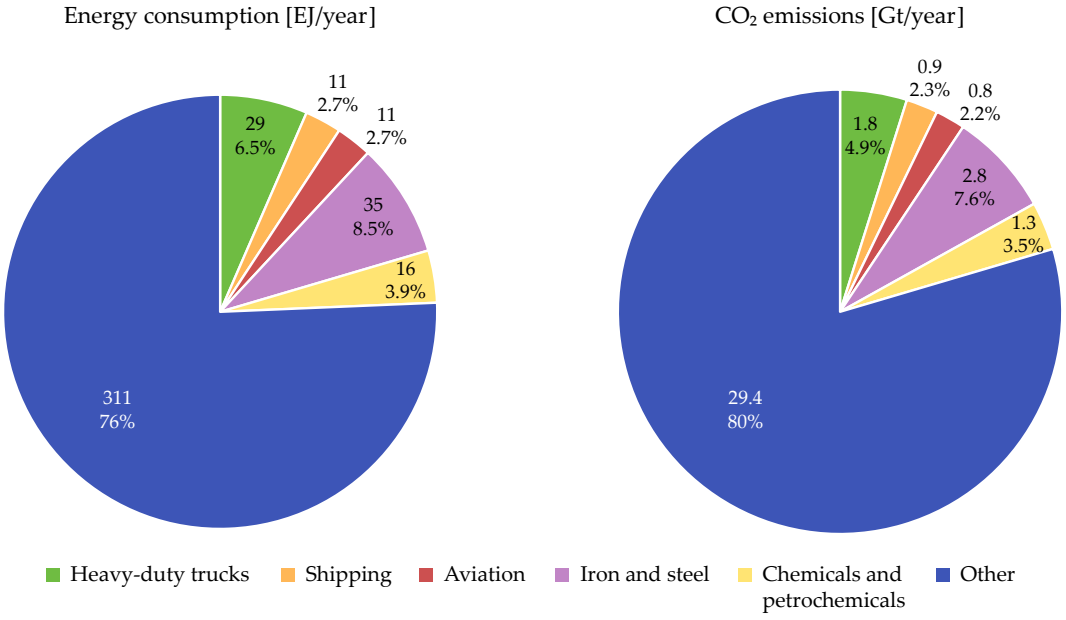

Figure 1.1: The hard-to-abate sectors distribution regarding global energy consumption and total CO_2 emissions. Data from [3].

Decarbonising these sectors requires a variety of approaches, all related to renewable energy, energy efficiency improvements, and carbon capture, utilisation and storage (CCUS). According to IRENA [3], one key approach, particularly relevant in shipping and aviation, is *the indirect use of clean electricity via synthetic fuels and feedstock*. This concept, known as power-to-X (PtX), involves indirect electrification by producing renewable hydrogen [3]. Besides using pure hydrogen, two synthetic fuels, known as e-fuels, are highlighted in the shipping industry: methanol and ammonia. Hydrogen primarily applies to short-distance shipping, since it requires frequent refuelling due to a low volumetric energy density,

leading to storage limitations [4]. The volumetric energy density for various fuels is visualised in Figure 1.2a, distinguishing between carbon-based and zero-carbon fuels. The exception to hydrogen is when it is liquefied and stored cryogenically, which significantly increases its volumetric energy density. This results in more compact storage but requires more energy for storage conditioning [5]. Figure 1.2b illustrates the various energy storage options in terms of storage capacity and duration, highlighting the potential of long storage periods and a wide range of storage capacities for chemical storage compared to other storage technologies [6]. This is important to consider for medium to long-distance shipping.

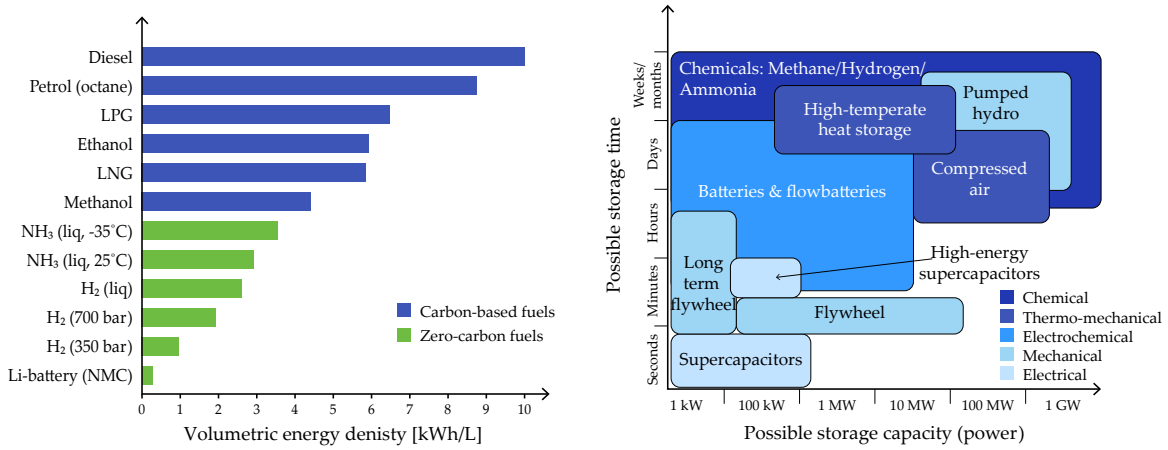

(a) Volumetric energy densities of a range of fuel options [7]. **(b)** Energy storage comparison against time and capacity [7].

Figure 1.2: Different fuel and energy storage options, highlighting ammonia as a high-energy-density, zero-carbon fuel, and chemical storage as a long-period, high-capacity energy storage option. Data from [5] and [8].

Methanol, in comparison to hydrogen, is suitable for medium to long-distance shipping, is easy to store, and can be retrofitted to existing ships. Possibly the most significant challenge facing e-methanol is the carbon content. A biogenic carbon source is required to produce green e-methanol, thereby necessitating the addition of potentially expensive carbon capture technologies. Reliance on a biogenic carbon source is not ideal for long-term decarbonisation, as this resource can become scarce quickly. In contrast, ammonia is a carbon-free fuel that also has an existing global infrastructure, due to its role in the fertiliser industry. Ammonia is ideal for long-distance shipping, as it has a higher volumetric energy density than hydrogen, increasing onboard storage capacities. Although the toxicity of ammonia causes safety concerns, these are considered manageable given the existing large-scale handling of ammonia [4]. However, when utilising ammonia in internal combustion engines, other challenges arise regarding nitrogen oxide emissions, high combustion temperature, and slow flame speed, leading to the use of dual-fuel engines [8]. Still, with ammonia's carbon-free composition and role in an already established global economy, it is considered here as an interesting option for sustainable shipping.

Green ammonia for e-fuel purposes remains in the earlier stages of development (considering both production and combustion technologies), while the large-scale production of so-called grey ammonia is widespread due to its role in the fertiliser industry. Conventionally, ammonia is produced via the Haber-Bosch (HB) process - an artificial nitrogen fixation process - which accounts for approximately 1.8% of global CO_2 emissions [5, 9]. This stems primarily from the water-gas shift (WGS) reaction and the energy-intensive steam methane reforming (SMR) process used to produce grey hydrogen. SMR alone

accounts for around 80% of the total energy consumption in a conventional fossil-fuel-based ammonia plant, making ammonia production the most CO_2-intensive industrial chemical process in the world [5]. To decarbonise this industry and thereby enable green ammonia production, replacing SMR with renewable hydrogen via water electrolysis is currently the most mature and widespread option. To ensure fully green ammonia production, a renewably powered air separation unit (ASU) is also necessary to produce nitrogen for the process. The value chain for green ammonia production is illustrated in Figure 1.3.

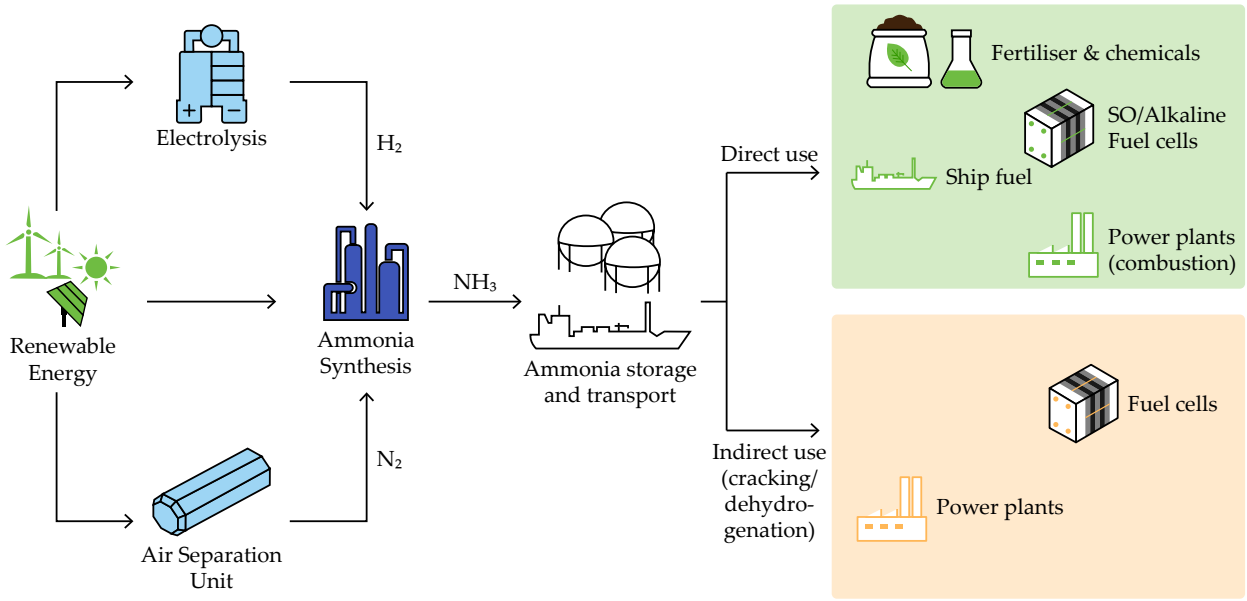

Figure 1.3: Overview of the green ammonia value chain from renewable energy to form H_2 and N_2, synthesised to NH_3 to some possible end-uses, including energy transport, direct use, and indirect use. Figure inspired by [5, 7].

Several technologies for water electrolysis are available, each offering distinct advantages and limitations. The most prominent are alkaline electrolysis (AEC) and proton exchange membrane electrolysis (PEMEC), both of which are low-temperature (LT) technologies with high technology readiness levels (TRLs). In contrast, solid oxide electrolysis cells (SOECs) operate at high temperatures and can provide higher electrical efficiencies if available thermal energy is utilised. [10] However, besides being less mature than AEC and PEMEC, the SOEC technology also faces durability issues due to high thermal stress. Therefore, researchers are investigating SOECs operating at lower temperatures to address this issue, consequently leading to lower efficiencies, creating an operational optimisation problem.

In the context of green ammonia production, coupling a high-temperature (HT) steam electrolysis technology with the exothermic ammonia synthesis process presents an interesting opportunity for heat integration. SOECs are particularly relevant in this context, both in the intermediate and high-temperature ranges. Therefore, this report focuses on investigating the potential synergies and techno-economic advances arising from the heat integration of a coupled ammonia synthesis and SOEC-based hydrogen production plant, with an emphasis on enabling the decarbonisation of the maritime industry.

1.1 Technology Overview

To gain knowledge of how a coupled SOEC-ammonia synthesis plant can help in the decarbonisation of the maritime industry, it is essential to understand the mechanisms behind the central processes. In this technology overview, this is achieved through the analysis of SOEC-based water electrolysis and green ammonia synthesis. The overview will focus on the working principles of the processes and present both advancements and limitations of the technologies in question.

1.1.1 Water Electrolysis for Green Hydrogen Production

Hydrogen is the most abundant element in the universe, but is not found on Earth in its pure form. Instead, it is bound into molecules, such as water and hydrocarbons, methane in particular [11]. Free hydrogen is obtained by splitting these molecules, creating several routes for hydrogen production that involve various renewable and fossil-based energy sources. In the route of green hydrogen production, water electrolysis is the most established technology; however, it can also be achieved using technologies such as thermolysis, photolysis, and biomass gasification. These methods are not yet as developed and are unavailable on an industrial scale. [12] This report only considers the route of green hydrogen production through water electrolysis. In water electrolysis, the electrochemical conversion of water and electricity into hydrogen and oxygen takes place in an electrolysis cell according to the following overall reaction: [13]

$$2\,H_2O \rightleftharpoons 2\,H_2 + O_2 \tag{1.1}$$

An electrolysis cell consists of two electrodes, an anode (positive electrode) and a cathode (negative electrode), separated by an electrolyte. AEC is the most mature technology that utilises a liquid electrolyte, achieving an electrical efficiency of around 70% based on the lower heating value (LHV), and is generally the most cost-effective option among the three types. In PEMEC, an acidic ionomer electrolyte is used, and is more expensive than AEC due to the use of platinum-group metal catalysts, but has a higher electrical efficiency of around 80%. It is predicted that this efficiency can increase up to 94% as this technology advances [10]. The SOEC uses a ceramic oxide electrolyte material and operates at around 700 to 1100 °C using steam instead of liquid water, reaching cell efficiencies close to 100% [14], but with a lower electrical efficiency of around 55%, since this technology is less developed [10, 13]. The electrical efficiency of an SOEC can be increased significantly if freely available heat is supplied to the process [15]. The general process is the same in all three types of electrolyser cells: Water is fed into an electrochemical cell where a sufficiently high voltage is applied, forming hydrogen at the cathode and oxygen at the anode through the so-called hydrogen evolution reaction (HER) and oxygen evolution reaction (OER), respectively. A comparison of both the technical and application aspects of the three electrolysis types is provided in Table 1.1. The different efficiencies used in this report are defined in Appendix A.1, while the TRL definitions are given in Appendix A.2.

Table 1.1: Comparison between the general AEC, PEMEC and SOEC technologies in terms of both technical and application aspects. *TRL 3-4 in nuclear applications [14].

	AEC	**PEMEC**	**SOEC**
Technical Aspects			
Efficiency (LHV) [10]	62-82%	67-82%	50-60%
Operating temp. [10]	40-90 °C	20-100 °C	700-1100 °C
Operating pressure [10]	1-30 bar	<70 bar	Atmospheric
Stack lifetime [14]	60,000-100,000 h	50,000-90,000 h	20,000-50,000 h
Electrolyte [14]	Aqueous KOH (20-40 wt%)	Solid acidic polymer	Solid ceramic oxide
Charge carrier [10]	OH^- ions	H^+ protons	O^{2-} ions
HER [10]	$H_2O + 2\,e^- \rightarrow H_2 + 2\,OH^-$	$2\,H^+ + 2\,e^- \rightarrow H_2$	$H_2O + 2\,e^- \rightarrow H_2 + O^{2-}$
OER [10]	$2\,OH^- \rightarrow \frac{1}{2}\,O_2 + H_2O + 2\,e^-$	$H_2O \rightarrow \frac{1}{2}\,O_2 + 2\,H^+ + 2\,e^-$	$O^{2-} \rightarrow \frac{1}{2}\,O_2 + 2\,e^-$
Application Aspects			
TRL [12, 14]	9	9	5-8*
Advantages [10, 15]	• Well-established tech • Cheapest and cost-effective • Long-term durability • Simple design	• High voltage efficiency • Compact (high current density) • High-purity H_2 • Fast response times	• Potential for near-100% voltage efficiency • Non-noble catalyst • Fast response times
Challenges [10, 15]	• Large footprint • Low current density • Gas crossover • Caustic environment	• Expensive components • Corrosive environment • Membrane degradation • Limited lifetime	• Less mature tech • Lower durability • Thermal cycling issues • Complex system design
Typical Application [15]	Industrial H_2 production	On-site H_2 production, lab and military use.	Coupling with nuclear/-solar/industrial thermal power.

Besides a high cell efficiency, SOEC offers other advantages compared to the LT technologies. Regarding material costs, the ceramic oxide electrolyte contains inexpensive and readily available materials, such as zirconium, iron, manganese, and stainless steel. Nickel (Ni) and cobalt are also extensively used, which can be an issue due to their scarcity. However, compared to AEC, which uses pure Ni and Ni-based materials, SOEC uses four times less of the material [10, 13]. One challenge of SOEC is that the technology is less developed, with lower durability due to high thermal stress on components. Currently, the technology is undergoing significant development as companies begin to build commercial-scale SOEC plants and large production factories, such as Haldor Topsoe's SOEC factory in Herning, Denmark, scheduled to start production in 2025 [16].

1.1.1.1 Solid Oxide Electrolysis Cell

From a thermodynamic point of view, a high temperature is desirable in electrolysis operation, since the minimum amount of electrical energy that must be supplied is reduced significantly as it can be replaced by thermal energy [15]. This is favourable when HT heat is available as a waste product from other processes, facilitating the integration of SOEC with heat from industrial processes. The relationship between operating temperature and the energy required for the decomposition of water during electrolysis is expanded in Appendix A.3.

The working principle of an SOEC is illustrated in Figure 1.4, displaying an electrochemical cell with a feed of water that is converted into H_2 and O_2 through the HER and OER using renewable electricity. Figure 1.4a highlights the electrolyte material that, according to Smolinka et al [15], is often used for the SOEC: Yttria-stabilised zirconia (YSZ) solid ceramic oxide. The cathode and anode are made of a ceramic metal compound (cermet) material, often YSZ-based. YSZ is a material that provides good mechanical strength and high oxygen-ion conductivity at temperatures above 800 °C. Figure 1.4b highlights the OER and HER facilitated by the anode and cathode, respectively, along with the oxygen-ion and electron flows.

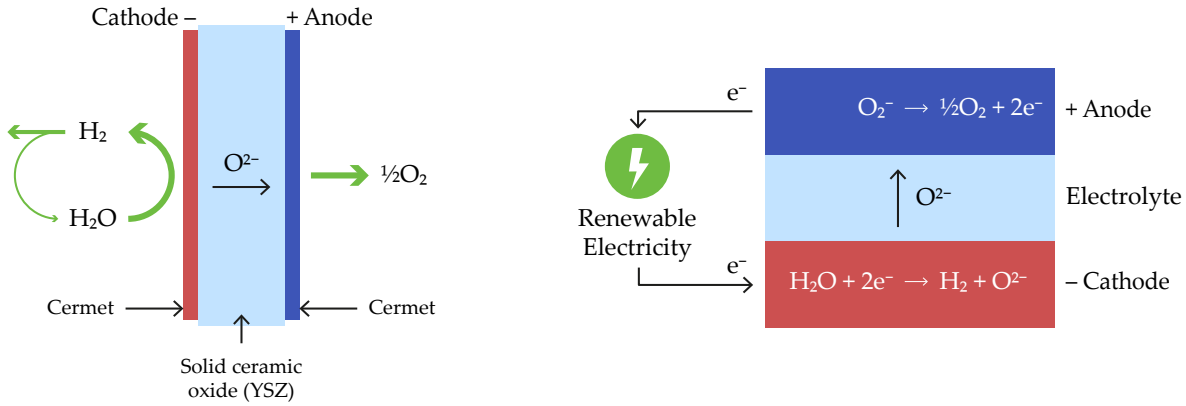

(a) SOEC principle with recirculation and typical materials.

(b) SOEC with reactions and ion flows.

Figure 1.4: Working principle of an SOEC, showing the cell consisting of the two electrodes (anode and cathode) and the electrolyte with energy and compound flows, including H_2 recirculation at the cathode. Figures inspired by [14].

While a high temperature is favourable in electrolysis operation, since the Faradaic efficiency (FE) increases with temperature, leading to a higher conversion of water, a lower or intermediate temperature causes less thermal stress on the materials, potentially solving durability issues of the cells. Some literature [14, 17] mentions SOECs operating at intermediate temperatures down to 500 °C; however, the configuration of this type of SOEC is slightly different, as they are proton-conducting (or hydrogen-ion conducting) rather than oxygen-ion conducting.

Proton-conducting solid oxide electrolysis cells (P-SOECs) are less mature than SOECs and have a lower cell efficiency, but draw benefit from the intermediate operating temperature (300-700 °C [18]), not only accommodating durability issues of the HT SOECs, but also decreasing the energy input to the cell [19]. The working principle of a P-SOEC is illustrated in Figure 1.5, showing an electrochemical cell similar to that of the SOEC seen in Figure 1.4 with a feed of water that is converted into H_2 and O_2 through the HER

and OER defined in Figure 1.5b using renewable electricity. The difference here is that water enters at the anode, where the OER creates oxygen and hydrogen ions that are conducted through the electrolyte to the cathode, where the HER creates hydrogen. Figure 1.5a illustrates the electrolyte material that is often used for the P-SOEC: Barium Zirconate Yttria (BZY) solid ceramic oxide, which provides a high proton conductivity [18, 19]. The anode and cathode are often made of a BZY-supported cermet material.

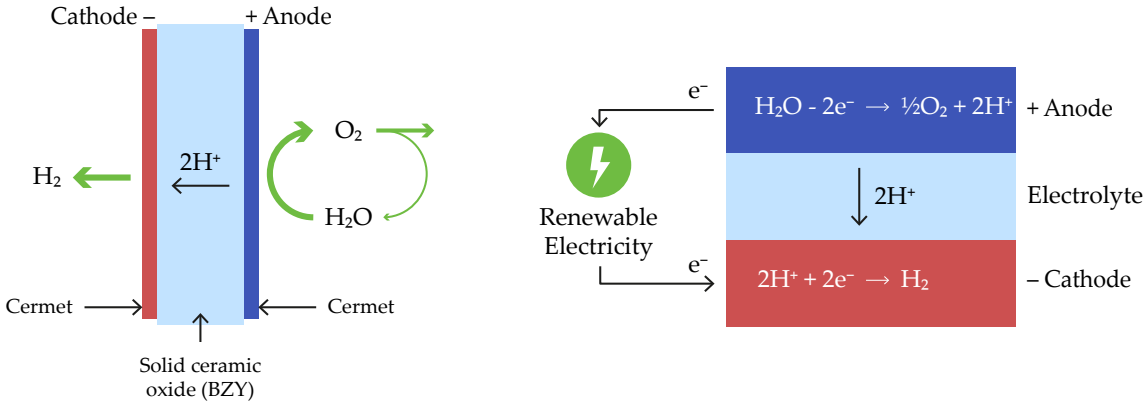

(a) P-SOEC principle with recirculation and typical materials.

(b) P-SOEC with reactions and ion flows.

Figure 1.5: Working principle of a P-SOEC, showing the cell consisting of the two electrodes (anode and cathode) and the electrolyte with energy and compound flows, including O_2 recirculation at the cathode.

1.1.1.2 SOEC Development Perspective

The SOEC is often described as a less mature technology compared to AEC and PEMEC. This is true when looking at the current capacity of SOEC systems installed in pilot and demonstration projects, ranging from around 100 kW to 10 MW [14]. However, assessing the commercial readiness of the SOEC technology based on these projects alone is unjustifiable, as it is almost identical to solid oxide fuel cell (SOFC) designs. SOFCs have already been commercialised in GW-scale for backup power generation and microgrid applications [14]. Therefore, multiple companies working on SOFC development are also showing interest in the SOEC technology. This is accelerating the development of SOECs, as design experience is already extensive at companies in the SOFC field, such as Haldor Topsoe. An overview of companies active in the SOEC area is provided in Table 1.2, including a description of their SOEC technology, estimated typical capacity, and notable projects they are currently working on.

Table 1.2: Overview of companies in the field of SOEC, including a technical description of their respective technology, the typical capacities, and notable projects they are collaborating on.

Company	Tech Description	Typical Capacity	Notable Projects
Sunfire [20, 21]	YSZ ceramics and Ni-based electrodes; operates around 850-900 °C with 88% electrical efficiency (LHV).	HyLink 10 MW SOEC module.	• MultiPLHY 2.4 MW SOEC project using industrial waste heat • e-CO_2Met (TotalEnergies) 0.7 MW SOEC for e-methanol • GrInHy3.0 SOEC project using waste heat from steelmaking
Haldor Topsoe [16, 22]	Ni – YSZ composites; operates around 675-825 °C targeting >90% efficiency; optimised for integration with industrial heat sources.	Modular stacks used in multi-MW scale.	• Nuclear heat integration with Rolls-Royce small modular reactors • Herning 500 MW SOEC factory
DynElectro [23]	YSZ-based stacks with heat-tolerant coatings and AC:DC operation to improve thermal stress handling and lifetime.	Test on 30-cell stack; 1 MW system (in development with SolydEra)	• SolydEra 1 MW hydrogen/ammonia system.
Elcogen [24]	Ceramic electrolytes supported by stainless steel; operation around 650-750 °C with >85% efficiency.	Small stacks used in pilot systems (around 100 W-10 kW)	• SYRIUS steel industry heat integration • Convion >85% efficiency test with HT steam.
Mitsubishi Heavy Industries [25, 26]	Large-scale; Ni – YSZ cells and HT steel hardware; tested in controlled pilot environments.	400 kW test system	• Takasago Hydrogen Park 400 kW SOEC test using HT steam.

From Table 1.2 it is apparent that most SOEC projects involve another HT process used for heat integration to produce HT steam for the SOEC system. Moreover, a tendency to build modular SOEC stacks is observed as a consequence of limited stack sizes resulting from the irreversible compression of the stack layers. The HT operation of an SOEC necessitates robust compression to maintain optimal contact between the stack layers, which can cause damage to the ceramic material, leading to the assembly of smaller modules [27]. This modularity creates a technology that can cover a wide range of capacities from kW-scale singular stacks to modules used in multi-MW scale projects. These findings highlight the possibility of coupling hydrogen production via SOEC with ammonia production, as is also explored in projects involving companies such as DynElectro and Haldor Topsoe.

1.1.2 Haber-Bosch Synthesis for e-Ammonia Production

According to Smith et al. [9], the most mature (TRL 6-8 [7]) and widespread alternative for carbon-free ammonia production is to replace SMR in the conventional HB-process with water electrolysis to produce green hydrogen, and by adding an ASU for nitrogen production. Ensuring an electricity input to the entire system based solely on renewable energy, this is referred to as the green HB process in this report, often defined in literature as the electrically driven HB process [9]. A comparison between the methane-fed and green (electrically driven) HB process is shown in Figure 1.6, highlighting the differences in complexity between the systems.

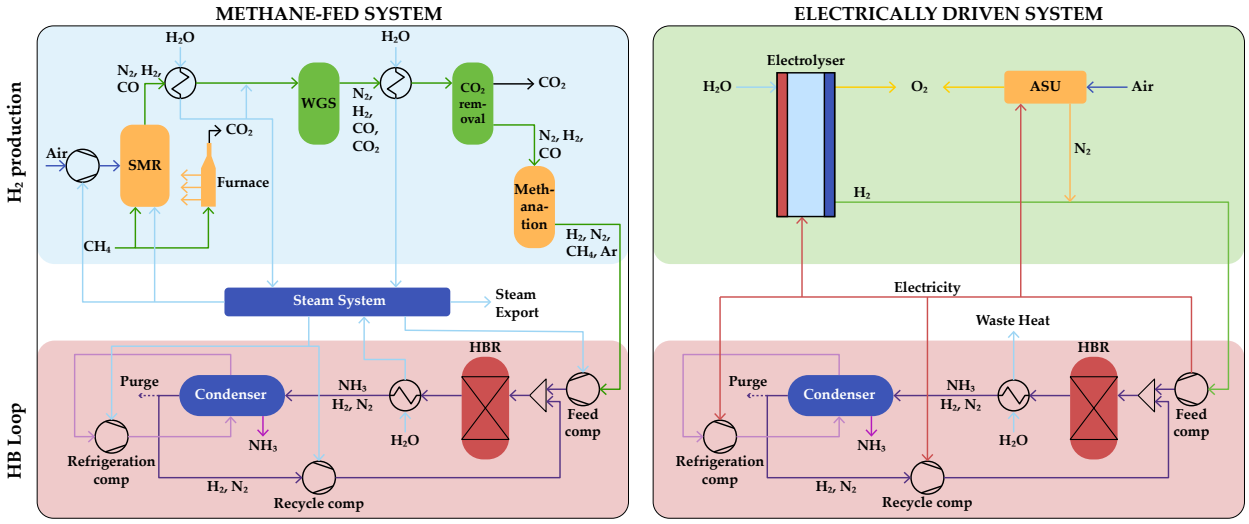

Figure 1.6: System diagram of a typical conventional methane-fed HB system (left) and a green/electrically driven system (right). WGS: Water-gas shift reactor. Figure inspired by [7, 9].

Another route to e-ammonia production includes the less-developed absorption-enhanced ammonia synthesis with TRL 3-6 [7]. According to Palys et al. [28], this technology is a promising alternative to the green HB process as it has the potential to reduce both capital and operational costs of the system, introducing a pressure 10 times lower than that of the traditional reaction-condensation HB loop (as seen in Figure 1.6). The high pressure and temperature needed to synthesise ammonia in the HB reactor (HBR) of around 150-300 bar and 400-500 °C lead to the use of expensive system components like multi-stage high-pressure (HP) compressors. If the pressure is reduced in the reactor, the single-pass conversion also decreases, along with the temperature needed for ammonia condensation to separate it from the unreacted hydrogen and nitrogen in the HB loop. Replacing the condenser with an ammonia absorber addresses this challenge in the absorbent-enhanced system. However, this system is more convenient in small-scale ammonia production, making it less ideal for large-scale maritime e-fuel production.

Several other routes to green ammonia production that do not rely on water electrolysis also exist, showing considerable promise for the future role of ammonia [29]. An overview of these technologies is provided in previous work [7]. With a focus on the heat integration potential between steam electrolysis and ammonia synthesis, this report does not further investigate the concepts that do not rely on electrolysis. Considering the production of green e-ammonia for the shipping industry, a mature route that

enables large-scale production is the most relevant choice. This delimitation makes the green HB process the most favourable, primarily due to it being the most developed technology, but also due to its reliance on electrolysis.

1.1.2.1 Synthesis Reaction & Equilibrium Limitations

Ammonia synthesis is governed by the following exothermic reaction:

$$N_2 + 3\,H_2 \rightleftharpoons 2\,NH_3 \qquad \Delta H^{\circ}_{rxn} = -46\,\mathrm{kJ/mol_{NH_3}} \tag{1.2}$$

where ΔH°_{rxn} is the heat of reaction per mole of NH_3 at standard conditions. Since the ammonia synthesis reaction requires a high temperature (400-500 °C) to overcome the energy necessary to break the chemical bonds [30], and the reaction is exothermic, the temperature can reach relatively high values over the length of the reactor. With an increase in temperature, the reaction rate decreases, limiting the equilibrium conversion in the reactor. This favours a lower operating temperature of around 400 °C in the HBR. As mentioned, a decrease in pressure has the same effect as an increase in temperature: limiting the equilibrium conversion. This leads to a preference for higher pressures in the reaction kinetics, but this is less attractive since it increases the energy consumption and component costs of the system [28].

Due to the equilibrium limitations of the ammonia synthesis reaction, an optimisation problem arises when considering an SOEC-HB integrated system, since the SOEC favours higher operating temperatures to maximise the conversion of water. Operating the HBR at a higher temperature enables it to cover a higher percentage of the latent heat required for steam generation in the SOEC, but at the cost of limited ammonia production. Lowering the temperature of the SOEC also enables the HBR to cover a higher percentage of the latent heat required, but results in reduced hydrogen production. Thus, there is a trade-off between higher hydrogen or higher ammonia production when setting the operation temperature of the two systems. Here, it is especially interesting to compare the integration of both an SOEC and a P-SOEC, since the waste heat from the HBR can be more thermally compatible for heat integration with the P-SOEC. In addition to considering the optimal operating conditions of a coupled system, it is also important to consider the scale of ammonia production. In the context of e-fuel for maritime applications, a large-scale production case is considered.

1.1.2.2 Case: Large-Scale Production of Marine E-Ammonia

According to the 2020 Ammonfuel report [31] - discussing the use of ammonia as a marine fuel from an industrial point of view - it is estimated that 25-50% of marine fuel should be replaced by e-ammonia by 2050. In an example of a 30% replacement, it is estimated that 55 Mton of e-ammonia is to be produced in new plants, without accounting for upscaling of the non-fuel ammonia market. The size of these new plants highly depends on the electrolysis capacity. The capacity of conventional ammonia plants is in the range of 1000-2400 $\mathrm{ton_{NH_3}/day}$, which requires a hydrogen supply of 177-425 $\mathrm{ton_{H_2}/day}$ by stoichiometry. Using an example of an SOEC plant with 60% electrical efficiency (LHV-based), based on the typical

range given in Table 1.1, this is equivalent to a 410-985 MW SOEC plant.

Currently, the largest SOEC plant is in the scale of 2.4 MW and is operated by Sunfire [20], who has also announced the production of 10 MW modules, leaving some capacity to be desired for this scale. However, the capacity of electrolysis plants is increasing rapidly [32], and designs of 1 GW AEC and PEMEC systems are already developed [33]. With the rapid increase in SOEC plant capacities [34], it is considered that the construction of a 500 MW SOEC plant by 2050 is reasonable, aiming to produce e-ammonia in a capacity comparable to conventional ammonia plants.

1.2 Literature Review on SOEC Heat-Integrated Systems

With the central technologies in green ammonia production presented, the following section focuses on reviewing relevant literature on SOEC heat-integrated systems. In 2017, Cinti et al. [35] published one of the first studies on a coupled SOEC-HB system, aiming to improve green ammonia production by utilising the HT waste heat from an HBR in the SOEC process. Up until then, most work had limited focus on integrating water electrolysis and the HB loop for green ammonia production [35]. A 40% power input reduction was achieved compared to equivalent plants, using an HBR under heavy conditions (650 °C and 550 bar), which enabled it to cover 98% of the heat required for the electrolysis reaction. Operating the HBR at this high a temperature decreases the conversion efficiency of the reactor, which is why the pressure is elevated as well to counteract this effect. Operating at a high pressure of 550 bar does come with some safety risks, but this is also observed in other industrial ammonia production plants [36]. The HT and HP processes entail quite a high energy demand along with safety and handling issues. In Cinti et al. [35], comparing the SOEC-HB integrated process using the heavy-conditioned HBR to both a conventional SMR-based HB plant and LT electrolysis HB (LT-EL-HB) plant, revealed a higher overall system efficiency of 93.4% (with LT-EL-HB at 92.33% and SMR-HB at 61.12%).

More generally, the work of Wang et al. [37] and Wu et al. [38] focuses on heat integration of an SOEC system with an industrial heat source, to estimate the change in plant performance of this addition. Wang et al. [37] found that using waste heat from a diesel engine could increase the electrical efficiency from 73.12% to 85.17%. The study also found that operating the SOEC at 800-1000 °C significantly improved the electrical efficiency over a wide range of current densities compared to operating at 600 °C. At an operating temperature of 1000 °C and current density of 11,600 A/m^2, an electrical efficiency of 94.52% was achieved, implying that an optimum between operating temperature, current density, and electrical efficiency can be found, but this optimum differs between integration cases.

Wu et al. [38] investigated SOEC heat integration for industrial waste heat recovery, operating the SOEC in thermoneutral mode to maintain isothermal operating conditions. The study investigated the most suitable operating point for increased system efficiency and hydrogen production by optimising the relationship between steam flow rate, temperature, and current density. It was found that operating the cell at 800 °C with an inlet steam flow rate of 50 kg/h increased the performance of the system, leading to an SOEC energy efficiency of 93.1% and an electrical efficiency of 106.4% based on the higher heating value

(HHV). This is equivalent to an electrical efficiency of around 89.6% based on the LHV.

The literature study on SOEC heat-integrated systems emphasises the potential of producing green ammonia through HT steam electrolysis, enabling heat integration between the processes for increased efficiency, and reduced energy consumption and operating costs. Early studies, such as Cinti et al. [35], demonstrate the feasibility of coupling SOEC with the HB loop under HT and HP operating conditions, while works by Wang et al. [37] and Wu et al. [38] illustrate the benefits of optimal SOEC operating parameters on system performance. However, several research gaps remain, of which some are highlighted here:

- Integrated SOEC-HB systems beyond early-stage conceptual studies are explored to a small extent, leaving research gaps about scalability, operational feasibility, and economic feasibility.
- Research conducted on extreme operating conditions in the HBR to accommodate the high temperature of the SOEC instead of exploring lower temperature SOEC operation.
- Most studies focus solely on conventional oxygen-ion SOECs, while P-SOECs, which may offer advantages in heat integration with the HBR, remain unexplored in this context.

Addressing these research gaps is essential for developing energy- and cost-efficient SOEC-based green ammonia production systems. Therefore, it is interesting to analyse the impact of varying the SOEC operating temperature on the overall system efficiency of green ammonia production. Here, it is relevant to consider both the standard SOECs (oxygen-ion conducting) and the P-SOECs (proton-conducting).

1.2.1 SOEC Temperature Considerations & Faradaic Efficiencies

It has been established that a higher operating temperature (around 800-1100 °C) increases the electrolysis cell efficiency and thereby the hydrogen production, while ammonia synthesis favours lower operating temperatures (around 400-500 °C) to increase the ammonia yield due to equilibrium conversion limitations. To investigate the impact of the SOEC operating temperature on system performance, it is essential to have a relation that describes the temperature-efficiency dependency. The cell efficiency (η_{cell}) is a product of the voltage efficiency (η_{vol}) and the Faradaic efficiency (η_F) of the cell:

$$\eta_{cell} = \eta_{vol} \cdot \eta_F \qquad \eta_{vol} = \frac{E_{tn}}{E_{cell}} \tag{1.3}$$

where ΔH_{rxn} is the heat of reaction at the cell operating temperature, F is the Faraday constant, and E_{cell} is the cell operating voltage. An overview of the different efficiencies and their definitions is provided in Appendix A.1. Literature often considers a Faradaic efficiency (FE) of 100%, since HT SOECs operate close to this value [39, 40]. However, when considering LT P-SOECs (considered LT for steam electrolysis), the FE reduces significantly, mainly due to the concept known as electronic leakage [41]. Unfortunately, no direct formula exists that connects the cell operating temperature to the FE; thus, this value must be determined based on experimental values. There are some uncertainties associated with using these experimental values, as they depend heavily on the specific design and materials used in the given cell.

This, combined with a lack of available literature on FE in SOECs and P-SOECs, also complicates making an accurate relation between the operating temperature and the FE. In this report, it is chosen to look at two operating cases based on available literature data: An HT SOEC operating at 800 °C and a LT P-SOEC operating at 500 °C. A thermoneutral operating mode, at which the electrolysis reaction is in equilibrium, is considered for both cases. This mode ensures isothermal operation of the cells at which point the voltage efficiency is equal to 100%.

Jin et al. [18] report FE values between around 40 and 70%, depending on the cell operating voltage, for a BZY-based P-SOEC operating at 500 °C. Operating in thermoneutral mode, the FE reaches a value of around 53.8%. Conversely, Duan et al. [39] report high FE values in the range of 96 to 99% for a YSZ spinel-based SOEC operating between 700 and 800 °C. When considering thermoneutral operation at 800 °C, the FE is estimated to be 96.8%. The difference in FE values between the presented SOEC and P-SOEC sources is quite significant, creating an interesting trade-off in the presented cases.

Based on these findings, the focus of this report is to investigate heat integration in an SOEC-HB coupled system, aiming to optimise system performance by considering the SOEC operating mode. Consequently, four cases are compared, considering both SOEC/P-SOEC operation and with/without heat integration:

1. HT SOEC without heat integration (SOEC-B)
2. HT SOEC with heat integration (SOEC-INT)
3. LT P-SOEC without heat integration (P-SOEC-B)
4. LT P-SOEC with heat integration (P-SOEC-INT)

The cases are compared both in terms of their technical and economic feasibility. The economic aspect is highly relevant, since the price of SOEC and P-SOEC stacks varies, and the degradation of these must also be considered. Besides enabling comparisons between cases, this also allows for comparisons of the green ammonia plant with conventional and similar green ammonia plants. This focus presents a novel approach to estimating the techno-economic feasibility of steam electrolysis-HB integrated systems, aiming to expand on the research provided by previous studies such as Cinti et al. [35], Wang et al. [37], and Wu et al. [38]. The following chapter presents the focus of this report in the form of a problem statement, which is analysed and answered in the subsequent chapters.

2 | Problem Statement

The primary focus of this report is to model a green ammonia production plant by integrating the waste heat from the HBR with an SOEC or P-SOEC to enhance the overall energy efficiency and minimise production costs for maritime e-fuel applications. The green ammonia production plant consists of three central processes: hydrogen production via steam electrolysis, nitrogen production via cryogenic air separation, and ammonia synthesis through the HB process. In this plant setup, four cases are considered: Using an HT SOEC with and without heat integration, and using an LT P-SOEC with and without heat integration. Based on this system, the following problem statement is formulated:

How can a coupled Haber-Bosch and solid oxide electrolysis plant be operated to reduce energy consumption and increase the overall energy efficiency of green ammonia production through heat integration?

The problem statement is solved through the following work questions:

1. How can the ammonia plant be modelled to estimate the impact of heat integration when operating with an HT SOEC and an LT P-SOEC?
2. Which of the four mentioned cases is more technically feasible in terms of electricity consumption and global plant efficiency?
3. What is the economic feasibility of the four mentioned cases when compared to other green ammonia production plants and conventional grey ammonia production?

Report Structure

The solution to the problem statement is provided through the following report structure: Chapter 3 introduces the integrated SOEC-HB system configuration, the associated process modelling approach in Aspen Plus and mathematical models developed for the different cases. Chapter 4 presents the technical performance of the systems, along with an economic feasibility study and its results. Chapter 5 discusses the achieved results and uncertainties of these, while Chapter 6 provides a conclusion to the findings of this report, and Chapter 7 delves into the future research directions.

3 | Integrated SOEC-HB System

This chapter presents a description of the processes involved in the four case configurations considered for green ammonia production with steam electrolysis in the form of SOECs or P-SOECs. While multiple cases are analysed, the processes of nitrogen production and ammonia synthesis are the same for all. The description comprises the designed system configuration, process modelling of system components in Aspen Plus, and a mathematical modelling approach, including electrochemical electrolysis models and a kinetic ammonia synthesis model.

3.1 Overall System Configuration

A diagram of the SOEC-HB integrated system concept is illustrated in Figure 3.1, comprising three subsystems: (1) the electrolysis system for hydrogen production, (2) the cryogenic air separation unit (CASU) for nitrogen production, and (3) the HB loop for ammonia synthesis.

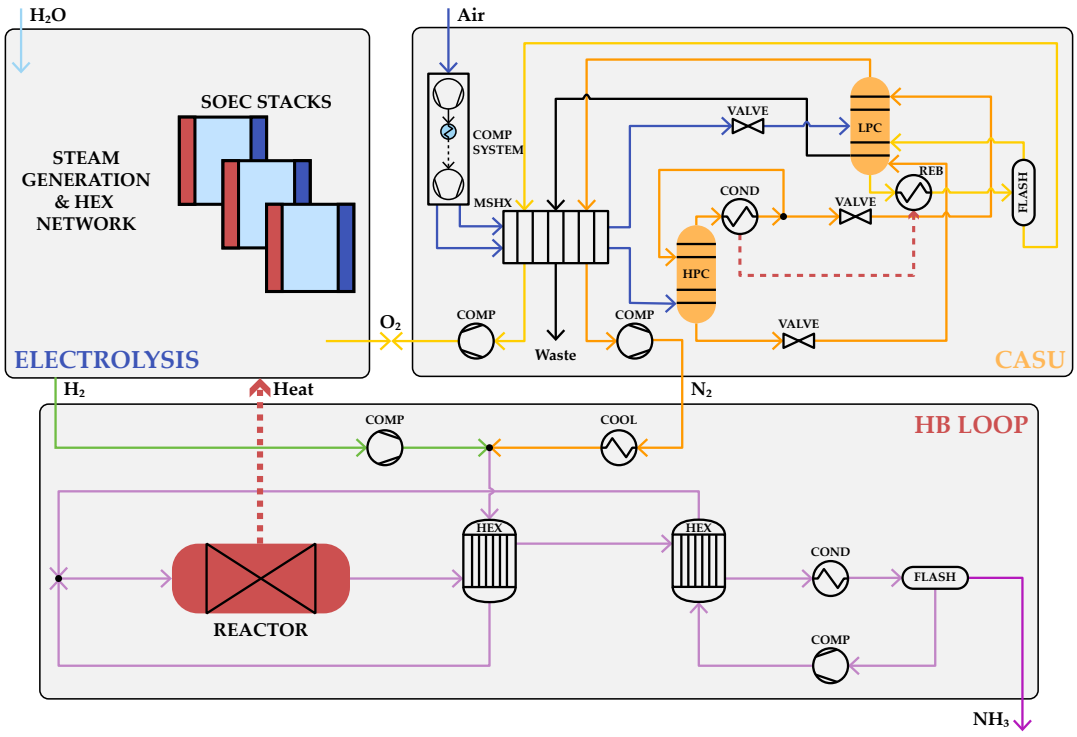

Figure 3.1: Overview of the SOEC-HB integrated system concept, divided into the three subsystems modelled in Aspen Plus: The Electrolysis system, the CASU, and the HB loop.

It is seen from Figure 3.1 that the electrolysis system is not fully defined, as the steam generation and heat exchanger (HEX) network must be determined for each case. This network depends on whether the SOEC or P-SOEC setup is used, as the options for internal heat exchange differ, and whether heat integration with the HBR is considered. For both the HT and LT cases, the HB loop and CASU models

are constructed using the same approach. The HB loop and CASU model are both based on Aspen Plus system models developed and verified by Asgharian et al. [42]. The approach to modelling the system seen in Figure 3.1 is to:

1. Create process models of the subsystems, applying overall mass and energy balances using Aspen Plus,
2. Create more detailed models of the electrolysis cells using mathematical models developed in MATLAB, and implement the results of these in the Aspen models,
3. Define ammonia synthesis reaction kinetics for implementation in the Aspen HB loop process model, and
4. Use Aspen Process Economic Analyser (APEA) to provide the required inputs to conduct an economic analysis and calculate the levelised cost of ammonia (LCOA).

The first step of the modelling approach is expanded in the following section.

3.1.1 Aspen Plus Modelling Approach

Each of the subsystems is built separately in Aspen Plus, using the output of N_2 and H_2 from the CASU and SOEC models, respectively, as input for the HB loop. The chosen property method for the system models is Peng-Robinson, as this method is ideal for non-polar and real component systems. The process models are constructed by defining each component from the blocks available in Aspen. Since no electrolysis units are available in the version of Aspen used (V12.1), the cells are simulated using an RStoic block (stoichiometric reactor), defining the fractional conversion of the electrolysis reaction, based on the FE determined from literature. To simulate the products leaving the cathode and anode, a separator block is used, assuming 100% separation efficiency of the electrolyte (only the ions it is designed to conduct travel through it). An overview of how the SOEC and P-SOEC stacks are simulated in Aspen Plus is seen in Figure 3.2.

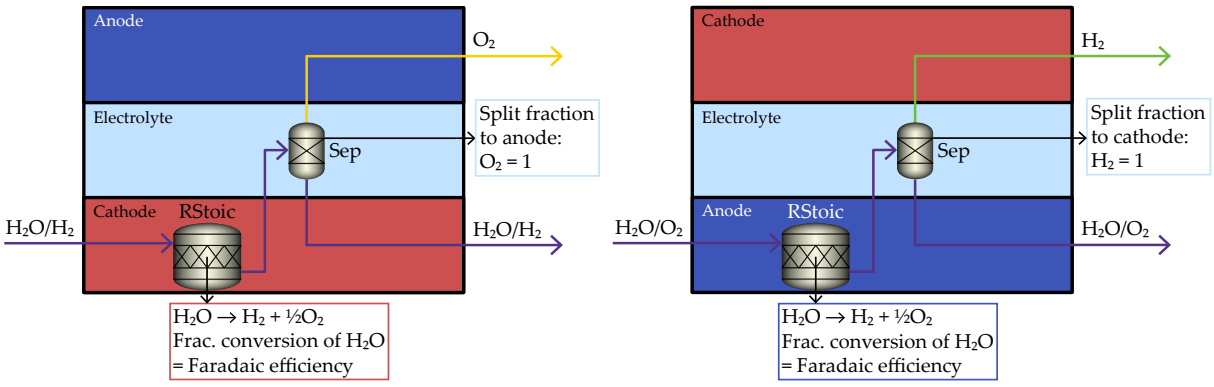

(a) SOEC model approach in Aspen.

(b) P-SOEC model approach in Aspen.

Figure 3.2: Components and settings used for SOEC and P-SOEC stack models in Aspen Plus.

The only input required from the electrochemical model to the RStoic component, besides operating temperature and pressure, is the Faradaic efficiency. The entire electrolysis system also requires the cal-

culated inlet flow rate of water and recycle flows. These parameters are all presented in Section 3.3.1 and summarised in Table 3.5.

The remaining system components are modelled as follows: The HBR is modelled as an RPlug block, simulating a packed-bed reactor (PBR) operating isothermally and with a pressure drop defined by the Ergun equation. The reaction kinetics used as input to this block are presented in Section 3.3.2 along with the reactor dimensions. All compressors are modelled using a polytropic method with a polytropic efficiency of 80% [38], whereas the pumps are modelled with a 75% efficiency. The HEXs are modelled as shell-and-tube HEXs with a pressure drop of 0.05 bar on the cold and hot side and a minimum approach temperature (MAT) of 5 °C. Similarly, all coolers and heaters are modelled with a pressure drop of 0.05 bar. For the electric heater, an efficiency of 98% is assumed [37]. These values are all summarised in Table 3.1.

Table 3.1: Overview of input parameters to flow component modelling in Aspen.

System parameter	Value	Unit
Electric heater efficiency	98	%
Water pump efficiency	75	%
Compressor polytropic efficiency	80	%
HEX pressure drop (e/s)	0.05	bar
Heater/cooler pressure drop	0.05	bar
MAT	5.0	°C

To ensure high energy efficiency in the constructed electrolysis subsystems, HEX networks are designed to utilise as much of the internal heat duty as possible. The HEX networks in the HT SOEC and LT P-SOEC systems are optimised using the Aspen Energy Analyser (AEA) application. As a baseline for developing the networks, the HEX network presented by Wu et al. [38] is used. Firstly, minor alterations were made to accommodate the available temperatures in the system streams, after which AEA determined the minimum energy requirement (MER) network by solving a mixed-integer linear programming (MILP) problem. The MER is the theoretical minimum amount of hot and cold utilities needed for maximum heat recovery, determined through a pinch analysis. [43] In Appendix C.3, the results generated by AEA after achievement of the MER networks are illustrated for all four cases. This means that the actual utility use is equivalent to the targeted utility use. Thus, the complete subsystems have been developed, and the associated processes are described next.

3.2 Process Description of Subsystems

A CASU is chosen as this is the most well-known approach for nitrogen production and proven to be the most cost-effective solution [44, 45]. The CASU takes dry air, composed of 78.1% nitrogen, 20.95% oxygen, and 0.95% argon, as an input and separates it into nitrogen, oxygen, and a waste product using an HP distillation column (HPC) and an LP distillation column (LPC). As seen in the process flow diagram (PFD) illustrated in Figure 3.3, the dry air is firstly compressed to 6 bar and water-cooled, after which it is

split into a minor stream (stream 4) that is further compressed to 12 bar and cooled, and a major stream (stream 7).

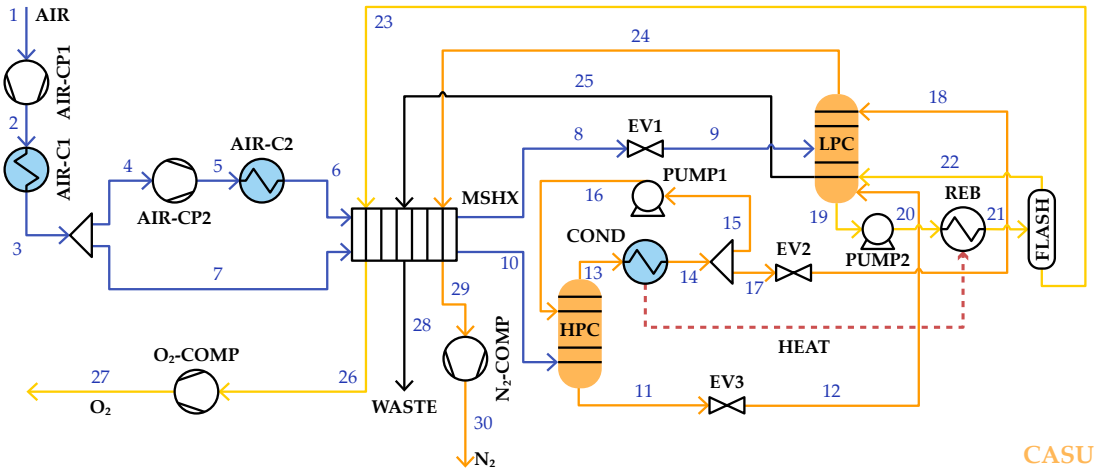

Figure 3.3: Detailed PFD of the CASU, based on Asgharian et al. [42].

Both the major and minor streams enter a multi-stream heat exchanger (MSHX) in which they are cooled to a low temperature of -166 °C, liquefying the minor stream. The minor stream is then expanded to 1.35 bar (stream 8) before it enters the LPC operated at cryogenic conditions. The expansion of the minor stream results in a significant temperature reduction, providing the required refrigeration to maintain cryogenic conditions in the LPC. This is necessary for the condensation of oxygen, causing it to separate from the nitrogen in the dry air. The major stream is transferred directly from the MSHX to the HPC (stream 10), from which a rich nitrogen stream exits at the top (stream 13), where it is liquefied in a condenser and partially recycled into the HPC (stream 16), directing the remaining to the LPC after expansion to 1.35 bar (stream 18). A rich nitrogen stream leaving the bottom of the HPC (stream 11) is also expanded to 1.35 bar before entering the LPC. From the bottom of the LPC, an oxygen-rich liquid stream (stream 19) exits, as oxygen has the highest boiling point among the air components. This stream is heated in a reboiler, which is heat-integrated with the condenser, and directed to a flash tank (stream 21), separating the stream into liquid oxygen directed to the MSHX (stream 23) and oxygen gas recycled to the LPC (stream 22). A nitrogen-rich cryogenic gas stream exits at the top of the LPC and is directed into the MSHX (stream 24), along with a waste stream also exiting the LPC (stream 25).

In the MSHX, cooling the air streams causes a temperature increase in the liquid oxygen stream, nitrogen gas stream, and waste gas stream, causing them to exit at ambient temperature. The oxygen stream (stream 26) is then compressed and ready for tank storage, while the waste stream is vented to the atmosphere (stream 28), and the nitrogen stream is compressed and forwarded into the HB system (stream 30). Before entering the HB loop seen in Figure 3.4, the nitrogen stream is cooled using cooling water (CW) and mixed with compressed hydrogen (stream 55).

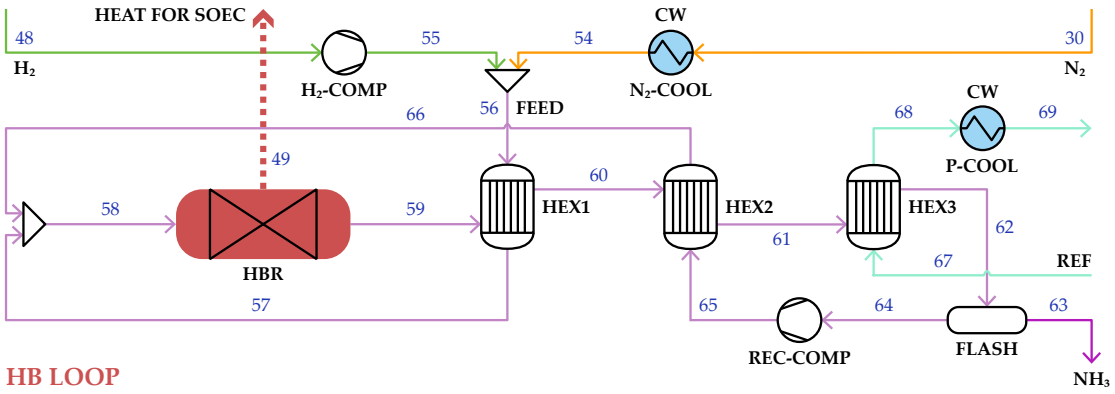

Figure 3.4: Detailed PFD of the HB loop, based on Asgharian et al. [42].

In the HB loop, the hydrogen-nitrogen feed mixture enters the system at a temperature of around 445 °C and pressure of 150 bar (stream 56). The feed is firstly guided into HEX1, where it is heated to the reactor operating temperature of 450 °C and directed into the reactor (stream 58). In the reactor, the feed mixture reacts over an iron-based catalyst bed to form ammonia. The product gas (stream 59), now consisting of a mixture of hydrogen, nitrogen and ammonia, enters two HEXs where it is used to firstly heat the inlet feed stream (HEX1) and then to pre-heat the recycled gas stream (HEX2). It is then cooled to -18 °C to condense the ammonia content using a refrigerant in HEX3, after which a flash tank is used to separate the liquid ammonia (stream 63) from the remaining gas mixture, which is recycled (stream 64). The recycle stream is re-pressurised and led back through HEX1 and HEX2 to the reactor (stream 66), where it is mixed with the feed stream, creating the HB loop.

3.2.1 HT SOEC System & Stream Results

In the HT SOEC system illustrated in Figure 3.5, clean water is pumped into a HEX network (stream 32), increasing the pressure of the stream to 1.263 bar. The temperature of the water stream is then increased through HEX1 to HEX3 to create HT steam. In the case of heat integration (SOEC-INT), an additional HEX is added (HBR-HEX) between HEX2 and HEX3. Before the steam enters the SOEC at the cathode, an electric heater is used to reach the operating temperature of 800 °C. Inside the SOEC, the HT steam is now split into pure oxygen, exiting at the anode (stream 50), and a hydrogen-steam mixture, exiting at the cathode (stream 39). At the anode, some of the oxygen is recycled and used as a sweep gas (stream 51) to avoid build-up in the anode [38, 46]. At the cathode, some of the hydrogen is separated from the hydrogen/steam mixture and recycled into the cathode stream (stream 40). The remaining gas mixture is used to heat the water in HEX3 (stream 41), after which it is compressed to 20 bar, water-cooled, and then used to heat the water again in HEX2. The mixture then enters a condenser (stream 45) and is separated into hydrogen gas (stream 48), ready to be transferred to the HB loop, and water (stream 47) using a flash tank. Furthermore, the oxygen that is not recycled at the anode is used to heat the water in HEX1 (stream 52).

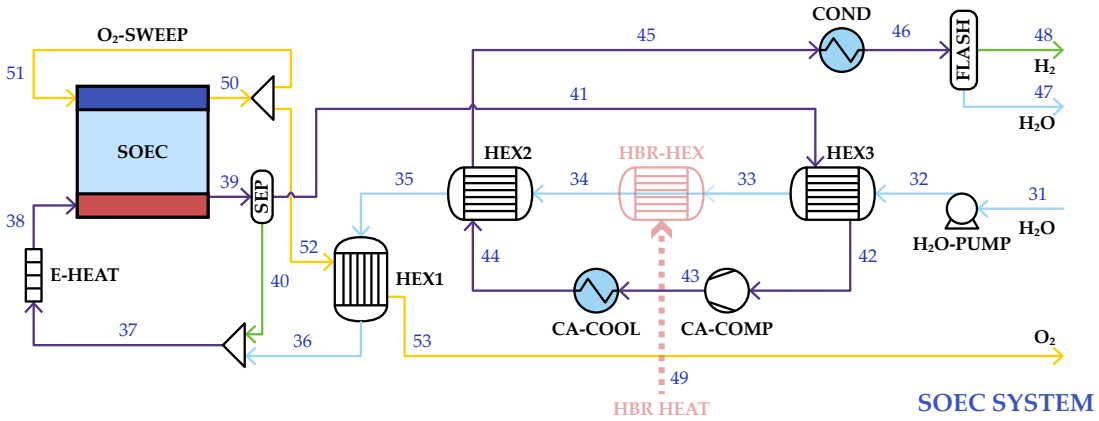

Figure 3.5: Detailed PFD of the HT SOEC system, illustrating the HEX network both with and without heat integration with the HBR, adding the HBR-HEX to the system in the case of heat integration.

The primary challenge of operating the system at 800 °C is the durability of the components. HT compressors often cannot operate within this inlet temperature range, as the outlet temperature will escalate. Thus, it is necessary to cool the hydrogen/steam mixture before compression to ensure that the compressor operates at a realistic temperature for the available materials. HEX3 ensures that the temperature is decreased to 50 °C (stream 42) before compression, while CA-COOL decreases the temperature after compression to 600 °C before entering HEX2.

The resulting temperature, pressure, and composition of the key streams of the complete HT system are presented in Table 3.2. The streams of the HT system, comprising the CASU, the HB loop, and the SOEC, are summarised for both the non-integrated (SOEC-B) and integrated case (SOEC-INT) in Table 3.2. It is noted that the only element in the key streams changing between the SOEC-B and SOEC-INT case is the temperature of stream 36 (steam temperature before mixing with recycle stream and electric heating in SOEC). For the SOEC-B case, the internal heating of the SOEC system is sufficient to evaporate the water, raising its temperature to 119.2 °C. Whereas, for the SOEC-INT case, the temperature reaches 649.6 °C due to the heat supplied from the HBR, leading to a much lower heating requirement of the electric heater in this system.

From Table 3.2 it is also seen that the nitrogen exiting the CASU (stream 30) is only 99.91 mol%$_{N_2}$ pure. Moreover, the hydrogen exiting the SOEC (stream 48) contains a trace amount of water (0.129 mol%$_{H_2O}$), since it is not completely condensed from the hydrogen/steam mixture. As a consequence, the green ammonia produced in the HB loop contains 99.24 mol%$_{NH_3}$, the rest being a small amount of the O_2, Ar and H_2O transferred from the CASU and SOEC, including remains of H_2 and N_2.

Table 3.2: Temperature, pressure, and composition of the key streams from the HT systems: SOEC-B and SOEC-INT. The stream numbers align with the PFDs in Figure 3.3, Figure 3.4, and Figure 3.5.

HT Case												
		CASU		SOEC						HB LOOP		
Stream number		1	30	31	36	36-INT	39	47	48	58	59	63
Temperature	[°C]	15.00	1213	15.00	119.2	649.6	800.0	20.00	20.00	444.7	450.0	-18.00
Pressure	[bar]	1.013	150.0	1.013	1.063	1.063	1.013	20.00	20.00	149.9	149.3	149.2
Flow rate	[kmol/s]	1.027	0.641	1.984	1.984	1.984	2.204	0.116	1.922	8.458	7.182	1.287
Composition	[mol%]											
H_2		0	0	0	0	0	97.12	0.302	99.87	74.02	60.52	0.383
N_2		78.10	99.91	0	0	0	0	0	0	24.12	19.52	0.137
O_2		20.95	0.008	0	0	0	0	0	0	0.035	0.042	0.004
NH_3		0	0	0	0	0	0	0	0	1.643	19.71	99.24
H_2O		0	0	100	100	100	2.880	99.70	0.129	0.029	0.035	0.192
Ar		0.950	0.085	0	0	0	0	0	0	0.153	0.180	0.042

3.2.2 LT P-SOEC System & Stream Results

The LT P-SOEC system seen in Figure 3.6 requires the same number of HEXs as the HT SOEC system, but has quite a different configuration due to the gas flows from the P-SOEC. Again, pure water is pumped, increasing the pressure to 1.263 bar, into a HEX network (stream 32) to create LT steam, adding the HBR-HEX in the case of heat integration (P-SOEC-INT). Before entering the P-SOEC anode, the electric heater is used to increase the temperature to the required 500 °C (stream 38). The P-SOEC reaction mechanism then splits the steam into pure hydrogen at the cathode (stream 43) and an oxygen-steam mixture at the anode (stream 39). Some of the oxygen is then separated from the mixture and recycled into the steam entering the anode (stream 40). The remaining oxygen-steam mixture is used to heat the water in HEX2 (stream 41) before it exits the system. The dry hydrogen exiting at the cathode is first used to heat the water in HEX1, before it is compressed to 20 bar, water-cooled, and used to heat the water in HEX3 (stream 47). The hydrogen stream is then ready to enter the HB loop.

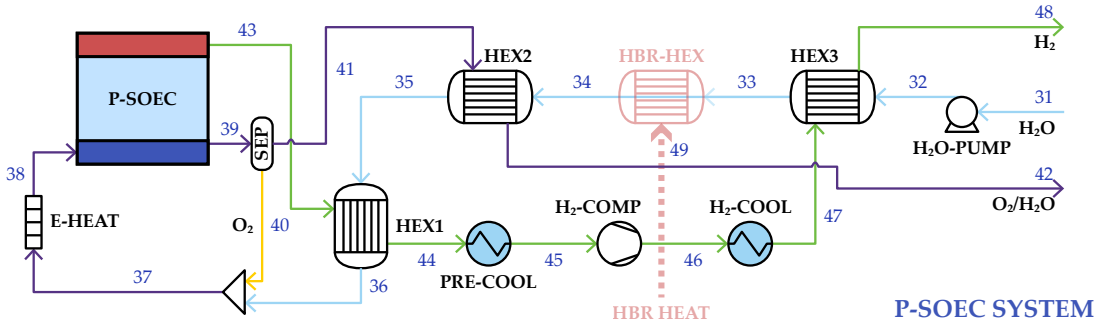

Figure 3.6: Detailed PFD of the LT P-SOEC system, illustrating the HEX network both with and without heat integration with the HBR, adding the HBR-HEX to the system in the case of heat integration.

Even as the P-SOEC system operates at a lower temperature than the SOEC system, component durability must still be considered to ensure that realistic materials can be used. Thus, a compression pre-cooler, reducing the temperature to 60 °C, and a pre-cooler to HEX3 (H_2-COOL), reducing the temperature to 600 °C, are added to the system. The primary difference between the non-integrated and integrated systems in both the HT and LT systems, aside from the addition of the HBR-HEX, is the power required to be supplied to the electric heater to achieve the required temperatures.

The streams of the LT system, comprising the CASU, the HB loop, and the P-SOEC, are summarised for both the non-integrated (P-SOEC-B) and integrated case (P-SOEC-INT) in Table 3.2. In the LT system, there is no difference in the temperature of key stream 36 (steam temperature before mixing with recycle stream and electric heating in P-SOEC) between the two cases. This is due to the reduced available internal heat duty of the P-SOEC system due to a lower operating temperature. This causes the water to still be in the process of evaporating at this point, with or without adding the heat duty from the HBR. Of course, the water in the P-SOEC-INT case is closer to being fully evaporated, since more energy has been supplied to cover the required heat of vaporisation, leading to a lower heating requirement of the electric heater in this system.

Table 3.3: Temperature, pressure, and composition of the key streams from the LT systems: P-SOEC-B and P-SOEC-INT. The stream numbers align with the PFDs in Figure 3.3, Figure 3.4, and Figure 3.6.

LT Case												
		CASU		**P-SOEC**						**HB LOOP**		
Stream number		1	30	31	36	36-INT	39	42	48	58	59	63
Temperature	[°C]	15.00	1213	15.00	99.95	99.95	500.0	107.6	20.00	444.9	450.0	-18.00
Pressure	[bar]	1.013	150.0	1.013	1.063	1.063	1.013	0.963	20.00	149.9	149.4	149.2
Flow rate	[kmol/s]	1.030	0.644	3.587	3.587	3.587	3.021	2.623	1.929	8.502	7.220	1.289
Composition	[mol%]											
H_2		0	0	0	0	0	0	0	100	17.55	12.21	0.047
N_2		78.10	99.91	0	0	0	0	0	0	78.31	53.57	0.227
O_2		20.95	0.008	0	0	0	45.11	36.77	0	0.140	0.140	0.008
NH_3		0	0	0	0	0	0	0	0	3.281	33.37	99.62
H_2O		0	0	100	100	100	54.89	63.23	0	0	0	0
Ar		0.950	0.086	0	0	0	0	0	0	0.712	0.712	0.101

From Table 3.3, it is seen that the purity of the N_2 stream leaving the CASU (stream 30) is the same as in the HT system, but that there is a difference in molar composition of the H_2 supplied to the HB loop (stream 48). With the P-SOEC electrolyte being hydrogen-ion (H^+) conducting, completely separating the H_2 from the steam mixture, there is no water entering the HB loop, slightly increasing the purity of the ammonia product to 99.62 $mol\%_{NH_3}$.

3.3 Mathematical Models

For both the HT and LT cases, the electrochemical reaction in the cell is modelled using a script in MATLAB, as the version of Aspen Plus used (V12.1) does not include built-in electrolysis components. This is then simulated using an RStoic reactor in Aspen Plus, providing the flows found from the script and determined FE for the given case. For the reaction kinetics used in the HBR, Aspen Plus offers options to define these parameters directly in the RPlug reactor component. This section presents the mathematical models used to determine the SOEC and HBR reaction mechanisms.

3.3.1 Electrochemical Electrolysis Models

Both the SOEC and P-SOEC operate under thermoneutral conditions, meaning that the operating voltage equals the thermoneutral voltage. The operating voltage (E_{cell}) of the SOEC can be determined from:

$$E_{cell} = E_{eq} + E_{ohm} + E_{act} + E_{conc} \tag{3.1}$$

where E_{eq} is the equilibrium potential, E_{ohm} is the ohmic overpotential, E_{act} is the activation overpotential, and E_{conc} is the concentration overpotential. The thermoneutral voltage (E_{tn}) is determined from the reaction enthalpy (ΔH_{rxn}) at the given operating temperature [38]:

$$E_{tn} = \frac{\Delta H_{rxn,T}}{2 \cdot F} \tag{3.2}$$

$$\Delta H_{rxn,T} = 3.49 \cdot \frac{T}{1000} + \frac{9.82}{2} \cdot \left(\frac{T}{1000}\right)^2 - \frac{11.65}{3} \cdot \left(\frac{T}{1000}\right)^3 + \frac{3.20}{4} \cdot \left(\frac{T}{1000}\right)^4 - 1.53 \cdot \left(\frac{T}{1000}\right)^{-1} + 244.07 \tag{3.3}$$

The efficiency of the cell, which defines the H_2O conversion, is determined from the FE, as the voltage efficiency is 100% in the thermoneutral operation mode. Since no relation defines the FE as a function of temperature, experimental values found in literature [18, 39] are used for the given operating conditions, as described in Section 1.2.1. Since the thermoneutral voltage is used, it is not necessary to find the equilibrium potential and overpotentials to find the operating voltage. However, these are still calculated to determine the polarisation curve, which can be used to verify the model. The Nernst equation expresses the equilibrium potential [38]:

$$E_{eq} = E^0 + \frac{R_u \cdot T}{2 \cdot F} \ln \left(\frac{\frac{p_{H_2}}{P_{std}} \cdot \left(\frac{p_{O_2}}{P_{std}}\right)^{0.5}}{\frac{p_{H_2O}}{P_{std}}} \right) \tag{3.4}$$

where R_u is the universal gas constant, p_i is the partial pressure (of species i =H_2, O_2, H_2O), and P_{std} is the standard pressure (1 atm). E^0 is the open cell potential at standard conditions, which for a temperature range of 500-1500 °C [37] can be expressed as:

$$E^0 = -1.253 + 2.4516 \times 10^{-4} \cdot T \tag{3.5}$$

Assuming that the change in electrical resistivity is constant, the ohmic overpotential can be defined by [37]:

$$E_{ohm} = I \cdot \delta_E \cdot \Phi \qquad \Phi = 2.99 \times 10^{-5} \cdot \exp\left(\frac{10300}{T}\right) \tag{3.6}$$

where I is the current density, δ_E is the electrolyte layer thickness, and Φ is the electrical resistivity of the electrolyte given by equation (3.6).

The total activation overpotential is a summation of the activation overpotential at the anode ($E_{act,A}$) and cathode ($E_{act,C}$), derived from the Butler-Volmer equation of the anode and cathode reactions [37]:

$$E_{act,A} = \frac{R_u \cdot T}{\alpha_A \cdot F} \sinh^{-1}\left(\frac{I}{2 \cdot I_{0,A}}\right) \qquad I_{0,A} = \gamma_A \cdot \exp\left(\frac{-\sigma_{a,A}}{R_u \cdot T}\right) \tag{3.7}$$

$$E_{act,C} = \frac{R_u \cdot T}{\alpha_C \cdot F} \sinh^{-1}\left(\frac{I}{2 \cdot I_{0,C}}\right) \qquad I_{0,C} = \gamma_C \cdot \exp\left(\frac{-\sigma_{a,C}}{R_u \cdot T}\right) \tag{3.8}$$

where I_0 is the exchange current density governed by the Arrhenius equation, α is the charge transfer coefficient, γ is the pre-exponential factor, and σ_a is the activation energy, all defined for both the anode and cathode.

Similarly, the total concentration overpotential is a summation of the concentration overpotential at the anode ($E_{conc,A}$) and cathode ($E_{conc,C}$). For the SOEC these are defined in equation (3.9), and for the P-SOEC in equation (3.10) [44]:

$$\text{SOEC:} \qquad E_{conc,A} = \frac{R_u \cdot T}{2 \cdot F} \ln\left(\sqrt{\frac{p_{O_2,tpb}}{p_{O_2,bp}}}\right) \qquad E_{conc,C} = \frac{R_u \cdot T}{2 \cdot F} \ln\left(\frac{p_{H_2O,bp} \cdot p_{H_2,tpb}}{p_{H_2O,tpb} \cdot p_{H_2,bp}}\right) \tag{3.9}$$

$$\text{P-SOEC:} \qquad E_{conc,A} = \frac{R_u \cdot T}{2 \cdot F} \ln\left(\frac{p_{O_2,tpb}^{0.5} \cdot p_{H_2O,bp}}{p_{O_2,bp}^{0.5} \cdot p_{H_2O,tpb}}\right) \qquad E_{conc,C} = \frac{R_u \cdot T}{2 \cdot F} \ln\left(\frac{p_{H_2,bp}}{p_{H_2,tpb}}\right) \tag{3.10}$$

where $p_{i,tpb}$ and $p_{i,bp}$ are the partial pressures (of species i =H_2, O_2, H_2O) at the triple phase boundary and in the bulk phase, respectively. The calculation of $p_{i,tpb}$ and $p_{i,bp}$ is found in Appendix B.1 and B.2, respectively, for both the SOEC and P-SOEC configuration.

3.3.1.1 SOEC & P-SOEC Mole Balances

To determine the required flows of the SOEC and P-SOEC system, a mole balance is established for each case, ensuring mass conservation within the system. The generated mole flows of a singular stack are determined by [44]:

$$\dot{n}_{\mathrm{H_2},gen} = \frac{A_{cell} \cdot I \cdot N_{cells}}{2 \cdot F} \qquad \dot{n}_{\mathrm{O_2},gen} = \frac{A_{cell} \cdot I \cdot N_{cells}}{4 \cdot F} \tag{3.11}$$

where A_{cell} is the cell surface area and N_{cells} is the number of cells per stack. The models are designed to generate the same amount of hydrogen and oxygen, resulting in a difference in the required water input due to a difference in the conversion of water. The required H_2O flow is determined from the FE:

$$\dot{n}_{\mathrm{H_2O},req} = \frac{\dot{n}_{\mathrm{H_2},gen}}{\eta_F} \tag{3.12}$$

The remaining mole flows are determined using a simple mass balance over the streams surrounding the cells. An overview of this is given in Appendix B.2. To find the total generated H_2 and O_2 flows and required H_2O flow of the entire 500 MW electrolysis plant, equations (3.11) and (3.12) are simply multiplied by the number of stacks in the system.

3.3.1.2 Sizing & Model Inputs

To determine the number of stacks required for a 500 MW system, the power of one stack ($\dot{W}_{stack}$) is first determined from the cell power ($\dot{W}_{cell}$):

$$\dot{W}_{stack} = \frac{\dot{W}_{cell} \cdot N_{cells}}{\eta_{ACDC}} \qquad \dot{W}_{cell} = E_{tn} \cdot I \cdot A_{cell} \tag{3.13}$$

where η_{ACDC} is the AC/DC conversion efficiency. The number of stacks is then found by dividing the 500 MW by the stack power and rounding off to the closest integer greater than or equal to this value. The design parameters used for the SOEC and P-SOEC cells are based on literature using similar operating conditions to those of this report. They are summarised in Table 3.4, along with the operating conditions, stream compositions, and overpotential parameters.

Table 3.4: Overview of the input parameters to the electrochemical electrolysis model for the HT and LT case.

		SOEC	P-SOEC	Sources
Operating Conditions				
Operating Temperature, T	[°C]	800	500	[18, 39]
Operating pressure, P	[bar]	1.013	1.013	[18, 39]
Thermoneutral voltage, $E_{tn,@T}$	[V]	1.288	1.276	Calculated
Current density, $I_{@E_{tn}}$	[A/cm^2]	4.541	0.192	[18, 38]
Faradaic Efficiency, η_{FE}	[%]	96.80	53.77	[18, 39]
Stream Composition				
Feed stream composition, x_i	[mol%]	90 H_2O / 10 H_2	90 H_2O / 10 O_2	[38]
Sweep gas composition, x_i	[mol%]	100 O_2	-	[38]
Anode recycle ratio, $\dot{n}_{an,rec}/\dot{n}_{an,gen}$	[mol%]	25	-	[46]
Design Parameters				
Electrolyte layer thickness, δ_E	[µm]	12.5	50	[37, 47]
Cell surface area, A_{cell}	[cm^2]	400	100	[37, 38]
Number of cells per stack, N_{cells}	[-]	1500	2000	[37, 38]
AC/DC conversion efficiency, η_{ACDC}	[%]	95	95	[38]
Overpotential Parameters				
Pre-exponential factor anode, γ_A	[A/m^2]	2.051×10^9	2.5363×10^7	[37, 48]
Pre-exponential factor cathode, γ_C	[A/m^2]	1.344×10^{10}	6.7212×10^7	[37, 48]
Activation energy anode, $\sigma_{a,A}$	[kJ/mol]	120	100	[37, 48]
Activation energy cathode, $\sigma_{a,C}$	[kJ/mol]	100	100	[37, 48]
Charge transfer coefficients, α	[-]	0.5	0.5	[48, 49]
Electrical resistivity, Φ	[Ωm]	2.031×10^{-9}	4.710×10^{-12}	[37, 48]

3.3.1.3 SOEC Model Verification & Results

Using the open cell voltage found from the electrochemical model at thermoneutral voltage and the corresponding current density seen in Table 3.4, the polarisation curves of the SOEC and P-SOEC are found. The equilibrium potential and overpotentials are found for a range of current densities, resulting in the cell operating voltage development seen in Figure 3.7 for both an SOEC and P-SOEC. These polarisation curves are then compared to literature models operating at the same temperatures [18, 38]. Most of the data used for the two models are based on these sources, so the current densities at the thermoneutral voltage are equal between the models and literature values. For both cells, the model exhibits a logarithmic-like development, undershooting voltage values at low and high current densities and slightly overshooting in between. In the area around the current density used in these models, the error between the two curves is assumed to be acceptable if it's below 5%. For the SOEC, the acceptable area of operation, in which the electrochemical model is considered to be verified, is then between a current density of around 0.5 A/cm^2 and 6.5 A/cm^2. For the P-SOEC, the acceptable area of operation is at a current density of around 0.165 A/cm^2 to 0.415 A/cm^2 and again at around 0.825 A/cm^2 to 1.8 A/cm^2.

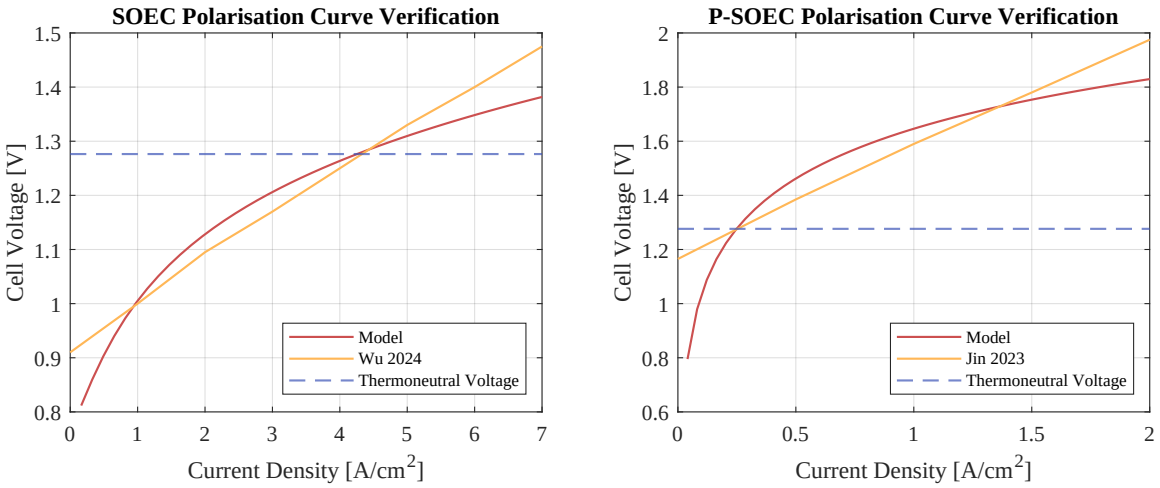

(a) SOEC polarisation curve at 800 °C.

(b) P-SOEC polarisation curve at 500 °C.

Figure 3.7: Polarisation curves of the electrolysis cell models of this study compared to polarisation curves in literature at similar operating conditions [18, 38].

The cause of the undershoots at the lower current densities can be due to activation overpotentials being too low in this area of operation in the models. At lower current densities, the activation necessary for charge transfer is usually higher, making this the most prominent overpotential in this area. At the higher current densities, the concentration overpotential, caused by the resistance to the transport of reactant and product species approaching and leaving the reaction site, respectively, is more prominent. This implies that the model underestimates this value at higher current densities. [15]

With the electrochemical SOEC models verified in the area of operation used in this report, the results of these models are presented in Table 3.5, highlighting the parameters used as input to the Aspen models. It is noticed that there's a big difference between the cell power of the SOEC and the P-SOEC. This is due to the SOEC being able to operate at a much higher current density (4.5 A/cm^2 vs 0.192 A/cm^2 for P-SOEC), and the cell surface area of the SOEC being 4 times larger. As the number of cells per stack is also a bit higher, the resulting number of stacks is around 70 times more for the P-SOEC than the SOEC. Since P-SOECs are not as developed as SOECs, it makes sense that P-SOEC stacks are not yet scaled for large-scale production.

Since the number of stacks is rounded off to the higher integer, the total power input to the models is slightly higher than 500 MW, with the SOEC at 501.43 MW and the P-SOEC at 500.02 MW. This results in the generation of hydrogen and oxygen being slightly different between the models as seen from Table 3.5. Moreover, since the electrolysis systems are built to generate similar amounts of hydrogen, the water input varies significantly between the models due to the difference in Faradaic efficiency, directly affecting the required water flow as seen from equation (3.12).

Table 3.5: Resulting stack performance and plant molar flows of the SOEC and P-SOEC systems.

		SOEC	P-SOEC	Aspen Input
Cell power, $\dot{W}_{cell}$	[kW]	2.339	0.025	-
Stack power, $\dot{W}_{stack}$	[kW]	3693	5.164	-
Number of stacks, N_{stacks}	[-]	136	9682	-
Resulting total power, $\dot{W}_{tot}$	[MW]	5.023	5.002	-
Total flow rates [kmol/h]				
H_2O required, $\dot{n}_{H_2O,req}$		7141	12,913	Stream 31: Total flow rate
H_2 recycle flow, $\dot{n}_{H_2,rec}$		793.5	-	Sep: H_2 flow
O_2 recycle flow, $\dot{n}_{O_2,rec}$		-	1435	Sep: O_2 flow
O_2 anode sweep flow, $\dot{n}_{O_2,sweep}$		864.1	-	FSplit: O_2 flow
H_2 generation, $\dot{n}_{H_2,gen}$		6913	6943	-
O_2 generation, $\dot{n}_{O_2,gen}$		3456	3472	-

Using the inlet flow rate of water and the recycle flow rates, found from the electrochemical models, as an input to the Aspen electrolysis models, the H_2 and O_2 generated flow rates are found to be the same, with a relative error below 0.005%. The Aspen flowsheets of the electrolysis subsystems are presented in Appendix C.1.

3.3.2 Kinetic Ammonia Synthesis Model

The HBR is modelled as an isothermal 1D PBR based on the setup presented in Asgharian et al. [42] for an HBR operating at 450 °C and 150 bar. In Aspen Plus, the HBR is modelled as an RPlug component defining the necessary parameters given by the following mathematical model. Ammonia synthesis follows the reaction seen in equation (3.14):

$$N_2 + 3\,H_3 \rightleftharpoons 2\,NH_3 \qquad \Delta H^{\circ}_{rxn} = -46\,\mathrm{kJ/mol_{NH_3}} \tag{3.14}$$

where ΔH°_{rxn} is the heat of reaction per mole of NH_3 at 298 K. The inlet nitrogen flow rate is calculated considering a stoichiometric H_2/N_2 ratio of 3:1 and the generated H_2 flow rate from the electrochemical SOEC model. The conversion fraction of the ammonia synthesis reaction depends on the reaction rate determined by the specific catalyst utilised in the reactor. In this model, a fixed bed of KM1 iron catalyst is utilised, since it is the industrial standard [28]. The rate kinetics are based on Kibria et al. [50], defining the rate of formation of ammonia by the Temkin kinetic model:

$$r_{NH_3} = k_r \left(K_a^2 a_{N_2} \left[\frac{(a_{N_2})^3}{(a_{NH_3})^2} \right]^{1/2} - \left[\frac{(a_{NH_3})^2}{(a_{H_2})^3} \right]^{1/2} \right) \tag{3.15}$$

where r_{NH_3} is the reaction rate, k_r is the kinetic constant of the reverse reaction, K_a is the equilibrium constant of the reaction, and a_i is the activity (of species $i = N_2, H_2, NH_3$). k_r is a function of temperature, determined using the Arrhenius equation seen in equation (3.16):

$$k_r(T) = 1.7698 \times 10^{15} \cdot \exp\left(\frac{-1705.61}{R_u \cdot T}\right) \tag{3.16}$$

K_a and a_i are determined from equation (3.17) and (3.18), respectively:

$$\log_{10} K_a = -2.69112 \cdot \log_{10} T - 5.519{,}27 \times 10^{-5} \cdot T + 1.848{,}86 \times 10^{-7} \cdot T^2 + \frac{2001.6}{T} + 2.6899 \tag{3.17}$$

$$a_i = x_i f_i^\circ \qquad\qquad f_i^\circ = \psi_i P \tag{3.18}$$

where x_i is the mole fraction, f_i° is the pure component fugacity at the temperature and pressure of the system, and ψ_i is the fugacity coefficient (of species $i = N_2, H_2, NH_3$). ψ_i are experimentally determined relations depending on the operating temperature and pressure of the system, and can be found in Kibria et al. [50]. Through the presented equations, the instantaneous reaction rate of ammonia is calculated as a function of the axial z-direction, temperature, and pressure over the reactor volume.

3.3.2.1 Reactor Sizing & Model Inputs

The size of the HBR in the HT and LT case is determined using equal gas-hourly space velocities (GHSVs) for each case, aiming for a value in the range of 10,000-15,000 h^{-1} [51, 52]. The GHSV depends on the volume flow rate at standard conditions ($\dot{V}_{std}^\circ$) and the catalyst volume ($\forbar{V}_{cat}$):

$$GHSV = \frac{\dot{V}_{in}^\circ}{\forbar{V}_{cat}} \tag{3.19}$$

Using a bed porosity of 0.4 and fixing the diameter of the reactor, the required reactor length and catalyst volume are determined for each case. The HT case is used as a starting point, iterating between values of reactor length, diameter, and catalyst volume within the allowed GHSV range. During this iteration, the pressure drop in the reactor is important to consider, as it is sensitive to the reactor sizing. The pressure drop is calculated in Aspen Plus using the Ergun equation. The volume and mass of the catalyst are found from the resulting HBR volumes using the following equation:

$$\forbar{V}_{cat} = \forbar{V}_{HBR} \cdot (1 - \phi_{bed}), \qquad\qquad m_{cat} = \forbar{V}_{cat} \cdot \rho_{cat} \tag{3.20}$$

An iteration between the calculated reactor length and catalyst mass of the HBR and the resulting volume flow rate of the gas mixture entering the HBR in the Aspen Plus model is then made to find the final GHSV of the two cases. The resulting design parameters for the HBR are summarised in Table 3.6 along with the operating conditions.

Table 3.6: Overview of the input parameters to the kinetic HBR model for both the HT and LT case.

		HT Case	LT Case	Sources
Inlet Conditions				
Inlet Temperature, T	[°C]	450		[42]
Inlet pressure, P	[bar]	150		[42]
Design Parameters				
Bed porosity, ϕ_{bed}	[-]	0.4		[42]
Catalyst particle diameter, D_p	[m]	2.3×10^{-3}		[50]
Catalyst particle density, ρ_{cat}	[kg/m^3]	3250		[50]
Reactor diameter, D_r	[m]	4.40		Modelled
GHSV	[h^{-1}]	11,051		Modelled
Reactor length, L_r	[m]	7.000	7.037	Modelled
Catalyst mass, m_{cat}	[kg]	207.553	208.637	Modelled

3.3.2.2 HBR Performance Results

The change in molar composition over the HBR length is seen in Figure 3.8a for the HT case (same result in LT case), while Figure 3.8b displays the change in molar flow rates over the HBR length for both the HT and LT cases. The overall conversion of nitrogen into ammonia, including recycling, reaches approximately 98.5% for both the HT and LT cases. The ammonia yield is almost the same in the two cases, with the HT case producing 78.74 ton_{NH_3}/h and the LT case producing 78.90 ton_{NH_3}/h. This minimal difference is attributed to the slight variation in hydrogen generation between the SOEC and P-SOEC systems, as well as the differences in reactor design.

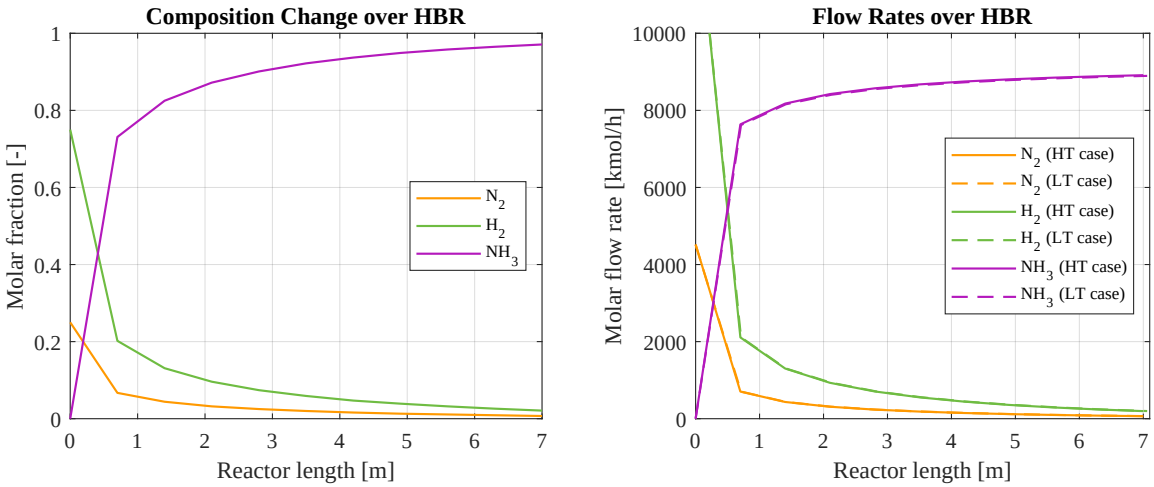

(a) Change in molar composition of HT case.

(b) Change in molar flow rate of HT and LT case.

Figure 3.8: Change in molar composition and molar flow rates over the length of the HBR. Only the reactants and products of the ammonia synthesis reaction are included, although there are traces of other components.

An overview of some of the key performance parameters for the HBR is summarised in Table 3.7, displaying that the HT and LT cases are almost identical. This is expected since the inputs to both systems

are the same, with only slight changes in the inlet flow rates, and as mentioned, since the reactor designs differ slightly to have identical GHSVs.

Table 3.7: Key performance parameters of the HBRs modelled in the HT and LT systems.

Parameter		**HT Case**	**LT Case**
NH_3 yield	[ton/day]	1890	1894
Conversion	[%]	98.55	98.54
Residence time	[s]	13.60	13.62
Pressure drop	[bar]	0.557	0.552
HBR waste heat	[MW]	67.18	67.50

This concludes the modelling approach related to the detailed mathematical models and performance results of the electrolysis cells and HBR. Following this, the economic analysis is presented in the next chapter, along with the results of the techno-economic study.

4 | Feasibility Study & Results

In this chapter, the results of the system models outlined in Chapter 3 are presented and evaluated. This comprises a presentation of the economic feasibility study and the final results of the techno-economic analysis, assessing the performance and feasibility of the presented cases.

4.1 Economic Feasibility Study

The economic feasibility of an SOEC-HB heat-integrated system is analysed by estimating the LCOA for the LT and HT cases with and without heat integration between the HBR and SOEC. The LCOA is calculated from the sum of costs over the plant lifetime, comprising the capital expenditures (CAPEX) and operational expenditures (OPEX), and the annual ammonia production capacity ($\chi_{\mathrm{NH_3},year}$) as follows:

$$LCOA = \left(\frac{CAPEX + OPEX}{\chi_{\mathrm{NH_3},year}} \right)_{lifetime} \tag{4.1}$$

The CAPEX is calculated using the APEA extension in Aspen Plus for the available components. This excludes the SOEC and P-SOEC stacks that are instead found in the available literature. Prosser et al. [53] estimate a CAPEX of around 130 mio USD for 500 MW SOEC stacks operated at 750 °C and 1.3 bar. It is more difficult to find an accurate source on the cost of P-SOECs, since they are less developed. Instead, a source on a proton-conducting fuel cell (PCFC) operated at 550 °C is found in Dubois [54] with an estimated specific CAPEX of 457 USD/kW, resulting in a CAPEX of 228.5 mio USD for 500 MW P-SOEC stacks. Typically, a plant lifetime of 20-25 years is considered, but the lifetime of a typical SOEC or P-SOEC stack is only around 5 years [53, 54]. It is expected that the lifetime of P-SOEC stacks will increase as this technology increases in TRL, since the thermal stress is lower on this cell. However, since the technology is still in early development, a lifetime of around 5 years is estimated by Dubois [54]. This must also be considered when evaluating the CAPEX, which can be found from equation (4.2):

$$CAPEX = C^{cap}_{HB\,loop} + C^{cap}_{CASU} + C^{cap}_{electrolysis} \tag{4.2}$$

where C^i_j is the cost of category i (here capital) for system j. Similarly, the yearly OPEX is found using the APEA application and can be found from the following summation:

$$OPEX_{year} = C^{op}_{HB\,loop} + C^{op}_{CASU} + C^{op}_{electrolysis} \tag{4.3}$$

This includes both the OPEX in terms of electricity costs, utility costs and operation and maintenance costs. The lifetime OPEX can then be found from equation (4.4):

$$OPEX_{lifetime} = \sum_{y=1}^{lifetime} \frac{OPEX_{year}}{(1+d)^{y-1}} \tag{4.4}$$

where y is the year and d is the discount rate. The values used in the feasibility study are summarised in Table 4.1. It is observed that the expected plant lifetime is set to 20 years, indicating that the stacks must be replaced three times during this period. The annual hours of operation are based on Asgharian et al. [42], assuming that the plant must be shut down for 6 weeks a year for maintenance. The discount rate is based on Palys et al. [28], while the cost of deionised water of 2.32 USD/m^3 is found in Zeitoun et al. [55]. The cost of electricity of 52 USD/MWh is based on the highest unit cost of onshore wind in the EU based on 2024 numbers from IRENA [56]. Since it is not accurate to assume a fixed cost of electricity, especially when looking 20 years into the future, a lower and upper margin for this value is added as a sensitivity test to the economic analysis. The lower value of 42 USD/MWh is based on 2024 values from [57] and the upper value of 88 USD/MWh is based on 2019 values from [58].

Table 4.1: Overview of parameters used for all cases in economic feasibility study.

Parameter	Value	Unit
Expected plant lifetime	20	years
Expected stack lifetime	5	years
Annual hours of operation	7758	hours
Discount rate, d	8.3	%
Cost of deionised water	2.32	USD/m^3
Cost of electricity		
Base value	52	USD/MWh
Lower value	42	USD/MWh
Upper value	88	USD/MWh

Based on the methodology presented in this section, the results of the economic feasibility study are presented next, along with the connection to the technical results.

4.2 Results of Techno-Economic Study

Based on the developed models and the methods of the economic feasibility study presented, the technical and economic feasibility results are presented in this section.

4.2.1 Electricity Consumption & Plant Efficiency

Since the HB loop and CASU subsystems are identical between the HT and LT cases, except for slight differences in flow rates, the electricity consumption of these subsystems is also almost identical as seen on Figure 4.1. The primary difference between the four cases lies in the electricity consumption of the electrolysis system, which is attributed to the electric heater used to achieve the operating temperature of the electrolysis cells. Most noticeable is the large electricity requirement of the electric heater in the P-SOEC-B case, reaching 141 MW. This is due to the lower heat duty of the internal HEX network in this system, meaning that the water has only just started to evaporate, and the remaining latent heat

required to evaporate the water is higher. Conversely, the electricity requirement of the electric heater in the SOEC-INT system is only 13.6 MW, as the internal HEX network, combined with the heat duty from the HBR in this system, is more than sufficient to evaporate the water.

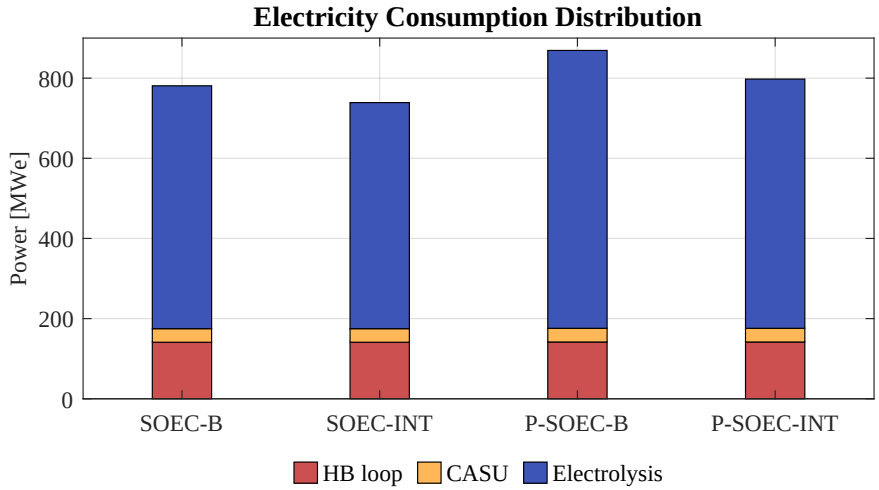

Figure 4.1: Electricity consumption of the four cases, divided between the three subsystems: Electrolysis, HB loop, and CASU.

The reduction in electricity consumption between the non-integrated and heat-integrated cases sums to 5.45% for the SOEC system and 8.24% for the P-SOEC system. Considering the heat duty required to bring the water input to the operating temperature of the cells, the waste heat from the HBR is able to cover 55.2% and 69.7% of this for the SOEC and P-SOEC systems, respectively.

The plant energy efficiency (η_{plant}) is closely related to the electricity consumption, and is calculated from equation (4.5), also including the calculation of the electrolysis electrical efficiency ($\eta_{el,electrolysis}$):

$$\eta_{plant} = \frac{\dot{n}_{NH_3} \cdot LHV_{NH_3}}{\dot{Q}_{in,tot} + \dot{W}_{in,tot}}, \qquad \eta_{el,electrolysis} = \frac{\dot{n}_{H_2} \cdot LHV_{H_2}}{\dot{W}_{in,electrolysis}} \tag{4.5}$$

where $\dot{Q}_{in}$ and $\dot{W}_{in}$ are the total external heat and power input, respectively. The resulting plant energy efficiency and electrolysis electrical efficiency for each case are presented in Figure 4.2, with the most efficient case being SOEC-INT.

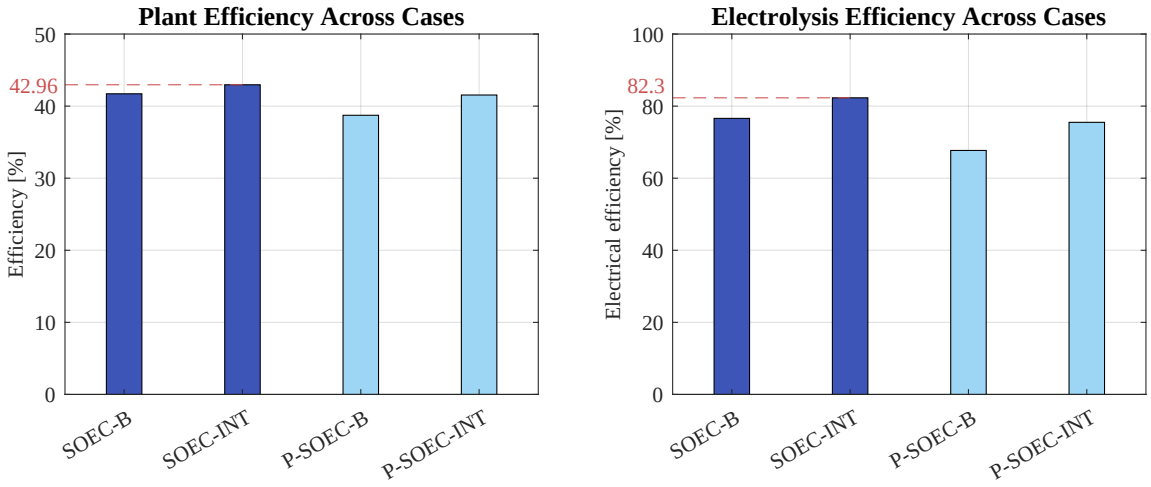

(a) Plant energy efficiency.

(b) Electrolysis electrical efficiency.

Figure 4.2: Plant and electrolysis efficiencies of the four cases found from equation (4.5).

The technical performance results of the four cases are summarised in Table 4.2.

Table 4.2: Technical performance results. *Of the heat duty required to bring water to the cell operating temperature.

	SOEC-B	**SOEC-INT**	**P-SOEC-B**	**P-SOEC-INT**
Electric heater electricity input [MW]	55.50	13.59	141.4	70.28
Total electricity consumption [MW]	783.2	741.3	866.9	795.4
Plant electricity consumption reduction [%]	-	5.35	-	8.24
HBR heat duty coverage* [%]	-	55.2	-	69.7
Efficiency [%]				
Plant energy efficiency, η_{plant}	41.71	42.96	38.73	41.54
Electrolysis electrical efficiency, $\eta_{el,electrolysis}$	76.58	82.30	67.66	75.46

The electrical efficiencies are valuable for comparison with similar systems; however, the economic results are also crucial for such a comparison. The results of the economic feasibility study are presented next, estimating the LCOA of the four cases.

4.2.2 Levelised Cost of Ammonia

The LCOA of the four cases depends on CAPEX, OPEX, and production capacity, as seen in equation (4.1). The CAPEX and OPEX are evaluated both in terms of yearly costs and lifetime costs as summarised in Table 4.3 together with the annual ammonia production and the resulting LCOA. As expected, considering the found electricity consumption and plant efficiencies, the LCOA is lowest for the SOEC-INT case and highest for the P-SOEC-B case.

Table 4.3: Results of the economic feasibility study $OPEX$ and $LCOA$ values are based on the base value of electricity costs.

	SOEC-B	SOEC-INT	P-SOEC-B	P-SOEC-INT
Yearly NH_3 Production [kton/year]	612.2	612.2	613.1	613.1
Yearly costs [mio. USD/year]				
Capital Expenditures, $CAPEX$	44.47	45.05	61.39	61.75
Operational Expenditures, $OPEX$	346.9	336.3	401.1	372.7
Costs after 20 years [mio. USD]				
Capital Expenditures, $CAPEX_{20}$	889.4	900.9	1228	1235
Operational Expenditures, $OPEX_{20}$	3608	3498	4175	3876
Levelised Cost of Ammonia, $LCOA$	367.3	359.3	440.6	416.8

It is evident that both the CAPEX and OPEX impact the difference in LCOA. Regarding the CAPEX, the cost of the P-SOEC cells is the largest contributor to the high cost of electrolysis for the P-SOEC cases, as seen in Figure 4.3. Since the lifetime of the plant is assumed to be 20 years and the lifetime of the stacks is only 5 years, it is accounted for that the stacks should be replaced 3 times during the plant lifetime.

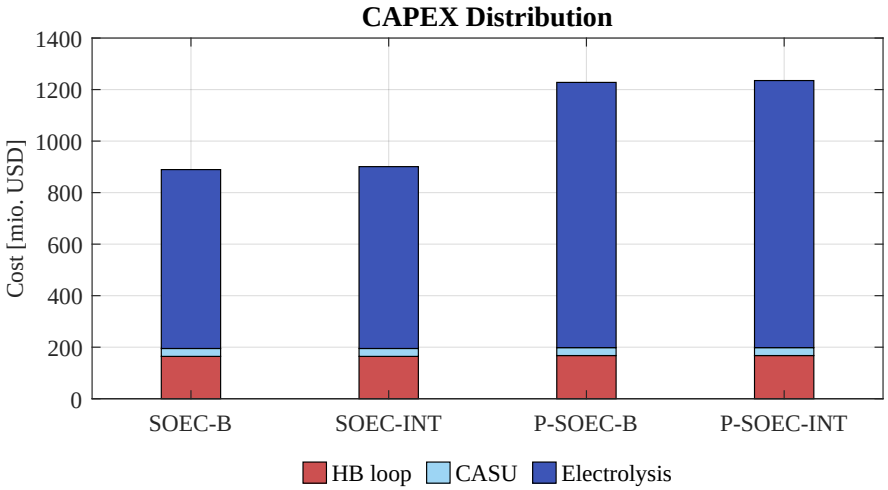

Figure 4.3: The distribution of CAPEX between the plant subsystems and the stacks, across the four cases. This is based on a lifetime of 20 years, meaning that the stack degradation is taken into account.

It is expected that the CAPEX of the HB loop and CASU will be almost the same across all four cases, as they are constructed in the same way, with only minor changes in flow rates. For the same reason, the OPEX distribution after 20 years of operation, seen in Figure 4.4, shows the same tendency for the HB loop and CASU. Here, it is seen that electrolysis is evidently the most significant contributor. This fits well with the high electricity consumption of the 500 MW stacks and electrolysis system presented in Figure 4.1.

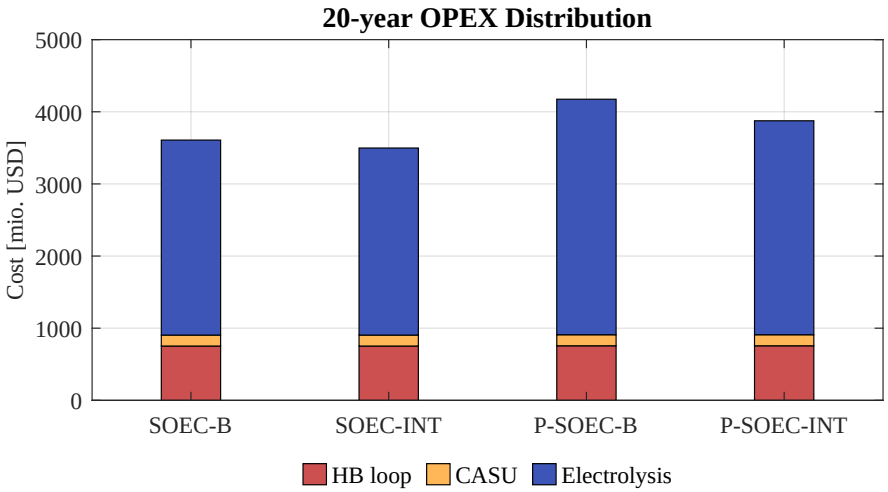

Figure 4.4: The distribution of OPEX between the plant subsystems, across the four cases for the base value cost of electricity found in Table 4.1.

The resulting LCOA after 20 years for all four cases based on the presented CAPEX, OPEX and ammonia production is illustrated on Figure 4.5. As mentioned, the constant cost of onshore wind-based electricity used in this analysis presents quite a rigid assumption. Therefore, the LCOA is calculated with an upper and lower bound value to test the sensitivity of this result. This is illustrated in the form of error bars on Figure 4.5, which are seen to alter the resulting LCOAs significantly. The upper values are all around 45-50% higher than the base LCOAs, while the lower values are around 12-14% lower.

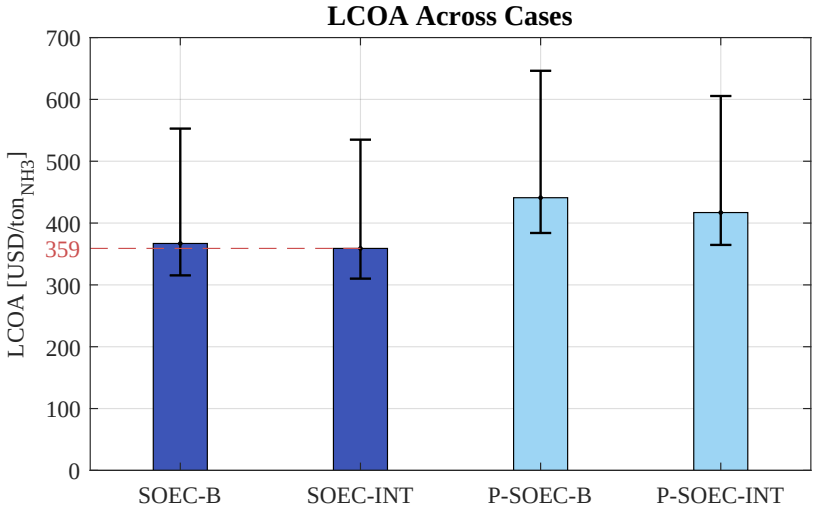

Figure 4.5: The resulting LCOA after 20 years across the four cases, with the error bars illustrating the effect of the cost of electricity used.

The development of the LCOA over the lifetime of the plant is seen in Figure 4.6 for all four cases. It is observed that the development follows an exponentially decreasing function, with sudden increases attributed to scheduled stack replacements. This development indicates that the price of ammonia is already halved after 4 years of production, while the reduction over the plant lifetime is around 70%.

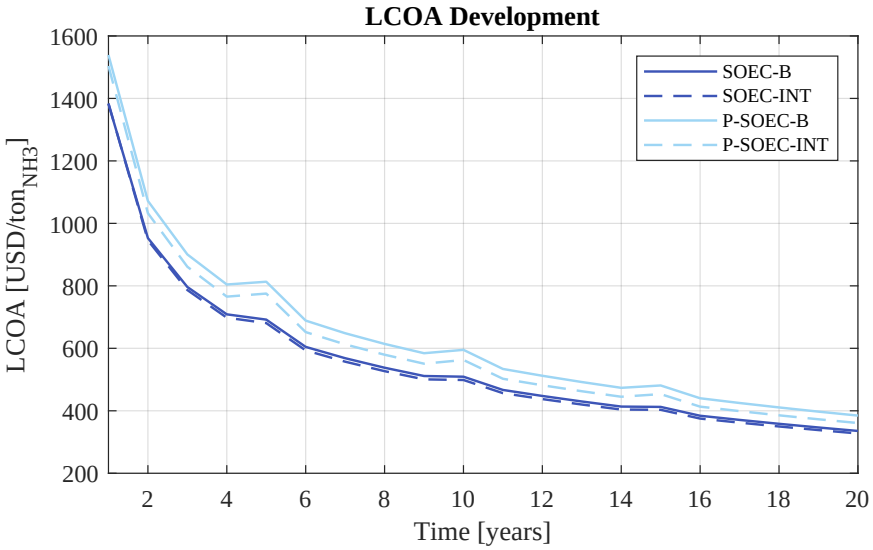

Figure 4.6: LCOA development over a plant lifetime of 20 years for the four cases.

The results of the techno-economic study indicate that the most feasible case, both technically and economically, is the SOEC-INT case, highlighting the potential for heat integration between an SOEC and HB process.

4.2.3 Comparison to Existing Ammonia Production & Literature

The results presented are relevant in comparison to similar ammonia production plants, considering both business-as-usual (BAU) SMR plants for grey ammonia production and other types of green ammonia plants based on an electricity input from renewable energy sources (RES). The LCOA for the SOEC-INT case, concluded to be the most energy- and cost-efficient case, is compared to different types of ammonia production plants in Figure 4.7. It is observed that the SOEC-INT case is not competitive with BAU SMR, as expected, but shows promise compared to blue ammonia production, where carbon capture and storage (CCS) is integrated into the SMR plant, considering the lower LCOA value. When compared to the RES-based ammonia production technologies (wind and solar), the SOEC-INT case shows great promise and competitiveness, even when considering the upper LCOA value.

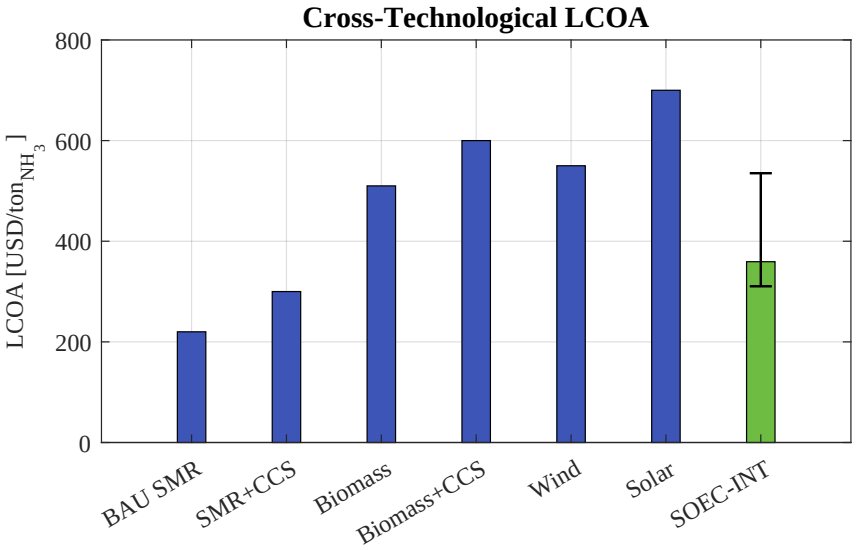

Figure 4.7: LCOA across different technologies for ammonia production from Schueler et al. [59], compared to the SOEC-INT case of this study.

The electrical efficiency of the SOEC-INT case is found to be 82.3% as seen in Figure 4.2b. In the literature study presented in Section 1.1, electrical efficiencies of other SOEC-integrated systems were given based on the studies conducted by Wang et al. [37] and Wu et al. [38]. A comparison between these values and the SOEC-INT case is presented in Figure 4.8, along with the electrical efficiency of a typical stand-alone SOEC-system (without waste heat integration) [10]. It is seen that the SOEC-INT case performs significantly better than the stand-alone case, as expected, but is just below the other two integrated cases. Although this difference is not significant, with electrical efficiencies of 85.2% in Wang et al. [37] and 89.6% in Wu et al. [38]. It is noted that neither of these sources accounts for the influence of the FE.

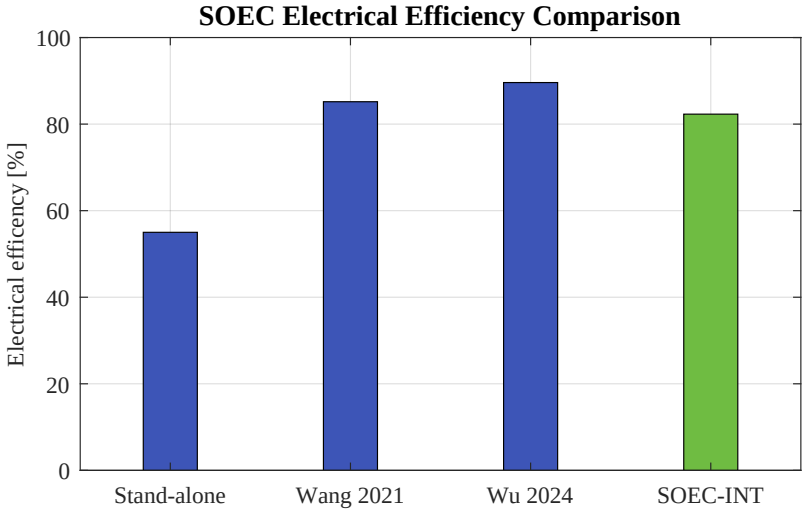

Figure 4.8: Electrical efficiency of electrolysis system of SOEC-INT case compared to literature values from [10, 37, 38].

With the results of the techno-economic analysis presented and compared to similar literature systems, a discussion of the analysis methods used and results obtained is presented in the preceding chapter.

5 | Discussion

In this chapter, the assumptions used and results obtained from modelling the SOEC-HB integrated systems are discussed. The primary focus is on the quality of the assumptions used for designing and modelling the electrolysis systems and the HB loop, along with the assumptions used for the economic analysis. Finally, the practical feasibility of using ammonia for maritime e-fuel applications is discussed.

5.1 Electrolysis Design & Model Assumptions

The design parameters used for the SOEC and P-SOEC stacks are based on multiple sources, which can introduce uncertainty in the validity of the FE values, as these are determined for specific material choices and operating conditions. Changing the cell dimensions does not affect the input to the Aspen model, as this only impacts the overpotentials used for verification and the number of stacks required for the 500 MW systems. However, the current density and FE values would need to change accordingly, as these are influenced by the material choices and dimensions. For the HT SOEC, the operating temperature, pressure and FE are based on Duan et al. [39]. The operating temperature and pressure coincide with the sources used for design and overpotential parameters [37, 38]. However, the FE is based on a H_2O/CO_2 co-electrolysis SOEC, as FE values were only found in the literature concerning this type of SOEC. This makes the relationship between cell voltage and current density quite different from that of a pure H_2O electrolysis cell. Thus, the current density at thermoneutral operation is based on Wu et al. [38] instead. Since literature often disregards the FE of SOECs, assuming a 100% efficiency, the used value of 96.8% is considered acceptable despite these uncertainties. The material used in all three sources [37–39] are YSZ-based, making the design compatible in terms of materials.

For the LT P-SOEC, all the operating conditions are based on Jin et al. [18] using BZY-based materials. However, most of the design and overpotential parameters are based on Ni et al. [48], who studied a PCFC operated at 1000 °C using a cerium-oxide-based electrolyte. This means that the found overpotentials contain uncertainties. The found polarisation curve, compared against the data from Jin et al. [18] in Figure 3.7b, does show significant undershoots at lower and higher current densities, which the parameter uncertainties of using data from Ni et al. [48] can explain.

The efficiencies used in this report are all defined and explained in Appendix A.1 to ensure transparency; however, this is not a standard practice in the literature working with electrolysis systems. Therefore, it is not always clear whether efficiency refers to energy input in general or electricity input only, is calculated on an LHV or HHV basis, or if the efficiency is determined at the cell or system level. This often leads to the misconception that SOEC systems can operate at high electrical efficiencies of nearly 100%. However, this usually refers to the cell efficiency, using an FE of 100% [10] and utilising freely available waste heat, enabling thermoneutral operation. The comparison to efficiencies found in literature, seen in Figure 4.7, is made considering only sources with well-defined efficiencies.

5.2 Ammonia Synthesis Operating Conditions

The inlet conditions used for the HBR are based on the system used in Asgharian et al. [42], operating at 450 °C and 150 bar and using a stoichiometric H_2/N_2 inlet composition of 3:1. These three parameters can all be optimised to favour the forward reaction of ammonia synthesis, increasing the ammonia yield according to the principle of Le Chatelier [60]. One approach to increasing the ammonia yield is to slightly increase the inlet H_2/N_2 ratio, allowing more of the H_2 to react with any remaining N_2 gas in the reactor. A second option is to increase the operating pressure of the HBR to enhance the ammonia yield, but this is less attractive considering the increased energy input and component costs [28]. One argument presented in the report is to examine the effect of heat integration on varying the electrolysis operating temperature while maintaining a lower HBR operating temperature to increase ammonia production. Therefore, a lower operating temperature of 400 °C makes more sense in this context, as it favours the forward reaction but reduces the percentage of the heat required to bring the water to the cell operating temperature that the HBR can cover.

Another reason to maintain a temperature of 450 °C in the HBR is the increased likelihood of corrosion at lower operating temperatures. In the H_2 stream entering the HB loop of the HT system, there is a small water content (0.192 mol%). At lower temperatures, this trace amount of water can lead to oxygen poisoning of the iron-based catalyst [61]. Therefore, if a lower operating temperature is considered, the water content must be reduced.

5.3 Validity of Economic Feasibility Analysis

The economic feasibility analysis relies heavily on cost estimations generated in Aspen Plus using the APEA extension. This leads to uncertainties in component choices and a limited operation range of the equipment used. As some of the system components in the HT SOEC system are subject to high temperatures of around 800 °C, the material choices must reflect this. However, APEA has very strict temperature limits on the materials of some components. Thus, the electric heater and separator of the HT SOEC system are modelled with an upper limit of 625 °C, which may affect the economic results slightly.

Moreover, since V12.1 of Aspen Plus does not include any electrolysis units, this equipment is found in literature. The assumptions regarding stack lifetime and replacement frequency have a substantial impact on the CAPEX. The assumed SOEC stack lifetime of 5 years (38,790 hours with 7758 hours/year of operation) align well with the 20,000-50,000 hours stack lifetime reported in [14]. However, the lifetime of the P-SOEC stacks is based on PCFC stacks from Dubois et al. [54], due to the limited availability of literature. The same applies to the P-SOEC stack CAPEX used. Since the PCFC is more developed than the P-SOEC, the lifetime may be shorter and CAPEX higher in reality, which could influence the final LCOA of the P-SOEC cases. However, since the SOEC-INT case has proven to be the most cost-effective, this does not affect the conclusions on this system.

5.4 The Choice of Ammonia for Maritime E-Fuel

Ammonia presents a promising candidate for maritime decarbonisation due to storage convenience, existing global infrastructure, and its carbon-free composition. However, its advantages must be weighed against challenges in engine development. Since ammonia requires a high combustion temperature and has a slow flame speed, dual-fuel engine configurations have been developed [62]. This can be a viable transitional solution, but the inherent reliance on auxiliary fuels questions the overall carbon neutrality of the approach. Dual-fuel engines do address the issue of NO_x and N_2S emissions associated with ammonia combustion [62]. Compared to e-methanol, ammonia faces slower adoption in engine technology, which may hinder the near-future deployment. Furthermore, the production scale required to meet global shipping demand is substantial, necessitating a rapid increase in electrolyser capacity. While the SOEC technology offers high efficiency, the current plant capacity and durability may make PEMEC or AEC solutions more practical in the short term.

The production capacity of the ammonia plant reaches approximately 1890 ton/day. In comparison, a container ship of 10,000 TEU travelling at normal speed (22 knots) consumes around 250 ton/day of heavy fuel oil [63], equivalent to approximately 518.5 ton_{NH_3}/day based on the LHVs. This means that the ammonia plant modelled in this report can deliver enough e-fuel for 3.65 container ships of this size, emphasising the scale-up required to decarbonise the maritime sector.

6 | Conclusion

This report investigated the technical and economic feasibility of an SOEC-HB heat-integrated green ammonia production plant for marine e-fuel applications. This was achieved through comparison of four cases, considering both HT SOECs operating at 800 °C and LT P-SOECs operating at 500 °C, with (-INT) and without (-B) heat integration with the HB loop. The findings show that the SOEC-INT configuration is the most energy- and cost-effective, achieving an overall plant efficiency of 42.96% and LCOA in the range of 310 - 535 USD/ton$_{NH_3}$, making it competitive with other types of green ammonia production.

The plant is modelled by developing process models in Aspen Plus for the three plant subsystems: The HB loop for ammonia synthesis, the electrolysis system for hydrogen production, and the CASU for nitrogen production. The electrolysis subsystems are coupled with a detailed mathematical model of the 500 MW electrochemical cells to estimate inlet and recycle streams for the SOEC and P-SOEC systems, as well as cell power requirements and the number of stacks, since Aspen Plus does not include built-in electrolysis components. Reaction kinetics and reactor sizing for ammonia synthesis are implemented directly in the Aspen RPlug component, yielding a production capacity of approximately 1890 ton/day across all cases.

To reduce energy consumption and increase overall energy efficiency in coupled HB-SOEC plants, heat integration proves to be a viable option. Operating the HBR at 450 °C and 150 bar produces 67.2 MW and 67.5 MW of waste heat, enabling it to cover 55.2% and 69.7% of the heat required to increase the water temperature to the operating temperature of the SOE and P-SOEC, respectively. This reduced electricity consumption by 5.35% and 8.24%, respectively, and increased electrolysis electrical efficiency from 76.6% to 82.3% in the HT system and from 67.7% to 75.5% in the LT system. While the relative efficiency gain of adding heat integration is greater for P-SOECs due to their lower operating temperature, the relatively low FE and high cost of stacks make them less cost-effective compared to the SOECs.

The economic analysis highlights that P-SOECs suffer from both high CAPEX and, in the P-SOEC-B case, elevated OPEX due to electric heating, resulting in an LCOA of 384 - 646 USD/ton$_{NH_3}$. Adding heat integration reduces this value to 364 - 605 USD/ton$_{NH_3}$, but it remains above the SOEC-B case of 316 - 553 USD/ton$_{NH_3}$. Ultimately, the SOEC-INT configuration with an LCOA of 310 - 535 USD/ton$_{NH_3}$ is concluded to be the most cost-effective solution among the four cases for large-scale e-ammonia production for the maritime sector, demonstrating competitiveness to similar green ammonia production pathways.

7 | Future Work

This chapter highlights relevant areas that require additional research and development, along with possible areas of optimisation, for future deployment of the SOEC-HB integrated ammonia plant.

7.1 Research & Development in P-SOECs

P-SOECs are still in the early stages of development, primarily in the research and development phase. This means that operation and material choices can still be optimised. Right now, significant challenges include low FEs and high stack costs. The lower FE is mainly due to the phenomenon known as electronic leakage, which refers to any unwanted current flowing outside of the desired current path [41]. This affects the efficiency with which electrons are transferred through the electrochemical cell. Duan et al. [41] explore recent advances in P-SOECs, where a research group achieved an FE of greater than 95% at 600 °C, focusing directly on reducing electronic leakage. This, combined with the fact that P-SOECs can produce completely dry hydrogen at the cathode, eliminating the need to separate any water content, highlights the potential of this technology. Still, a significant development gap remains before commercial deployment can be considered, requiring additional research in this field.

7.1.1 Faradaic Efficiency & Temperature Relation

In this work, it is mentioned that the operating temperature of the cell influences the FE. While this is true, material compositions also play a vital role. Both operating conditions and material choice influence the electronic leakage that directly affects the FE [41]. Therefore, it is challenging to establish a direct relationship between the FE and operating temperature of the cell, which is crucial for determining the performance of the cell and enabling the optimisation of operating conditions, especially for P-SOECs. Electronic leakage is not a significant concern in SOECs operating above 800 °C, but it is observed that the FE becomes more influential below this temperature [41]. Since P-SOECs and SOECs are constructed differently and utilise different materials, different relations for FE-Temperature dependence would be necessary between them. In general, such a relation would have to be described for a specific cell design to show high enough accuracy. This necessitates further experimental testing of different cell designs, as well as further development in the material composition of P-SOECs and SOECs operating below 800 °C.

7.2 Further Optimisation Possibilities

The optimisation of this work relates to the comparison between using HT and LT steam electrolysis, as well as the improvements achieved by utilising waste heat integration. Further optimisation can be achieved in the modelled subsystems by considering the optimisation parameters and their effect on capital and operational costs of the system. In future work, it is relevant to set up a cost function aiming to minimise the LCOA while adjusting the operation parameters.

7.2.1 SOEC & P-SOEC Parameters

In the literature study presented in Section 1.1, previous work on heat-integrated SOECs also focuses on optimising cell parameters such as operating voltage, current density, and temperature to analyse the effect on the electrical efficiency and power consumption of the system. This work considers thermoneutral operation with a fixed current density, limiting the operation range. Considering operation in exothermic and endothermic modes is also relevant to consider in a parameter optimisation study. The effect of varying the temperature, and perhaps pressure, is also interesting in terms of component choices to see if equipment costs can be minimised.

7.2.2 HB Loop Operating Conditions

It is discussed that changing the operating temperature, pressure and inlet feed ratio of the HBR directly affects the ammonia yield due to the principle of Le Chatelier. These parameters can be optimised on their own, but can also be directly related to equipment and operational costs, as seen in other work, such as Palys et al. [28]. Further relating this to the operation of the entire plant and the operating conditions of the electrochemical cells makes for an interesting optimisation problem in terms of costs and efficiency. However, such a wide optimisation problem can also lead to many uncertainties that must be monitored.

Bibliography

[1] Intergovernmental Panel on Climate Change (IPCC). "Summary for Policymakers". In: *Global Warming of 1.5C. An IPCC Special Report on the impacts of global warming of 1.5C above pre-industrial levels and related global greenhouse gas emission pathways, in the context of strengthening the global response to the threat of climate change, sustainable development, and efforts to eradicate poverty*. Geneva, Switzerland: World Meteorological Organization, 2018. URL: https://www.ipcc.ch/sr15/chapter/spm/.

[2] The European Council. *Climate change: what the EU is doing*. Accessed 17/04/2025. 2024. URL: https://www.consilium.europa.eu/en/policies/climate-change/.

[3] International Renewable Energy Agency (IRENA). *Decarbonising Hard-to-Abate Sectors with Renewables: Perspectives for the G7*. Tech. rep. Prepared at the request of the 2024 Italian G7 Presidency. Abu Dhabi, United Arab Emirates: IRENA, 2024. URL: https://www.irena.org/Publications/2024/Apr/Decarbonising-hard-to-abate-sectors-with-renewables-Perspectives-for-the-G7.

[4] Isabelle Gerretsen. "The Decarbonization Tradeoffs for Ammonia, Methanol and H2". In: *The Maritime Executive* (2022). Accessed 17/04/2025. URL: https://maritime-executive.com/editorials/the-decarbonization-tradeoffs-for-ammonia-methanol-and-h2.

[5] The Royal Society. *Ammonia: zero-carbon fertiliser, fuel and energy store*. Tech. rep. The Royal Society, 2020.

[6] A. Valera-Medina et al. "Review on Ammonia as a Potential Fuel: From Synthesis to Economics". In: *Energy & Fuels* 35.9 (2021), pp. 6964–7029. DOI: 10.1021/acs.energyfuels.0c03685.

[7] Rie Emilie Hansen. "Ammonia-Integrated Offshore Renewable Power Plant: A Small-Scale Absorbent-Enhanced Ammonia Synthesis Solution for Floating Power Plant A/S". MSc 3 Project. Aalborg University, 2025.

[8] A. Valera-Medina et al. "Ammonia for power". In: *Progress in Energy and Combustion Science* 69 (2018), pp. 63–102. ISSN: 0360-1285. DOI: https://doi.org/10.1016/j.pecs.2018.07.001. URL: https://www.sciencedirect.com/science/article/pii/S0360128517302320.

[9] Collin Smith, Alfred K. Hill, and Laura Torrente-Murciano. "Current and future role of HaberBosch ammonia in a carbon-free energy landscape". In: *Energy Environ. Sci.* 13 (2 2020), pp. 331–344. DOI: 10.1039/C9EE02873K. URL: http://dx.doi.org/10.1039/C9EE02873K.

[10] Mustafa Ergin Sahin. "An Overview of Different Water Electrolyzer Types for Hydrogen Production". In: *Energies* 17 (2024), p. 4944. DOI: https://doi.org/10.3390/en17194944.

[11] CIC energiGUNE. *Hydrogen production methods and its colours*. Accessed 16/04/2025. 2022. URL: https://cicenergigune.com/en/blog/hydrogen-production-methods-colours.

[12] Lena Maria Ringsgwandl et al. "Current Legislative Framework for Green Hydrogen Production by Electrolysis Plants in Germany". In: *Energies* 15 (2022), p. 1786. DOI: https://doi.org/10.3390/en15051786.

[13] Danish Energy Agency. *Technology Data - Renewable fuels*. Tech. rep. Danish Energy Agency, 2018.

[14] Gniewomir Flis and Ghassan Wakim. *Solid Oxide Electrolysis: A Technology Status Assessment*. Tech. rep. Clean Air Task Force, 2023.

[15] T. Smolinka. "Water Electrolysis". In: *Encyclopedia of Electrochemical Power Sources*. Ed. by Jürgen Garche et al. Elsevier, 2009, pp. 394–418. ISBN: 9780444527455. DOI: 10.1016/B978-044452745-5.00315-4.

[16] Topsoe A/S. *Topsoe A/S SOEC Fabrik Herning*. Accessed 23/04/2025. 2025. URL: https://www.topsoe.com/da/herning.

[17] Biaowu Lu et al. "Control strategy of solid oxide electrolysis cell operating temperature under real fluctuating renewable power". In: *Energy Conversion and Management* 299 (2024), p. 117852. ISSN: 0196-8904. DOI: https://doi.org/10.1016/j.enconman.2023.117852. URL: https://www.sciencedirect.com/science/article/pii/S0196890423011986.

[18] Xinfang Jin and Yasser Shoukry. "Current Leakage and Faradaic Efficiency Simulation of Proton-Conducting Solid Oxide Electrolysis Cells". In: *ECS Transactions* 111.6 (2023), pp. 1159–1167. DOI: 10.1149/11106.1159ecst. URL: https://doi.org/10.1149/11106.1159ecst.

[19] Libin Lei et al. "Intermediate-temperature solid oxide electrolysis cells with thin proton-conducting electrolyte and a robust air electrode". In: *J. Mater. Chem. A* 5 (44 2017), pp. 22945–22951. DOI: 10.1039/C7TA05841A. URL: http://dx.doi.org/10.1039/C7TA05841A.

[20] Sunfire. *Sunfire HyLink SOEC*. Accessed 24/04/2025. 2025. URL: https://sunfire.de/en/products/sunfire-hylink-soec/.

[21] Multiplhy Project. *Multiplhy Project*. Accessed 24/04/2025. 2025. URL: https://multiplhy-project.eu/.

[22] Topsoe. *SOEC - Solid Oxide Electrolysis Cells*. Accessed 24/04/2025. 2025. URL: https://www.topsoe.com/soec.

[23] Dynelectro. *1 MW SOE Collaboration*. Accessed 24/04/2025. 2025. URL: https://dynelectro.dk/news/1mw-soe-collaboration?utm_source=chatgpt.com.

[24] Elcogen. *Elcogen and Partners Unveil Syrius Project Aimed at Decarbonizing the Steel Industry*. Accessed 24/04/2025. 2025. URL: https://elcogen.com/elcogen-and-partners-unveil-syrius-project-aimed-at-decarbonizing-the-steel-industry/?utm_source=chatgpt.com.

[25] Mitsubishi Heavy Industries. *Hydrogen and Ammonia Solutions Development Base*. Accessed 24/04/2025. 2025. URL: https://www.mhi.com/business/solutions/hydrogen-ammonia/development-base.html?utm_source=chatgpt.com.

[26] Mitsubishi Heavy Industries. *MHI Begins Operation of SOEC Test Module at Takasago Hydrogen Park*. Accessed 24/04/2025. 2025. URL: https://www.globalhydrogenreview.com/hydrogen/31052024/mhi-begins-operation-of-soec-test-module-at-takasago-hydrogen-park/?utm_source=chatgpt.com.

[27] Hannes Lange et al. "Modularization approach for large-scale electrolysis systems: a review". In: *Sustainable Energy & Fuels* 8 (2024), pp. 1208–1224. DOI: 10.1039/D3SE01588B. URL: https://doi.org/10.1039/D3SE01588B.

[28] Matthew J. Palys et al. "Modeling and Optimal Design of Absorbent Enhanced Ammonia Synthesis". In: *Processes* 6.7 (2018). ISSN: 2227-9717. DOI: 10.3390/pr6070091. URL: https://www.mdpi.com/2227-9717/6/7/91.

[29] Ghassan Chehade and Ibrahim Dincer. "Progress in green ammonia production as potential carbon-free fuel". In: *Fuel* 299 (2021), p. 120845. ISSN: 0016-2361. DOI: https://doi.org/10.1016/j.fuel.2021.120845. URL: https://www.sciencedirect.com/science/article/pii/S0016236121007225.

[30] Tianbao Gu et al. "Exploring decentralized ammonia synthesis for hydrogen storage and transport: A comprehensive CFD investigation with experimental validation and parametric study". In: *Energy Conversion and Management* 295 (2023), p. 117604. ISSN: 0196-8904. DOI: https://doi.org/10.1016/j.enconman.2023.117604. URL: https://www.sciencedirect.com/science/article/pii/S0196890423009500.

[31] ALFA LAVAL et al. *Ammonfuel An Industrial View of Ammonia as a Marine Fuel*. Tech. rep. Version 09.9. Ammonfuel Working Group, 2020.

[32] International Energy Agency (IEA). *Electrolysers*. Tech. rep. Last updated 10 July 2023. International Energy Agency, 2023. URL: https://www.iea.org/energy-system/low-emission-fuels/electrolysers.

[33] Institute for Sustainable Process Technology (ISPT). *A one-gigawatt green hydrogen plant: Advanced design and costs*. Tech. rep. Institute for Sustainable Process Technology, 2022. URL: https://ispt.eu/publications/a-one-gigawatt-green-hydrogen-plant/.

[34] *Solid Oxide Electrolysis Cell (SOEC) Market Size, Share, Growth, and Industry Analysis, By Type, By Application, Regional Insights and Forecast to 2033*. Report ID 112615; Last Updated: 28 July 2025. 2025. URL: https://www.marketgrowthreports.com/market-reports/solid-oxide-electrolysis-cell-soec-market-112615.

[35] Giovanni Cinti et al. "Coupling Solid Oxide Electrolyser (SOE) and ammonia production plant". In: *Applied Energy* 192 (2017), pp. 466–476. ISSN: 0306-2619. DOI: https://doi.org/10.1016/j.apenergy.2016.09.026. URL: https://www.sciencedirect.com/science/article/pii/S0306261916313289.

[36] D. Frattini et al. "A system approach in energy evaluation of different renewable energies sources integration in ammonia production plants". In: *Renewable Energy* 99 (2016), pp. 472–482. ISSN: 0960-1481. DOI: https://doi.org/10.1016/j.renene.2016.07.040. URL: https://www.sciencedirect.com/science/article/pii/S096014811630636X.

[37] Fu Wang et al. "Thermodynamic analysis of solid oxide electrolyzer integration with engine waste heat recovery for hydrogen production". In: *Case Studies in Thermal Engineering* 27 (2021), p. 101240. ISSN: 2214-157X. DOI: https://doi.org/10.1016/j.csite.2021.101240. URL: https://www.sciencedirect.com/science/article/pii/S2214157X21004032.

[38] Chenxi Wu et al. "Thermodynamic analysis of a solid oxide electrolysis cell system in thermoneutral mode integrated with industrial waste heat for hydrogen production". In: *Energy* 301 (2024), p. 131678. ISSN: 0360-5442. DOI: https://doi.org/10.1016/j.energy.2024.131678. URL: https://www.sciencedirect.com/science/article/pii/S0360544224014518.

[39] Nanqi Duan et al. "Exploring Ni(Mn1/3Cr2/3)2O4 spinel-based electrodes for solid oxide cells". In: *J. Mater. Chem. A* 8 (7 2020), pp. 3988–3998. DOI: 10.1039/C9TA11878K. URL: http://dx.doi.org/10.1039/C9TA11878K.

[40] Yunfeng Tian et al. "Progress and potential for symmetrical solid oxide electrolysis cells". In: *Matter* 5.2 (2022), pp. 482–514. ISSN: 2590-2385. DOI: https://doi.org/10.1016/j.matt.2021.11.013. URL: https://www.sciencedirect.com/science/article/pii/S2590238521005750.

[41] Chuancheng Duan et al. "Proton-conducting oxides for energy conversion and storage". In: *Applied Physics Reviews* 7.1 (Mar. 2020), p. 011314. ISSN: 1931-9401. DOI: 10.1063/1.5135319. eprint: https://pubs.aip.org/aip/apr/article-pdf/doi/10.1063/1.5135319/19739717/011314_1_online.pdf. URL: https://doi.org/10.1063/1.5135319.

[42] Hossein Asgharian et al. "Techno-economic analysis of blue ammonia synthesis using cryogenic CO2 capture Process-A Danish case investigation". In: *International Journal of Hydrogen Energy* 69 (2024), pp. 608–618. DOI: https://doi.org/10.1016/j.ijhydene.2024.05.060.

[43] AspenTech. *Aspen Energy Analyzer V7.3 Reference Guide*. Tech. rep. Last updated: 03 November 2020. AspenTech, Nov. 2020.

[44] Duncan A. Nowicki, Gerry D. Agnew, and John T.S. Irvine. "Green ammonia production via the integration of a solid oxide electrolyser and a Haber-Bosch loop with a series of solid electrolyte oxygen pumps". In: *Energy Conversion and Management* 280 (2023), p. 116816. DOI: 10.1016/j.enconman.2023.116816. URL: https://doi.org/10.1016/j.enconman.2023.116816.

[45] Fiammetta Rita Bianchi and Barbara Bosio. "Modelling of green ammonia production based on solid oxide cells as electrolyser and oxygen separator for Haber-Bosch loop decarbonisation". In: *International Journal of Hydrogen Energy* 95 (2024), pp. 1183–1193. DOI: 10.1016/j.ijhydene.2024.07.047. URL: https://doi.org/10.1016/j.ijhydene.2024.07.047.

[46] L. Barelli, Gianni Bidini, and Giovanni Cinti. "Airflow Management in Solid Oxide Electrolyzer (SOE) Operation: Performance Analysis". In: *ChemEngineering* 1 (Nov. 2017), p. 13. DOI: 10.3390/chemengineering1020013.

[47] Meng Ni, Michael K. H. Leung, and Dennis Y. C. Leung. "An Electrochemical Model of a Solid Oxide Steam Electrolyzer for Hydrogen Production". In: *Chemical Engineering & Technology* 29 (May 2006), pp. 636 –642. DOI: 10.1002/ceat.200500378. URL: https://www.researchgate.net/publication/229666144.

[48] Meng Ni, Michael K. H. Leung, and Dennis Y. C. Leung. "Theoretical analysis of reversible solid oxide fuel cell based on proton-conducting electrolyte". In: *Journal of Power Sources* 177 (2008), pp. 369 –375. DOI: 10.1016/j.jpowsour.2007.11.057. URL: https://www.sciencedirect.com/science/article/pii/S0378775307025682?via%3Dihub.

[49] Yudong Wang, Barbara Marchetti, and Xiao-Dong Zhou. "Theoretical understanding of stability of the oxygen electrode in a proton-conductor based solid oxide electrolysis cell". In: *International Journal of Hydrogen Energy* 48.81 (2023), pp. 31519–31530. ISSN: 0360-3199. DOI: https://doi.org/10.1016/j.ijhydene.2023.04.148. URL: https://www.sciencedirect.com/science/article/pii/S0360319923019080.

[50] M.A. Kibria, D.E. McManus, and S. Bhattacharya. "Options for net zero emissions hydrogen from Victorian lignite. Part 2: Ammonia production". In: *International Journal of Hydrogen Energy* 48.95 (2023), pp. 37166–37182. ISSN: 0360-3199. DOI: https://doi.org/10.1016/j.ijhydene.2023.06.098. URL: https://www.sciencedirect.com/science/article/pii/S0360319923029579.

[51] CSIRO) Sarb Giddey (moderator and Ammonia Energy Association Organizers. *Introduction to Next-generation Ammonia Synthesis Panel*. Ammonia Energy Conference 2020, Panel #5: Next-generation Ammonia Synthesis. Presented on November 18, 2020. Available via Ammonia Energy Association archive. Nov. 2020.

[52] Max Appl. "The Haber-Bosch Heritage: The Ammonia Production Technology". In: *Proceedings of the 50th Anniversary IFA Technical Conference*. Presented September 2526, 1997. Conference organized by the International Fertilizer Association (IFA). Seville, Spain, Sept. 1997.

[53] Jacob H. Prosser et al. "Cost analysis of alternative large-scale high-temperature solid oxide electrolysis hydrogen production facilities". In: *International Journal of Hydrogen Energy* 106 (2025), pp. 1385–1402. ISSN: 0360-3199. DOI: https://doi.org/10.1016/j.ijhydene.2025.01.433. URL: https://www.sciencedirect.com/science/article/pii/S036031992500477X.

[54] A. Dubois. "Protonic ceramic fuel cells: Design analysis from cells to systems". In: *ProQuest Dissertations & Theses Global* (2019). URL: https://www.proquest.com/dissertations-theses/protonic-ceramic-fuel-cells-design-analysis/docview/2189860598/se-2.

[55] Obida Zeitoun et al. "Desalinated Water Costs from Steam, Combined, and Nuclear Cogeneration Plants Using Power and Heat Allocation Methods". In: *Energies* 16.6 (2023). ISSN: 1996-1073. DOI: 10.3390/en16062752. URL: https://www.mdpi.com/1996-1073/16/6/2752.

[56] International Renewable Energy Agency (IRENA). *Renewable Power Generation Costs in 2024*. Abu Dhabi: International Renewable Energy Agency, 2025.

[57] Tyler Stehly, Patrick Duffy, and Daniel Mulas Hernando. *Cost of Wind Energy Review: 2024 Edition*. Tech. rep. Accessed 20/08/25. National Renewable Energy Laboratory, 2024. URL: https://docs.nrel.gov/docs/fy25osti/91775.pdf.

[58] WindEurope. *Economics*. Accessed 20/08/25. 2019. URL: https://windeurope.org/policy/topics/economics/.

[59] Yannik Schueler et al. "How are decarbonization policies in the US and Canada shaping low-carbon ammonia production strategies?" In: *Environmental Research Letters* 19 (Oct. 2024). DOI: 10.1088/1748-9326/ad858c.

[60] LibreTexts. *Le Chatelier's Principle*. Accessed 20/08/25. URL: https://chem.libretexts.org/Bookshelves/Physical_and_Theoretical_Chemistry_Textbook_Maps/Supplemental_Modules_(Physical_and_Theoretical_Chemistry)/Equilibria/Le_Chateliers_Principle.

[61] Brian A. Rohr, Aayush R. Singh, and Jens K. Nørskov. "A theoretical explanation of the effect of oxygen poisoning on industrial Haber-Bosch catalysts". English. In: *Journal of Catalysis* 372 (2019), pp. 33–38. ISSN: 0021-9517. DOI: 10.1016/j.jcat.2019.01.042.

[62] Yanjie Ma et al. "Combustion and emission characteristics of ammonia-diesel marine high pressure direct injection low-speed dual-fuel engine". In: *Scientific Reports* 15 (2025), p. 20018. DOI: 10.1038/s41598-025-04997-z. URL: https://doi.org/10.1038/s41598-025-04997-z.

[63] Jean-Paul Rodrigue. *Fuel Consumption by Containership Size and Speed*. The Geography of Transport Systems (6th ed.) Accessed 26/08/25. 2024. URL: https://transportgeography.org/contents/chapter4/transportation-and-energy/fuel-consumption-containerships/.

[64] European Commission. *Technology readiness levels (TRL)*. Extract from Part 19 - Commission Decision C(2014)4995.

A | Appendix: Definitions

A.1 Efficiency Definitions

A1. Electrical efficiency - ratio of the energy content of product produced per unit time to electricity input to system. Used primarily to estimate the electrical efficiency of electrolysis systems, taking the energy content of the produced hydrogen. This report uses the LHV-based efficiency. [15]

$$\eta_{el} = \frac{\dot{n}_{\mathrm{H_2},gen} \cdot LHV}{\dot{W}_{in}} \qquad \text{or} \qquad \eta_{el} = \frac{\dot{n}_{\mathrm{H_2},gen} \cdot HHV}{\dot{W}_{in}}$$

A2. Energy efficiency - ratio of the energy content of product produced per unit time to energy input to system. Used in this report to estimate the plant energy efficiency, taking the energy content of the produced ammonia. This report uses the LHV-based efficiency.

$$\eta_{en} = \frac{\dot{n}_{\mathrm{NH_3}} \cdot LHV}{\dot{Q}_{in} + \dot{W}_{in}} \qquad \text{or} \qquad \eta_{en} = \frac{\dot{n}_{\mathrm{NH_3}} \cdot HHV}{\dot{Q}_{in} + \dot{W}_{in}}$$

A3. Voltage efficiency - defined as the ratio of the minimum theoretical cell voltage to the real voltage during operation of the cell. [15]

$$\eta_{vol} = \frac{E_{tn}}{E_{cell}} = \frac{\Delta H_{rxn}}{2 \cdot F \cdot E_{cell}}$$

A4. Faradaic efficiency - describes the overall selectivity of an electrochemical process. It can be defined as the efficiency with which charge (electrons) is transferred in a system facilitating an electrochemical reaction. In simpler terms, it can be described by the ratio of the actual hydrogen generation to the ideal hydrogen generation. [15]

$$\eta_{FE} = \frac{\dot{n}_{\mathrm{H_2},gen,real}}{\dot{n}_{\mathrm{H_2},gen,ideal}}$$

A5. Cell efficiency - the product of the voltage and Faradaic efficiency. [15]

$$\eta_{cell} = \eta_{vol} \cdot \eta_{FE}$$

A.2 Technology Readiness Level Definition

Technology Readiness Level (TRL) as defined by [64]:

- **TRL 1** - basic principles observed
- **TRL 2** - technology concept formulated
- **TRL 3** - experimental proof of concept
- **TRL 4** - technology validated in lab
- **TRL 5** - technology validated in relevant environment (industrially relevant environment in the case of key enabling technologies)
- **TRL 6** - technology demonstrated in relevant environment (industrially relevant environment in the case of key enabling technologies)
- **TRL 7** - system prototype demonstration in operational environment
- **TRL 8** - system complete and qualified
- **TRL 9** - actual system proven in operational environment (competitive manufacturing in the case of key enabling technologies; or in space

A.3 Energy & Temperature Relation for The Decomposition of Water

The change in Gibbs free energy, or the free energy of reaction, can be regarded as the minimum amount of enthalpy of reaction (ΔH_{rxn}) that must be applied as electrical energy. In water electrolysis, the energy required to decompose one mole of water into hydrogen and oxygen corresponds to the enthalpy of formation of one mole of water. A part of this enthalpy of reaction can be applied as thermal energy, according to the second law of thermodynamics, with a maximum equal to the product of the temperature (T) and entropy of reaction (ΔS_{rxn}). [15] The difference between the entropy term and the enthalpy of reaction is defined as the free energy of reaction:

$$\Delta G_{rxn} = \Delta H_{rxn} - T \cdot \Delta S_{rxn}$$

The relationship of the enthalpy of reaction and free energy of reaction with temperature (at atmospheric conditions) is seen in Figure A.1, demonstrating why higher temperatures are desirable in water electrolysis, from a thermodynamic point of view. The enthalpy of reaction drops suddenly when water undergoes the phase change from liquid to gaseous (reduced by the value of the enthalpy of evaporation), and then slightly increases with temperature. Suppose only the enthalpy of formation is considered. In that case, it is not advantageous to increase the temperature much above the 100 °C, but if the free energy of reaction is also considered, this is significantly more advantageous. At higher temperatures, the free energy of

reaction is significantly reduced, thereby decreasing the minimum amount of electrical energy required for electrolysis, given that it can be replaced by thermal energy. [15]

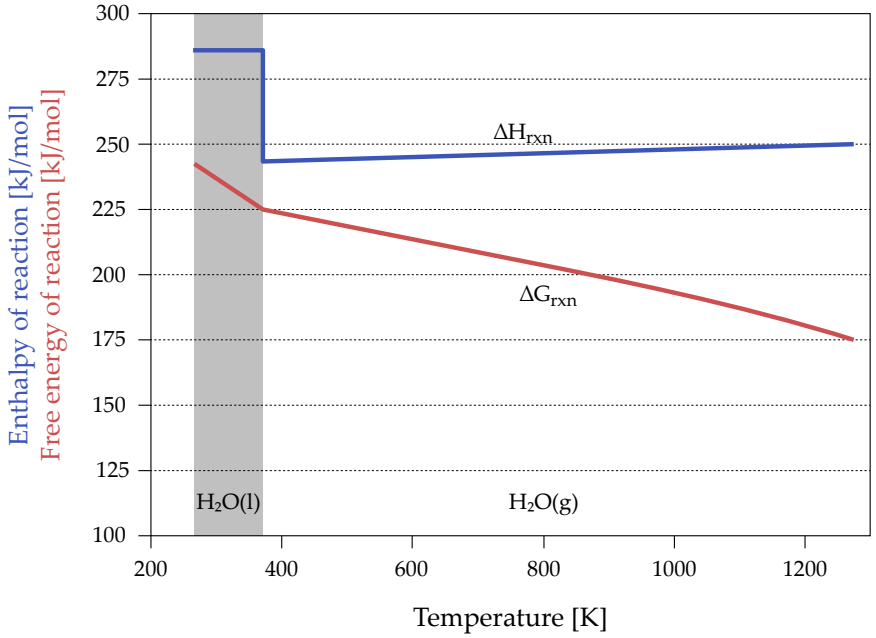

Figure A.1: Enthalpy of reaction (ΔH_{rxn}) and free energy of reaction (ΔG_{rxn}) as a function of temperature for the decomposition of water in both the liquid and gaseous phase at atmospheric pressure. Figure inspired by [15].

B | Appendix: Extended SOEC Model

B.1 Diffusion Calculations for Concentration Overpotentials

SOEC:

The following theory is based on the models presented by Wang et al. [37] and Nowicki et al. [44]. The partial pressures of the triple phase boundary ($p_{i,tpb}$) are found from equation (B.3):

$$p_{\mathrm{H_2},tpb} = p_{\mathrm{H_2},bp} - \frac{R_u \cdot T}{2 \cdot F} \frac{I \cdot \delta_C}{\mathcal{D}_{eff,\mathrm{H_2}}} \tag{B.1}$$

$$p_{\mathrm{O_2},tpb} = p_{\mathrm{O_2},bp} + \frac{R_u \cdot T}{4 \cdot F} \frac{I \cdot \delta_A}{\mathcal{D}_{eff,\mathrm{O_2}}} \tag{B.2}$$

$$p_{\mathrm{H_2O},tpb} = p_{\mathrm{H_2O},bp} - \frac{R_u \cdot T}{2 \cdot F} \frac{I \cdot \delta_C}{\mathcal{D}_{eff,\mathrm{H_2O}}} \tag{B.3}$$

where $p_{i,bp}$ is the bulk phase partial pressure (of species $i = \mathrm{H_2}$, $\mathrm{O_2}$, $\mathrm{H_2O}$), R_u is the universal gas constant, T is the operating temperature, F is the Faradaic constant, I is the current density, δ_i is the layer thickness of the anode and cathode, and $\mathcal{D}_{eff,i}$ is the effective diffusion coefficient (of species $i = \mathrm{H_2}$, $\mathrm{O_2}$, $\mathrm{H_2O}$). The effective diffusion coefficient can be calculated by:

$$\mathcal{D}_{eff,\mathrm{H_2}} = \frac{\varepsilon}{\tau \cdot (1/\mathcal{D}_{Kn,\mathrm{H_2}} + 1/\mathcal{D}_{\mathrm{H_2-H_2O}})} \tag{B.4}$$

$$\mathcal{D}_{eff,\mathrm{O_2}} = \frac{\varepsilon}{\tau} \cdot \mathcal{D}_{Kn,\mathrm{O_2}} \tag{B.5}$$

$$\mathcal{D}_{eff,\mathrm{H_2O}} = \frac{\varepsilon}{\tau \cdot (1/\mathcal{D}_{Kn,\mathrm{H_2O}} + 1/\mathcal{D}_{\mathrm{H_2O-H_2}})} \tag{B.6}$$

where τ is the tortuosity, ε is the porosity, and $\mathcal{D}_{Kn,i}$ and $\mathcal{D}_{i-j}$ are the Knudsen and binary diffusion terms, respectively. The Knudsen diffusion term describes the diffusion of species i in porous media, whereas the binary diffusion term describes the diffusivity of two species within each other. They are empirical relations computed by:

$$\mathcal{D}_{Kn,\mathrm{H_2}} = \frac{d_p}{3}\sqrt{\frac{8 \cdot R_u \cdot T}{\pi \cdot MW_{\mathrm{H_2}}}} \qquad \mathcal{D}_{Kn,\mathrm{O_2}} = \frac{d_p}{3}\sqrt{\frac{8 \cdot R_u \cdot T}{\pi \cdot MW_{\mathrm{O_2}}}} \qquad \mathcal{D}_{Kn,\mathrm{H_2O}} = \frac{d_p}{3}\sqrt{\frac{8 \cdot R_u \cdot T}{\pi \cdot MW_{\mathrm{H_2O}}}} \tag{B.7}$$

$$\mathcal{D}_{H_2-H_2O} = \frac{1.43 \times 10^{-2} \cdot T^{1.75}}{P\sqrt{2/(1/MW_{H_2} + 1/MW_{H_2O})}\left(\forbar{V}_{d,H_2}^{1/3} + \forbar{V}_{d,H_2O}^{1/3}\right)^2} \tag{B.8}$$

$$\mathcal{D}_{H_2O-H_2} = \mathcal{D}_{H_2-H_2O} \tag{B.9}$$

where d_p is the the pore diameter, MW_i is the molecular weight of species i, and $\forbar{V}_d$ are the diffusion volumes of the species.

P-SOEC:

The partial pressures at the triple phase boundary are found from equation (B.12):

$$p_{H_2,tpb} = p_{H_2,bp} + \frac{R_u \cdot T}{2 \cdot F}\frac{I \cdot \delta_C}{\mathcal{D}_{eff,H_2}} \tag{B.10}$$

$$p_{O_2,tpb} = p_{O_2,bp} - \frac{R_u \cdot T}{4 \cdot F}\frac{I \cdot \delta_A}{\mathcal{D}_{eff,O_2}} \tag{B.11}$$

$$p_{H_2O,tpb} = p_{H_2O,bp} - \frac{R_u \cdot T}{2 \cdot F}\frac{I \cdot \delta_A}{\mathcal{D}_{eff,H_2O}} \tag{B.12}$$

The effective diffusion coefficient can be calculated by:

$$\mathcal{D}_{eff,H_2} = \frac{\varepsilon}{\tau} \cdot \mathcal{D}_{Kn,H_2} \tag{B.13}$$

$$\mathcal{D}_{eff,O_2} = \frac{\varepsilon}{\tau \cdot (1/\mathcal{D}_{Kn,O_2} + 1/\mathcal{D}_{O_2-H_2O})} \tag{B.14}$$

$$\mathcal{D}_{eff,H_2O} = \frac{\varepsilon}{\tau \cdot (1/\mathcal{D}_{Kn,H_2O} + 1/\mathcal{D}_{H_2O-O_2})} \tag{B.15}$$

The Knudsen diffusion terms are the same as for the SOEC seen in B.7, and the binary diffusion terms are computed by:

$$\mathcal{D}_{H_2O-O_2} = \frac{1.43 \times 10^{-2} \cdot T^{1.75}}{P\sqrt{2/(1/MW_{H_2O} + 1/MW_{O_2})}\left(\forbar{V}_{d,H_2O}^{1/3} + \forbar{V}_{d,O_2}^{1/3}\right)^2} \tag{B.16}$$

$$\mathcal{D}_{O_2-H_2O} = \mathcal{D}_{H_2O-O_2} \tag{B.17}$$

The additional design parameters used in the presented equations are given in Table B.1.

Table B.1: Overview of the additional design input parameters to the electrochemical electrolysis model for the HT and LT case.

		SOEC	P-SOEC	Sources
Design Parameters				
Cathode layer thickness, δ_C	[µm]	12.5	500	[37, 47]
Anode layer thickness, δ_A	[µm]	17.5	50	[37, 47]
Pore radius, r_p	[µm]	1.385	0.5	[37, 47]
Porosity, ε	[-]	0.3	0.4	[37, 47]
Tortuosity, τ	[m]	5.0	5.0	[37, 48]

B.2 Mole Balances for SOEC & P-SOEC Systems

SOEC:

The generated and required mole flows have been determined, from which the rest of the mole flows can be determined from a simple mass balance. For the SOEC, this is employed on the system seen in Figure B.1, giving the following H_2 mole flows:

$$\dot{n}_{H_2,j} = 0 \qquad \text{for stream } j = 1, 6..8$$

$$\dot{n}_{H_2,2} = \frac{x_{H_2,2}}{x_{H_20,2}} \cdot \dot{n}_{H_2O,req}, \qquad \dot{n}_{H_2,5} = \dot{n}_{H_2,2}$$

$$\dot{n}_{H_2,3} = \dot{n}_{H_2,2} + \dot{n}_{H_2,gen}, \qquad \dot{n}_{H_2,4} = \dot{n}_{H_2,3} \cdot (1 - SR_{H_2})$$

where $SR_{H_2} = \dot{n}_{H_2,2}/\dot{n}_{H_2,3}$ is the H_2 split ratio for recycling.

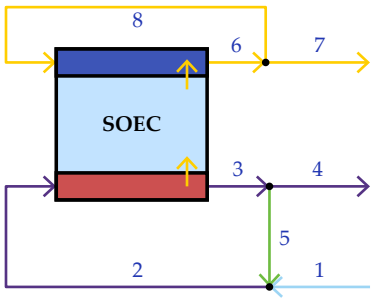

Figure B.1: Stream numbering for mole balance in SOEC.

The H_2O mole flows are determined by:

$$\dot{n}_{H_2O,j} = 0 \qquad \text{for stream } j = 5..8$$

$$\dot{n}_{H_2O,1} = \dot{n}_{H_2O,req}, \qquad \dot{n}_{H_2O,2} = \dot{n}_{H_2O,1}$$

$$\dot{n}_{H_2O,3} = \frac{\dot{n}_{H_2O,2} \cdot MW_{H_2O} - \dot{n}_{H_2,gen} \cdot MW_{H_2} - \dot{n}_{O_2,gen} \cdot MW_{O_2}}{MW_{H_2O}}, \qquad \dot{n}_{H_2O,4} = \dot{n}_{H_2O,3}$$

The O_2 mole flows are determined by:

$$\dot{n}_{O_2,j} = 0 \qquad \text{for stream } j = 1..5$$

$$\dot{n}_{O_2,6} = \dot{n}_{O_2,gen}, \qquad \dot{n}_{O_2,7} = \dot{n}_{O_2,6} \cdot (1 - SR_{O_2}), \qquad \dot{n}_{O_2,8} = \dot{n}_{O_2,6} \cdot SR_{O_2}$$

where SR_{O_2} is the O_2 split ratio for recycling. The total mole flows and mole fractions can then be determined from:

$$\dot{n}_j = \sum \dot{n}_{i,j}$$

$$x_{i,j} = \frac{\dot{n}_{i,j}}{\dot{n}_j} \qquad \text{for component } i = H_2, H_2O, O_2 \quad \text{and stream } j = 1..8$$

Finally, the conservation of mass is checked:

$$\dot{m}_3 + \dot{m}_6 - \dot{m}_2 = 0 \tag{B.18}$$

P-SOEC:

Similarly, the mole flows for the P-SOEc are determined from the system seen in Figure B.2.

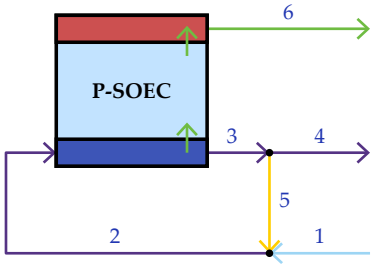

Figure B.2: Stream numbering for mole balance in P-SOEC.

The O_2 mole flows are determined by:

$$\dot{n}_{O_2,j} = 0 \qquad \text{for stream } j = 1,6$$

$$\dot{n}_{O_2,2} = \frac{x_{O_2,2}}{x_{H_2O,2}} \dot{n}_{H_2O,req} \qquad \dot{n}_{O_2,5} = \dot{n}_{O_2,2}$$

$$\dot{n}_{O_2,3} = \dot{n}_{O_2,2} + \dot{n}_{O_2,gen} \qquad \dot{n}_{O_2,4} = \dot{n}_{O_2,3} \cdot (1 - SR_{O_2})$$

The H_2O mole flows are determined by:

$$\dot{n}_{H_2O,j} = 0 \qquad \text{for stream } j = 5..6$$

$$\dot{n}_{H_2O,1} = \dot{n}_{H_2O,req} \qquad \dot{n}_{H_2O,2} = \dot{n}_{H_2O,1}$$

$$\dot{n}_{H_2O,3} = \frac{\dot{n}_{H_2O,2} \cdot MW_{H_2O} - \dot{n}_{H_2,gen} \cdot MW_{H_2} - \dot{n}_{O_2,gen} \cdot MW_{O_2}}{MW_{H_2O}} \qquad \dot{n}_{H_2O,4} = \dot{n}_{H_2O,3}$$

The H_2 mole flows are determined by:

$$\dot{n}_{H_2,j} = 0 \qquad \text{for stream } j = 1..5$$

$$\dot{n}_{H_2,6} = \dot{n}_{H_2,gen}$$

The total mole flows and mole fractions can then be determined in the same way as for the SOEC system. Finally, the conservation of mass is checked using equation (B.18).

Given the mole fractions for all streams, the bulk phase mole fractions can be found from which the bulk phase partial pressures are determined:

$$x_{H_2,bp} = \frac{x_{H_2,2} + x_{H_2,3}}{2} \qquad x_{H_2O,bp} = \frac{x_{H_2O,2} + x_{H_2O,3}}{2} \qquad x_{O_2,bp} = \frac{x_{O_2,6} + x_{O_2,7}}{2}$$

$$p_{H_2,bp} = x_{H_2,bp} \cdot P \qquad p_{H_2O,bp} = x_{H_2O,bp} \cdot P \qquad p_{O_2,bp} = x_{O_2,bp} \cdot P$$

C | Appendix: Aspen Models

C.1 Aspen Flowsheet Diagrams

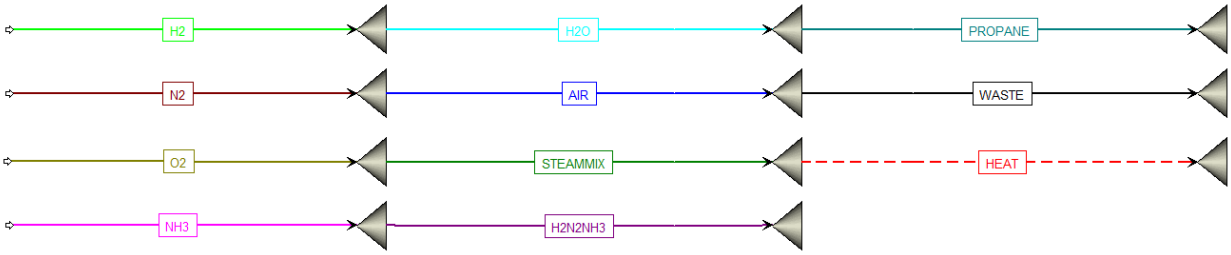

Figure C.1: Stream colour-coding in Aspen.

C.1.1 CASU

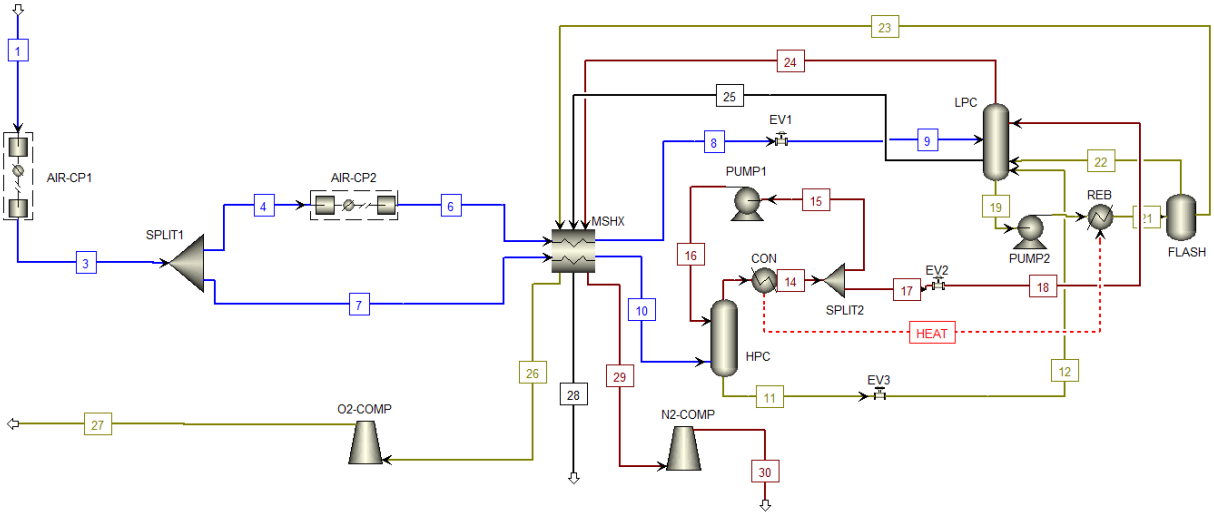

Figure C.2: Aspen flowsheet of CASU configuration.

Table C.1: Aspen block overview of CASU configuration.

CASU		
Block ID	**Aspen block**	**Specification**
AIR-CP1	MCompr	Discharge pressure: 6 bar
AIR-CP2	MCompr	Discharge pressure: 12 bar
SPLIT1	FSplit	Fraction: 0.32 (stream 4)
SPLIT2	FSplit	Fraction: 0.654 (stream 15)
MSHX	MHeatX	Air minor/major out: $-166\,^{\circ}\mathrm{C}$
HPC	RadFRac	Calculation type: Equilibrium, Stages: 20, Top stage: 4.45 bar
LPC	RadFRac	Calculation type: Equilibrium, Stages: 45, Top stage: 1.1 bar
PUMP1	Pump	Discharge pressure: 4.45 bar
PUMP2	Pump	Discharge pressure: 1.15 bar
EV1-3	Valve	Discharge pressure: 1.35 bar
CON	Heater	Discharge vapor fraction: 0
REB	Heater	Inlet heat stream
FLASH	Flash2	Heat duty: 0
O2-COMP	Compr	Discharge pressure: 30 bar
N2-COMP	Compr	Discharge pressure: 150 bar

Table C.2: Temperature, pressure, and composition of all streams in CASU systems (HT and LT cases) without H_2, NH_3, and H_2O.

			HT Case				**LT Case**			
Stream	T [°C]	P [bar]	$\dot{n}$ [kmol/s]	Composition [mol%]			$\dot{n}$ [kmol/s]	Composition [mol%]		
				N_2	O_2	Ar		N_2	O_2	Ar
1	15.00	1.013	1.027	78.10	20.95	0.950	1.030	78.10	20.95	0.950
3	17.00	5.950	1.027	78.10	20.95	0.950	1.030	78.10	20.95	0.950
4	17.00	5.950	0.329	78.10	20.95	0.950	0.330	78.10	20.95	0.950
6	17.00	11.95	0.329	78.10	20.95	0.950	0.330	78.10	20.95	0.950
7	17.00	5.950	0.698	78.10	20.95	0.950	0.700	78.10	20.95	0.950
8	-166.0	11.90	0.329	78.10	20.95	0.950	0.330	78.10	20.95	0.950
9	-191.2	1.350	0.329	78.10	20.95	0.950	0.330	78.10	20.95	0.950
10	-166.0	5.900	0.698	78.10	20.95	0.950	0.700	78.10	20.95	0.950
11	-177.8	4.450	0.428	64.26	34.20	1.547	0.429	64.26	34.20	1.547
12	-189.8	1.400	0.428	64.26	34.20	1.547	0.429	64.26	34.20	1.547
13	-180.5	4.450	0.782	99.99	0.000	0.006	0.784	99.99	0.001	0.006
14	-180.6	4.400	0.782	99.99	0.001	0.006	0.784	99.99	0.001	0.006
15	-180.6	4.400	0.511	99.99	0.001	0.006	0.513	99.99	0.001	0.006
16	-180.6	4.450	0.511	99.99	0.001	0.006	0.513	99.99	0.001	0.006
17	-180.6	4.400	0.270	99.99	0.001	0.006	0.271	99.99	0.001	0.006
18	-193.1	1.350	0.270	99.99	0.001	0.006	0.271	99.99	0.001	0.006
19	-182.4	1.100	0.726	0.000	99.33	0.672	0.729	0.000	99.33	0.672
20	-182.4	1.150	0.726	0.000	99.33	0.672	0.729	0.000	99.33	0.672
21	-182.4	1.100	0.726	0.000	99.33	0.672	0.729	0.000	99.33	0.672
22	-182.4	1.100	0.578	0.000	99.28	0.720	0.580	0.000	99.28	0.720
23	-182.4	1.100	0.148	0.000	99.51	0.486	0.149	0.000	99.51	0.486
24	-195.0	1.100	0.641	99.91	0.001	0.085	0.643	99.91	0.001	0.086
25	-189.4	1.100	0.238	68.07	28.36	3.571	0.238	67.97	28.45	3.579
26	15.04	1.050	0.148	0.000	99.51	0.486	0.149	0.000	99.51	0.485
27	599.8	30.00	0.148	0.000	99.51	0.486	0.149	0.000	99.51	0.485
28	15.04	1.050	0.238	68.07	28.36	3.571	0.238	67.97	28.45	0.086
29	15.04	1.050	0.641	99.91	0.001	0.085	0.643	99.91	0.001	0.086
30	1213	150.0	0.641	99.91	0.001	0.085	0.643	99.91	0.001	0.086

C.1.2 HB Loop

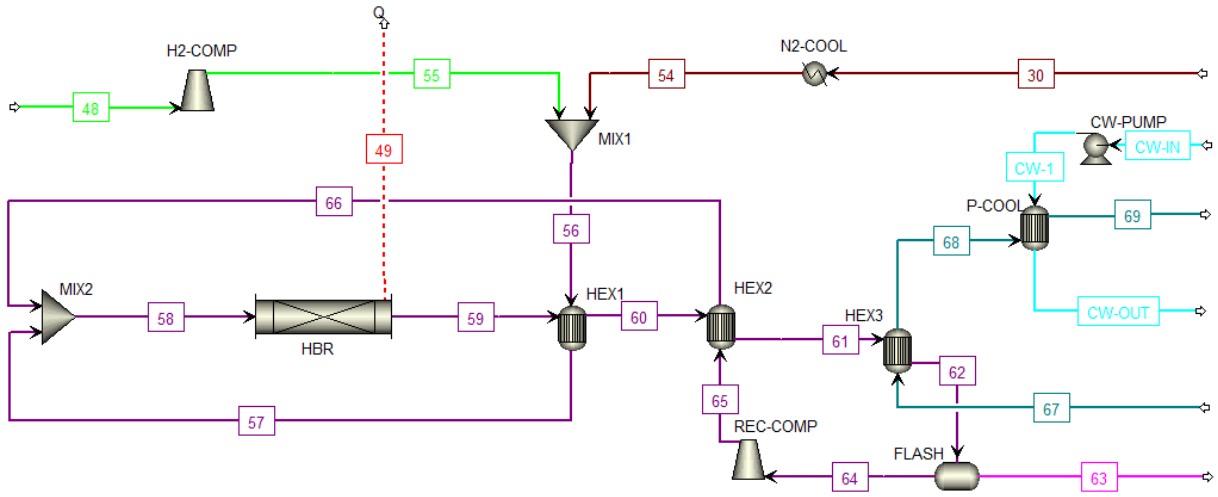

Figure C.3: Aspen flowsheet of HB loop configuration.

Table C.3: Aspen block overview of HBR configuration.

HB-LOOP		
Block ID	**Aspen block**	**Specification**
H2-COMP	Compr	Discharge pressure: 150 bar
N2-COOL	Heater	Cold outlet: 765 °C
MIX1	Mixer	-
MIX2	Mixer	-
HEX1	HeatX	Hot outlet: 450 °C
HEX2	HeatX	Hot outlet: 106 °C
HEX3	HeatX	Hot outlet: −18 °C
HBR	RPlug	Isothermal, Pressure drop: Ergun
FLASH	Flash2	Heat duty: 0
REC-COMP	Compr	Discharge pressure: 150 bar
P-COOL	Heater	Hot outlet: 45 °C
CW-PUMP	Pump	Discharge pressure: 1.1 bar

Table C.4: Temperature, pressure, and composition of all streams in HBR systems (HT and LT cases).

HT Case

Stream	T [°C]	P [bar]	$\dot{n}$ [kmol/s]	Composition [mol%]						
				N_2	H_2	NH_3	H_2O	Propane	O_2	Ar
30	1213	150.0	0.641	0.000	0.000	0.000	0.000	0.000	0.000	0.000
48	20.00	20.00	1.923	23.42	73.97	2.354	0.000	0.000	0.206	0.051
54	765.0	150.0	0.641	99.91	0.000	0.000	0.000	0.000	0.086	0.008
55	327.3	150.0	1.923	0.000	99.99	0.010	0.000	0.000	0.000	0.000
56	443.7	150.0	2.563	25.00	74.97	0.007	0.000	0.000	0.022	0.002
57	445.0	149.9	2.563	23.90	74.27	1.644	0.000	0.000	0.150	0.036
58	444.7	149.9	8.459	0.000	0.000	0.000	100.0	0.000	0.000	0.000
59	450.0	149.3	7.182	0.000	0.000	0.000	0.000	100.0	0.000	0.000
60	449.6	149.3	7.182	23.42	73.97	2.354	0.000	0.000	0.206	0.051
61	105.7	149.2	7.182	23.42	73.97	2.354	0.000	0.000	0.206	0.051
62	-18.00	149.2	7.182	0.000	0.000	0.000	0.000	100.0	0.000	0.000
63	-18.00	149.2	1.287	23.42	73.97	2.354	0.000	0.000	0.206	0.051
64	-18.00	149.2	5.895	19.26	60.82	19.70	0.000	0.000	0.177	0.043
65	-17.50	150.0	5.895	19.26	60.82	19.70	0.000	0.000	0.177	0.043
66	444.6	150.0	5.895	19.26	60.82	19.70	0.000	0.000	0.177	0.043
67	-23.00	1.500	15.28	0.000	0.000	0.000	0.000	0.000	0.000	0.000
68	27.51	1.450	15.28	0.000	0.000	0.000	0.000	100.0	0.000	0.000
69	45.00	14.95	15.28	0.000	0.000	0.000	0.000	0.000	0.000	0.000
CW-1	15.00	1.100	17.50	99.91	0.000	0.000	0.000	0.000	0.086	0.008
CW-IN	15.00	1.050	17.50	0.000	99.99	0.010	0.000	0.000	0.000	0.000
CW-OUT	102.9	1.050	17.50	25.00	74.97	0.007	0.000	0.000	0.022	0.002

LT Case

Stream	T [°C]	P [bar]	$\dot{n}$ [kmol/s]	Composition [mol%]						
				N_2	H_2	NH_3	H_2O	Propane	O_2	Ar
30	1213	150.0	0.643	99.91	0.000	0.000	0.000	0.000	0.086	0.008
48	20.00	20.00	1.929	0.000	99.99	0.010	0.000	0.000	0.000	0.000
54	765.0	150.0	0.643	99.91	0.000	0.000	0.000	0.000	0.086	0.008
55	328.4	150.0	1.929	0.000	99.99	0.010	0.000	0.000	0.000	0.000
56	444.6	150.0	2.572	25.00	74.97	0.007	0.000	0.000	0.022	0.002
57	445.0	149.9	2.572	25.00	74.97	0.007	0.000	0.000	0.022	0.002
58	444.9	149.9	8.502	23.90	74.27	1.644	0.000	0.000	0.150	0.036
59	450.0	149.3	7.219	19.26	60.82	19.70	0.000	0.000	0.177	0.043
60	449.9	149.3	7.219	19.26	60.82	19.70	0.000	0.000	0.177	0.043
61	105.5	149.2	7.219	19.26	60.82	19.70	0.000	0.000	0.177	0.043
62	-18.00	149.2	7.219	19.26	60.82	19.70	0.000	0.000	0.177	0.043
63	-18.00	149.2	1.290	0.138	0.391	99.42	0.000	0.000	0.042	0.004
64	-18.00	149.2	5.929	23.42	73.97	2.354	0.000	0.000	0.206	0.051
65	-17.50	150.0	5.929	23.42	73.97	2.354	0.000	0.000	0.206	0.051
66	444.9	150.0	5.929	23.42	73.97	2.354	0.000	0.000	0.206	0.051
67	-23.00	1.500	15.28	0.000	0.000	0.000	0.000	100.0	0.000	0.000
68	27.58	1.450	15.28	0.000	0.000	0.000	0.000	100.0	0.000	0.000
69	45.00	14.95	15.28	0.000	0.000	0.000	0.000	100.0	0.000	0.000
CW-1	15.00	1.100	17.50	0.000	0.000	0.000	100.0	0.000	0.000	0.000
CW-IN	15.00	1.050	17.50	0.000	0.000	0.000	100.0	0.000	0.000	0.000
CW-OUT	102.9	1.050	17.50	0.000	0.000	0.000	100.0	0.000	0.000	0.000

C.2 SOEC & P-SOEC System

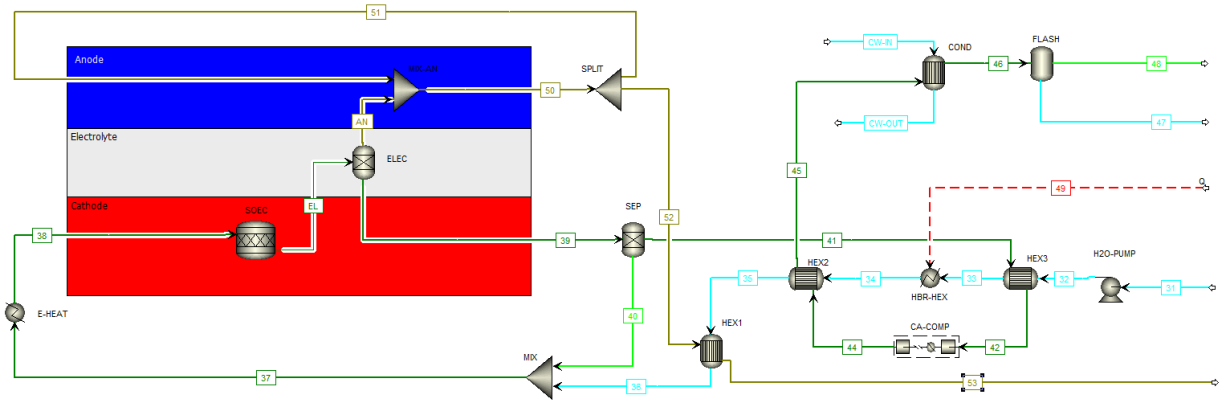

Figure C.4: Aspen flowsheet of SOEC-INT configuration.

Table C.5: Aspen block overview of SOEC-INT configuration.

SOEC-INT		
Block ID	**Aspen block**	**Specification**
H2O-PUMP	Pump	Discharge pressure: 1.263 bar
HEX1	HeatX	Hot outlet: 548.3 °C
HEX2	HeatX	Hot outlet: 356.1 °C
HEX3	HeatX	Hot outlet: 50 °C
HBR-HEX	Heater	Heat duty: 67.18 MW
MIX	Mixer	-
E-HEAT	Heater	Heat duty: 12.32 MW
SOEC	RStoic	Fractional conversion: 96.8%
ELEC	Sep	O_2 split fraction: 1
AN-MIX	Mixer	-
SPLIT	FSplit	O_2 flow: 864.1 kmol/h
SEP	Sep	H_2 flow: 793.5 kmol/h
CA-COMP	Compr	Discharge pressure: 20.1 bar
COND	Heater	Hot outlet: 20 °C
FLASH	Flash2	

Table C.6: Temperature, pressure, and composition of all streams in SOEC systems.

	SOEC-B						SOEC-INT					
Stream	T [°C]	P [bar]	$\dot{n}$ [kmol/s]	Composition [mol%]			T [°C]	P [bar]	$\dot{n}$ [kmol/s]	Composition [mol%]		
				H_2O	H_2	O_2				H_2O	H_2	O_2
31	15.00	1.013	1.984	100.0	0.000	0.000	15.00	1.013	0.001	100.0	0.000	0.000
32	15.00	1.263	1.984	100.0	0.000	0.000	15.00	1.263	0.001	100.0	0.000	0.000
33	105.1	1.213	1.984	100.0	0.000	0.000	105.1	1.213	0.001	100.0	0.000	0.000
34	103.9	1.163	1.984	100.0	0.000	0.000	351.1	1.163	0.001	100.0	0.000	0.000
35	102.6	1.113	1.984	100.0	0.000	0.000	543.3	1.113	0.001	100.0	0.000	0.000
36	119.2	1.063	1.984	100.0	0.000	0.000	649.6	1.063	0.001	100.0	0.000	0.000
37	178.2	1.013	2.204	90.00	10.00	0.000	661.1	1.013	0.001	90.00	10.00	0.000
38	800.0	1.013	2.204	90.00	10.00	0.000	800.0	1.013	0.001	90.00	10.00	0.000
39	800.0	1.013	2.204	2.880	97.12	0.000	800.0	1.013	0.001	2.880	97.12	0.000
40	800.0	1.013	0.220	0.000	100.0	0.000	800.0	1.013	0.000	0.000	100.0	0.000
41	800.0	1.013	1.984	3.200	96.80	0.000	800.0	1.013	0.001	3.200	96.80	0.000
42	50.00	0.963	1.984	3.200	96.80	0.000	50.00	0.963	0.001	3.200	96.80	0.000
44	600.0	20.05	1.984	3.200	96.80	0.000	600.0	20.05	0.001	3.200	96.80	0.000
45	108.9	20.00	1.984	3.200	96.80	0.000	356.1	20.00	0.001	3.200	96.80	0.000
46	20.00	19.95	1.984	3.200	96.80	0.000	20.00	19.95	0.001	3.200	96.80	0.000
47	20.00	20.00	1.923	0.129	99.87	0.000	20.00	20.00	0.000	99.70	0.302	0.000
48	20.00	20.00	0.061	99.70	0.302	0.000	20.00	20.00	0.001	0.129	99.87	0.000
50	800.0	1.013	1.200	0.000	0.000	100.0	800.0	1.013	0.000	0.000	0.000	100.0
51	800.0	1.013	0.240	0.000	0.000	100.0	800.0	1.013	0.000	0.000	0.000	100.0
52	800.0	1.013	0.960	0.000	0.000	100.0	800.0	1.013	0.000	0.000	0.000	100.0
53	107.6	0.963	0.960	0.000	0.000	100.0	548.3	0.963	0.000	0.000	0.000	100.0
CW-IN	15.00	1.013	6.944	100.0	0.000	0.000	15.00	1.013	0.002	100.0	0.000	0.000
CW-OUT	29.60	0.963	6.944	100.0	0.000	0.000	57.06	0.963	0.002	100.0	0.000	0.000

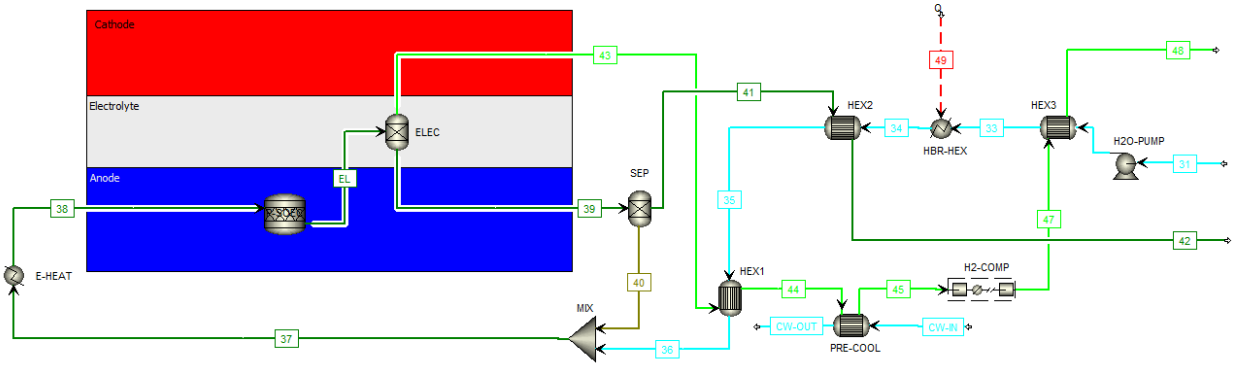

Figure C.5: Aspen flowsheet of P-SOEC-INT configuration.

Table C.7: Aspen block overview of P-SOEC-INT configuration.

P-SOEC-INT		
Block ID	**Aspen block**	**Specification**
H2O-PUMP	Pump	Discharge pressure: 1.263 bar
HEX1	HeatX	Hot outlet: 106.3 °C
HEX2	HeatX	Hot outlet: 197.6 °C
HEX3	HeatX	Hot outlet: 20 °C
HBR-HEX	Heater	Heat duty: 67.50 MW
MIX	Mixer	-
E-HEAT	Heater	Heat duty: 63.55 MW
P-SOEC	RStoic	Fractional conversion: 53.77%
ELEC	Sep	H_2 split fraction: 1
SEP	Sep	O_2 flow: 1435 kmol/h
PRE-COOL	HeatX	Hot outlet: 60 °C
H2-COMP	MCompr	Discharge pressure: 20.05 bar

Table C.8: Temperature, pressure, and composition of all streams in SOEC systems.

	P-SOEC-B						P-SOEC-INT					
Stream	T [°C]	P [bar]	$\dot{n}$ [kmol/s]	Composition [mol%]			T [°C]	P [bar]	$\dot{n}$ [kmol/s]	Composition [mol%]		
				H_2O	H_2	O_2				H_2O	H_2	O_2
31	15.00	1.013	3.587	100.0	0.000	0.000	15.00	1.013	3.587	100.0	0.000	0.000
32	15.00	1.213	3.587	100.0	0.000	0.000	15.00	1.213	3.587	100.0	0.000	0.000
33	103.9	1.163	3.587	100.0	0.000	0.000	103.9	1.163	3.587	100.0	0.000	0.000
34	102.6	1.113	3.587	100.0	0.000	0.000	102.6	1.113	3.587	100.0	0.000	0.000
35	101.3	1.063	3.587	100.0	0.000	0.000	101.3	1.063	3.587	100.0	0.000	0.000
36	99.95	1.013	3.587	100.0	0.000	0.000	99.95	1.013	3.587	100.0	0.000	0.000
37	94.40	1.013	3.985	90.00	0.000	10.00	96.87	1.013	3.985	90.00	0.000	10.00
38	500.0	1.013	3.985	90.00	0.000	10.00	500.0	1.013	3.985	90.00	0.000	10.00
39	500.0	1.013	3.021	54.89	0.000	45.11	500.0	1.013	3.021	54.89	0.000	45.11
40	500.0	1.013	0.399	0.000	0.000	100.0	500.0	1.013	0.399	0.000	0.000	100.00
41	500.0	1.013	2.623	63.23	0.000	36.77	500.0	1.013	2.623	63.23	0.000	36.77
42	107.6	0.963	2.623	63.23	0.000	36.77	107.6	0.963	2.623	63.23	0.000	36.77
43	500.0	1.013	1.929	0.000	100.0	0.000	500.0	1.013	1.929	0.000	100.00	0.000
44	106.3	0.963	1.929	0.000	100.0	0.000	106.3	0.963	1.929	0.000	100.00	0.000
45	60.00	0.913	1.929	0.000	100.0	0.000	60.00	0.913	1.929	0.000	100.00	0.000
47	600.0	20.05	1.929	0.000	100.0	0.000	600.0	20.05	1.929	0.000	100.00	0.000
48	20.00	20.00	1.929	0.000	100.0	0.000	20.00	20.00	1.929	0.000	100.00	0.000
CW-IN	15.00	1.018	0.417	100.0	0.000	0.000	15.00	1.018	0.417	100.0	0.000	0.000
CW-OUT	96.97	0.968	0.417	100.0	0.000	0.000	96.97	0.968	0.417	100.0	0.000	0.000

C.3 HEX Network Optimisation in Aspen

C.3.1 SOEC System

Summary Table				
Property	Actual	Target	Available Savings	% of Actual
Total Utilities [Watt]	5.544E+11	5.544E+11	0	0
Heating Utilities [Watt]	554400000	554400000	0	0
Cooling Utilities [Watt]	167.5	167.5	0	0
Carbon Emissions [kg/hr]	0	0	0	0

Figure C.6: Aspen Energy Analyser table overview of utilised utilities for SOEC-B case.

Summary Table				
Property	Actual	Target	Available Savings	% of Actual
Total Utilities [Watt]	5.544E+11	5.544E+11	0	0
Heating Utilities [Watt]	554400000	554400000	0	0
Cooling Utilities [Watt]	167.5	167.5	0	0
Carbon Emissions [kg/hr]	0	0	0	0

Figure C.7: Aspen Energy Analyser table overview of utilised utilities for SOEC-INT case.

C.3.2 P-SOEC System

Summary Table				
Property	Actual	Target	Available Savings	% of Actual
Total Utilities [Watt]	60900000000	60900000000	0	0
Heating Utilities [Watt]	609000000	609000000	0	0
Cooling Utilities [Watt]	0	0	0	0
Carbon Emissions [kg/hr]	0	0	0	0

Figure C.8: Aspen Energy Analyser table overview of utilised utilities for P-SOEC-B case.

Summary Table				
Property	Actual	Target	Available Savings	% of Actual
Total Utilities [Watt]	60900000000	60900000000	0	0
Heating Utilities [Watt]	609000000	609000000	0	0
Cooling Utilities [Watt]	0	0	0	0
Carbon Emissions [kg/hr]	0	0	0	0

Figure C.9: Aspen Energy Analyser table overview of utilised utilities for P-SOEC-INT case.